Precipitation Hardening in a Magnesium-Neodymium-Zinc Alloy

by

Amirreza Sanaty Zadeh

A dissertation submitted in partial fulfillment of
the requirements for the degree of

Doctor of Philosophy
(Materials Science)

at the

UNIVERSITY OF WISCONSIN-MADISON

2014

Date of final oral examination: 09/22/14

The dissertation is approved by the following members of the Final Oral Committee:
Donald Stone, Professor, Materials Science and Engineering
Roderick Lakes, Professor, Engineering Physics
Susan Babcock, Professor, Materials Science and Engineering
Izabela Szlufarska, Professor, Materials Science and Engineering
Dane Morgan, Professor, Materials Science and Engineering

ABSTRACT

The effects of thermal history and deformation on precipitation behavior and precipitation kinetics in a magnesium-zinc-rare earth alloy were studied. The composition of the studied alloy is Mg-0.2Zn- 3Nd (% wt). The microstructure analysis of the aged alloys revealed the presence of some new phases in the microstructure in addition to the old description: *Super saturated solid solution (SSSS)→ G. P. zones → β" → β' → β,* reported for Mg-Nd system. In this regard, the sequence of precipitation for the studied alloy was identified as: *Super saturated solid solution (SSSS)→ Clusters of atoms → G. P. zones (I, II, III) → β' → β_2 → β_1 / γ' → β.*

The formation of clusters of solute atoms in this system was confirmed by scanning electron transmission microscopy and atom probe tomography analysis. In addition, new metastable phases, designated as G. P. zones (I, II, III) and β_2, were identified in the microstructure of aged alloys by means of high resolution high angle annular dark field scanning transmission electron microscopy. The β_2 phase was found to be a transition phase in transformation of β' to β_1. Furthermore, microstructure analysis revealed that the structure of β_1 phase is indeed a body

centered tetragonal structure in spite of face centered cubic structure that has been reported for this phase in the literature.

The kinetics analysis of precipitation revealed that the concentration of excess vacancies is critical in growth kinetics of G. P. zones and β'/ β_2. The presence of quenched in vacancies in the solid solution state leads to a lower activation energy of the growth for the mentioned phases.

The effect of prior deformation on age hardening behavior of this alloy was investigated. The higher yield strength of pre-deformed aged alloys was attributed to the pinning effect resulting from segregation of solute atoms into defects such as dislocations and twin boundaries. Analysis showed that the presence of solute atom clusters (i.e. Nd-Zn clusters) can enhance the pinning effect that results from segregation of these atoms into defects. As a result, aforementioned behavior can explain higher strength and improved creep resistance of these alloys.

Differential scanning calorimetry analysis of the deformed alloys revealed that the deformation enhances the kinetics of β_1 precipitation while it has a slight negative effect on precipitation of G. P. zones and β'/β_2. The negative effect was attributed to the annihilation of quenched in vacancies. The positive effect on β_1 precipitation was related to the effect of shear strain, introduced by basal dislocations and twins, in lowering the required energy for shearing of β_2 lattice in β_2/β_1 transformation.

Acknowledgement

I would like to thank Professor Donald Stone for giving me the opportunity and support to pursue my Ph.D. education at the University of Wisconsin-Madison. His close relationships with his students and understanding of their difficulties are priceless. I am grateful to Professor Susan Babcock for supporting me to start my Ph.D. at the University of Wisconsin-Madison and for her encouragement and advice throughout my whole duration of studies at the university. I would like to express my gratitude to my other Ph.D. committee members: Professor Roderick Lakes, Professor Izabela Szlufarska, and Professor Dane Morgan for their valuable discussion, feedback, and advice on my Ph.D. thesis. I would also like to express my gratitude to Professor Alan Luo at the Ohio State University for his valuable suggestions and insight on my research and publications.

I extend my thanks to Dr. Alex Kvit for his helpful training and assistance on the TEM and STEM instruments. I greatly appreciate his effort in assisting me throughout my research during and after business hours. Many thanks to Dr. Rick Noll for his training and useful information on the SEM and FIB facilities. I would also like to give thanks to Dr. Paul Ransheim for his training on APT and his valuable insights on the data analysis.

I extend my appreciation to Diana Rhodes for all of her administrative support, providing students with information about the program, and helping with all necessary paperwork. I would like to express thanks to my fellow lab group members, Xianguy Xia, Humberto Melgarejo, Nayomi Plaza, Samuel Zelinka, and Laura Hasburgh, for their valued contributions in our group meetings. We have had many wonderful times together, from conducting experiments to having

get-togethers and dining out at restaurants. I am grateful to them for continuously supporting my goals and pursuits.

I acknowledge the financial support provided by the National Science Foundation, DMR GOALI Program (Grant No. 1005762) which made it possible for me to pursue my Ph.D. I also acknowledge the use of instruments in the materials science center at the University of Wisconsin-Madison supported by UW MRSEC (DMR-1121288), UW NSEC (DMR-0832760), UW MRSEC (DMR-1121288), UW NSEC (DMR-0832760), and UW MRSEC (DMR-1121288).

Finally, special recognition goes out to my family, for their priceless encouragement, support, and patience throughout my Ph.D. studies. To my soul mate Paria who stood by me during the three years of our wonderful friendship. Even though I was not able to be there for her at all times, she continuously encouraged me through the whole process and supported me in every way. To my parents, my sister, and my brother for their unconditional love and their support during my twelve years of post-secondary education. To my parents-in-law for their love, support, and encouragement during my Ph.D. To Soheila and Rahim, for their support, love, and guidance throughout all years of being far from home. I thank all of you for patience and priceless love.

Last but not the least, I express my sincere and humble gratitude to Almighty God whom I seek in every moment of my life.

تقدیم به

سپیدار

List of Abbreviations

AFM	Atomic Force Microscopy
APT	Atom Probe Tomography
BCT	Body Centered Tetragonal
BCO	Based Centered Orthorhombic
BSE	Back Scattered Electron
DSC	Differential Scanning Calorimetry
EELS	Electron Energy Loss Spectroscopy
EDX	Energy Dispersive X-ray
EPMA	Electron Probe Micro Analysis
FCC	Faced Centered Cubic
FFT	Fast Fourier Transform
HAADF	High Angle Annular Dark Filed
HCP	Hexagonal Closed Packed
HREM	High Resolution Electron Microscopy
JMAK	John Mehl Avrami Kolomogrov
PFZ	Precipitation Free Zone
SAXS	Small Angle X-ray Scattering
SEM	Scanning Electron Microscopy
STEM	Scanning Transmission Electron Microscopy
SSSS	Super Saturated Solid Solution
TEM	Transmission Electron Microscopy
XRD	X-Ray Diffraction

Table of Contents

Chapter 1

1. Introduction

The precipitation hardening magnesium alloys have been one of the key focuses of researchers in automotive and aerospace industries over the last decades [1-3]. The advantage of these alloys is their high strength/weight ratio property. Among those, rare earth containing magnesium alloys attracted more attention. The importance of rare earth elements is their simultaneous effect on the hardness and ductility of magnesium through precipitation hardening and texture randomization, respectively [4-6]. Among rare earth elements, neodymium has a higher precipitation potential due to its lower solubility at room temperature [7-9]. However, information on the precipitation behavior of magnesium (Mg) -neodymium (Nd) alloying system during thermal treatment is limited. This is partially due to complexity of the precipitation and partially due to the recent development of this alloying system [8].

In my research I have performed a systematic characterization of the precipitation phenomena in Mg-Nd-Zn alloy. My goals were to:

1) Characterize the precipitation sequence that contributes to age hardening in the alloys;
2) Quantify the kinetics of precipitation to gain insight into the mechanisms of phase transformation;
3) Examine effects of aging temperature and prior deformation on precipitate evolution and hardening, which is useful to materials engineers who wish to tailor the properties of these alloys.

Outcomes of this research will be useful in designing processing conditions for Mg-Zn-RE alloys to achieve optimal properties. In addition, quantitative measurements and calculated parameters provide a database for simulation of precipitation in these alloys.

Chapter 2

2. Literature Survey

2.1. Magnesium

Magnesium is the fourth most common element on the earth although virtually all is bound oxide and hydroxide compounds because of its high reactivity. The pure metal has a hexagonal closed packed (HCP) structure (a = 0.321 nm and c = 0.521 nm) [10]. It is also the third most abundant element found in seawater due to high solubility of magnesium ions in water [11]. The most common method in producing magnesium is electrolysis of magnesium salts from brine [12]. Some applications of magnesium include starting emergency fires, flash photography, flares, and fireworks. The most common application of magnesium is as an alloying element in aluminum and other alloys such as magnesium-based alloys. Addition of different elements into magnesium alters the properties of magnesium drastically which indeed is used to produce alloys for specific applications. Due to their low densities magnesium alloys are often used in high strength/weight ratio applications [13].

2.2. Magnesium alloys

Common alloying elements for magnesium (Mg) include aluminum, zinc, manganese, silicon, copper, rare earth (RE) elements, and zirconium. The presence of aluminum is usually accompanied by existence of manganese for improvement in grain structure [14, 15]. In the absence of manganese and aluminum, zirconium is often present in the alloy for grain refinement purpose [7-9, 16, 17]. Most metal alloys are referred to by codes which contain information on their compositions and heat treatments. The same is true for Mg alloys, but here the designation system is not as well established as it is for other alloy systems. Typically, for Mg alloys the code starts with letters showing the two main alloying elements followed by numbers related to the weight percent of each element. For instance for the alloy AZ31, the letter A refers to aluminum, letter Z refer to Zinc, the number 3 refers to 3 wt.% aluminum and number 1 refer to 1 wt.% zinc. The designated letters for some of the alloying elements are listed in table 2. 1 [18].

Table 2. 1. The designated letters for alloy coding in magnesium alloys

Element	Al	Bi	Cu	Cd	RE	Fe	Th	Sr	Zr	Li	Mn
Letter code	A	B	C	D	E	F	H	J	K	L	M
Element	Ni	Pb	Ag	Cr	Ag	Sn	Gd	Y	Ca	Sb	Zn
Letter code	N	P	Q	R	S	T	V	W	X	Y	Z

Some examples of commercialized magnesium alloys are AZ63, AZ81, AZ91, AM50, AM60, ZK51, ZK60, ZK61, ZE41, ZC63, HK31, HZ32, QE22, QH21, WE54, WE43, etc [19]. Magnesium alloys are made in the form of cast alloys and wrought alloys; however, due to complexity of plastic deformation in elements with HCP lattice structure, these alloys are usually used in cast form. Magnesium cast alloys are produced by sand-permanent mold and die casting methods.

Due to low weight-high strength property of magnesium alloys, these alloys are mostly used in

electronics, aerospace and automotive industries [20]. Examples are WE43 in the components of aircraft and high performance vehicles [21], AMC602 non-combustible Mg alloys [22], AJ62 in high temperature engines and rare earth containing magnesium alloys in high temperature creep resistant and corrosion resistant applications [23].

2.2.1 Rare earth additions

Magnesium alloys have recently received considerable attention due to their low density and high specific strengths [1, 2]. However, the poor ductility of magnesium at room temperature due to its Hexagonal Closed-Packed (HCP) structure and low creep resistance and strength at elevated temperatures limit its applications in critical structural components [1-3]. Modification of texture is reported to improve the ductility of magnesium alloys greatly [2, 3]. This is achieved by alloying magnesium with rare-earth elements such as cerium (Ce), gadolinium (Gd), and neodymium (Nd) [4-7]. It has been reported in different researches that the addition of rare earth elements also has a significant effect on the hardness and creep resistance of Mg alloys both at room and elevated temperatures [8].

Among the rare earth elements Nd has relatively high solid solubility at the eutectic point and low solid solubility at room temperature (~0.08 wt. %), which make it suitable for texture randomization and age hardening of magnesium and magnesium alloys [8]. The strength of Mg-Nd alloys can be further enhanced by controlled addition of third element such as zinc (Zn) [24-28]. It has been shown that proper addition of Zn to Mg–Nd binary system improves the mechanical properties through solid solution strengthening mechanism [8, 26-33]. However, higher amount of Zn (>0.5 wt. %) was shown to reduce the precipitation hardening effect of neodymium which is due to the effect of zinc on the sequence and nature of precipitation [8].

2.3. Precipitation sequence in Mg-RE alloys

The sequence of precipitation in Mg-RE alloys varies based on the composition and the effect of other alloying elements. For instance in the binary Mg-Nd alloy, the sequence is somehow different from the ternary Mg-Zn-Nd alloys. In terms of Mg-3Nd (wt. %) alloy, the sequence is reported to be: *SSSS* → *G.P. zones* → *β"* → *β'*→ *β* [7]. Fig 2. 1. shows TEM micrographs taken from these precipitates in a Mg-3 wt. % Nd alloy [7]. Later on, it was shown that another intermediate phase β_1 (fcc) also forms during isothermal aging and after β' precipitation which eventually transforms into equilibrium phase β [34]. This sequence is almost the same for magnesium alloys containing only rare earth element as the alloying element. However, the kinetics of precipitation varies from one to another.

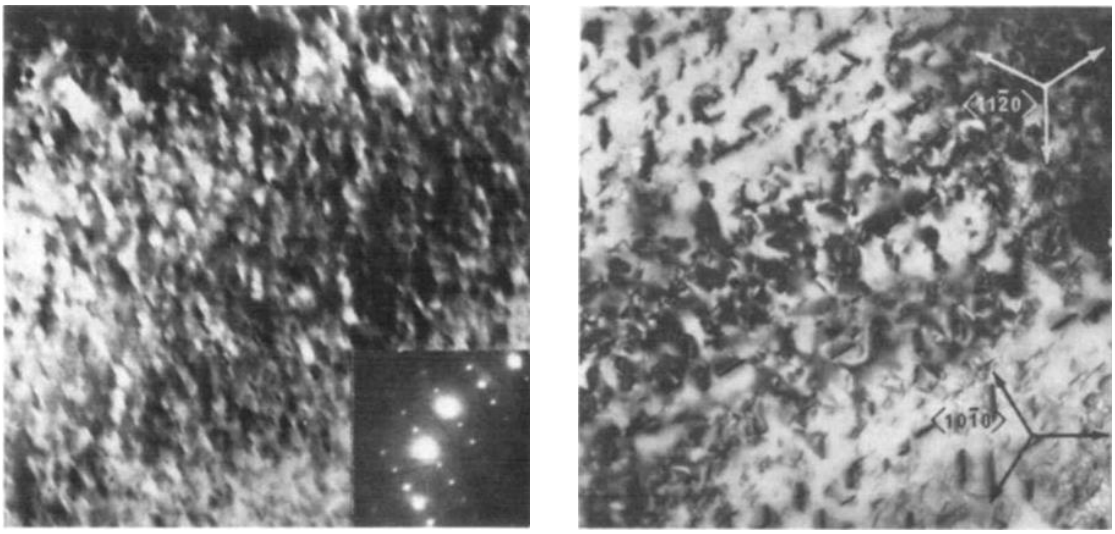

(a) (b)

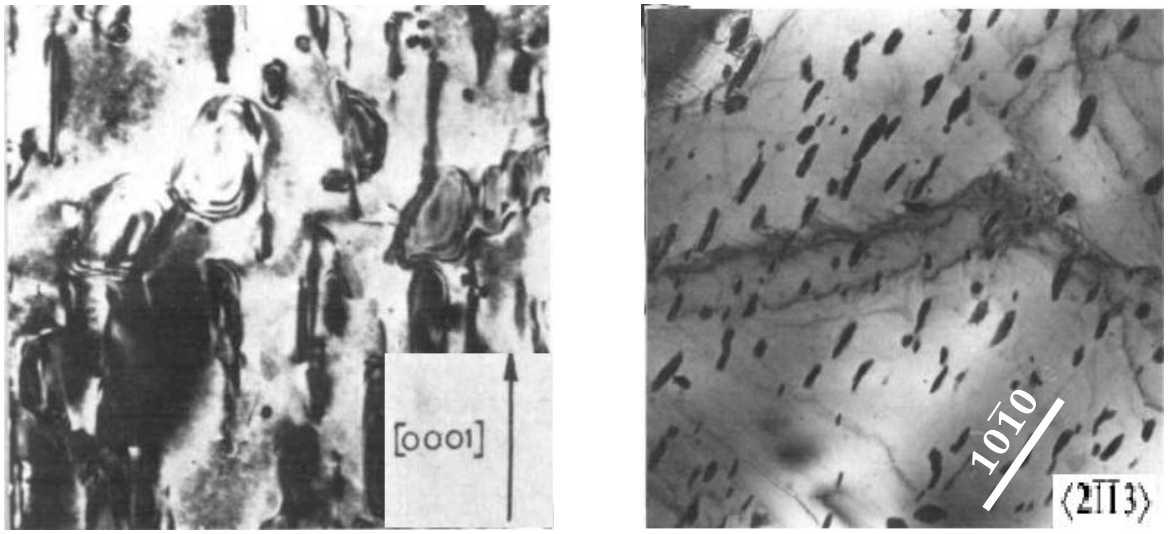

(c) (d)

Fig 2. 1. TEM micrographs of the metastable and stable phases which evolve during heat treatment of the Mg-3 wt.% Nd: a) High resolution dark-field micrograph of G.P. zones in specimen aged at 180°C for 8 h (x 120,000); b) β" precipitates in specimen aged at 190°C for one day (x 40,000); c) Coarse, disc-shaped β' precipitates in specimen aged at 24°C for one week (x 30,000); d)Specimen deformed 10% before ageing at 350°C for 30 min, showing particles of β (x 6000).

In the ternary alloy Mg-Nd-Zn containing 2.8 wt. % Nd and 1.3wt% Zn, the sequence changes drastically to SSSS → low-temperature reaction→ γ'' → γ [8, 9]. Fig. 2.2. shows TEM micrographs of the two intermediate phases γ'' and γ in this alloy [9]. The nature of low-temperature reaction has not been fully understood but it is postulated that it is related to the formation of G.P. zones. The addition of 1.3 wt. % zinc seems to completely change the nature and sequence of precipitation from Nd enriched β series to Zn enriched γ series. In other word, the addition of zinc has a restricting effect on the precipitation of β series and consequently on precipitation hardening in these alloys. A recent study on Mg- 3 wt.% Nd alloy with 0.2 wt. % and 0.5 wt. % Zn revealed the co-existence of β' and γ' in alloy containing 0.5 wt. % Zn. However, for the alloy with 0.2 wt. %, γ' is rarely distributed on some grains. From above discussion, it can be concluded that the amount of zinc plays an important role in sequence of

precipitation. Higher amount of Zn (>0.5 wt. %) reduces the precipitation hardening effect by restricting the precipitation of Mg-Nd phase. Also higher amounts of zinc than 0.5 wt. % was experimentally shown to degrade the mechanical properties (i.e. formability) of the alloy [8].

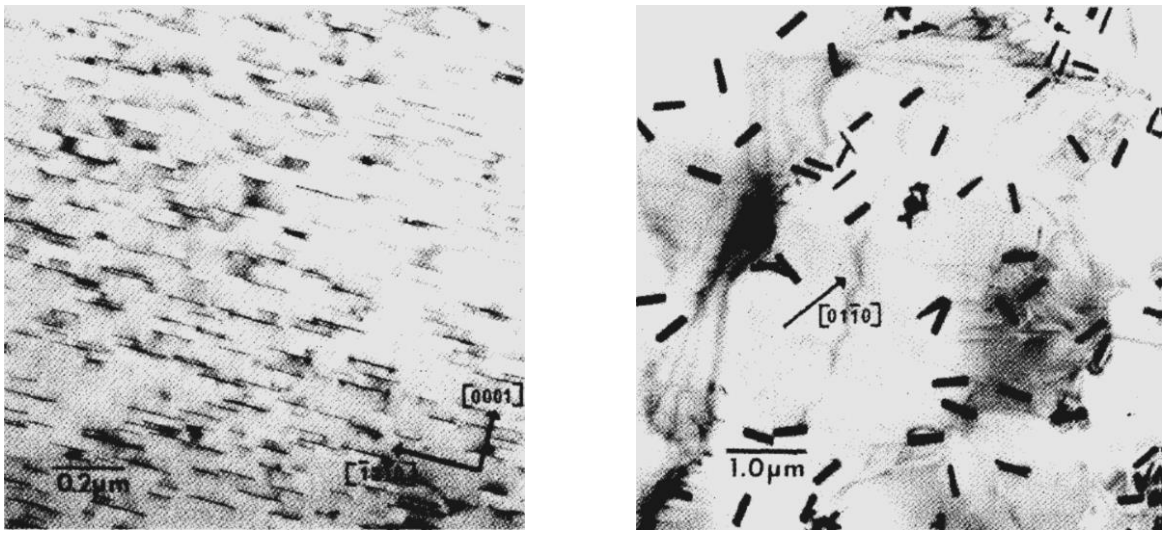

(a) (b)

Fig. 2. 2. TEM micrographs of Mg- 2.8wt%Nd- 1.3wt% Zn: a) Coarse γ" produced by aging at 325°C for 1 hr; b) Electron micrographs of the γ phase. Sample aged 3 days at 325 °C.

2.4. Structure of intermediate precipitates

2.4.1. β Series

The structure of the G. P. zones have not been evaluated due to small size of these features and instrumentation limits. There is no report on compositions of G.P zones as well. However, in a paper by Hirage et al, it is reported to be the same as *β''* [35]. The structure of *β''* is determined as ordered D019, as shown in Fig. 2. 3., with $a_{\beta''} = 2a_{Mg}$ and $c_{\beta''} = c_{Mg}$. According to the arrangement of atoms in the structure, the composition of *β''* was determined as Mg_3Nd [7, 8, 35]. This phase forms on both prismatic planes type I and II ($(11\bar{2}0)$ and $(10\bar{1}0)$) [8] and is fully coherent with the matrix. Similar structure has been reported for the *β''* in alloys containing Gd and Nd [35-39].

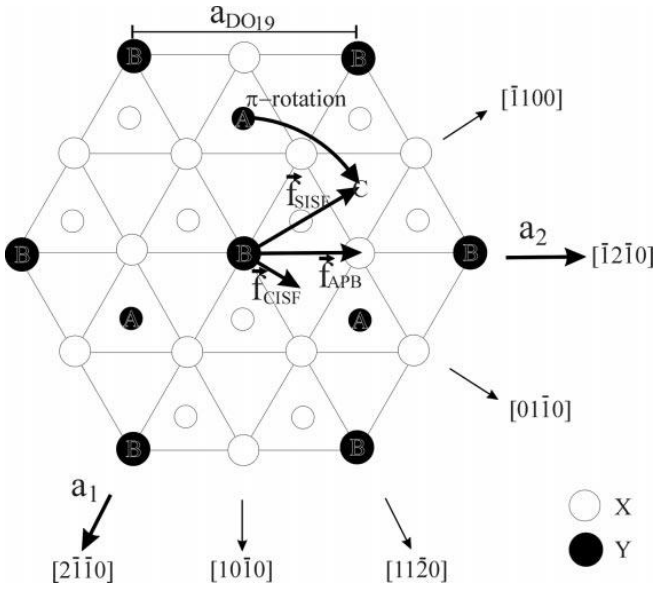

Fig. 2. 3. Atomic arrangement in the {0001} planes of a DO19 structure based on the Mg_3Nd composition. Open and full circles represent Mg and Nd atoms, respectively. Large circles represent atoms in the A layer and small circles represent atoms in layer B (below and above layer A). The sequence ABAB corresponds to the DO19 structure [39].

Transformation of *β''* into *β'* leads to a transition in structure of the precipitates. According to literature, *β'* forms on prismatic planes type I($10\bar{1}0$). The arrangement of atoms in *β'* results in a formation of a fully coherent phase with the matrix [35-38]. The lattice parameters for this phase have been determined from diffraction patterns and high resolution electron microscopy and the results are not consistent. In the research by Pike et al on Mg-3Nd (wt. %) [7], the structure is determined as hexagonal with $a_{\beta'}$ = 0.52 nm and $c_{\beta'}$ = 1.3 nm. However, in recent researches on Mg-RE (Gd, and Nd) alloys, a base centered orthorhombic structure with lattice parameters $a_{\beta'}$ =0.642 nm, $b_{\beta'}$=2.223 nm, $c_{\beta'}$=0.521 nm is reported for the *β'* phase (see. Fig. 2. 4.).

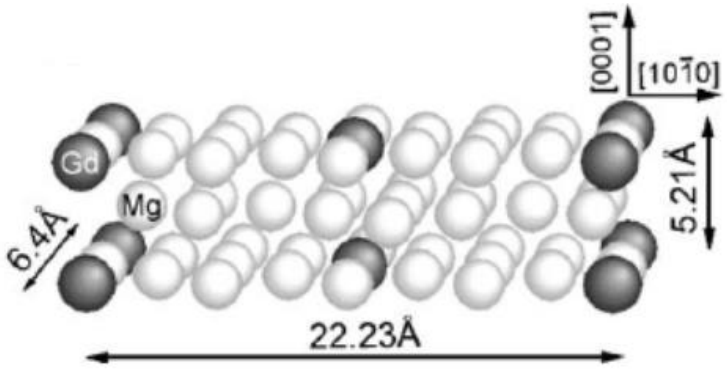

Fig. 2. 4. The atomic model of β' phase deduced from the SAED patterns. Image is taken from reference [36].

The composition of the *β'* phase based on BCO structure is $Mg_{14}RE$. Although the structural model in Fig. 2. 4 shows a based centered orthorhombic structure for the *β'* phase, further STEM analysis performed on Mg-Gd alloy showed a slightly different arrangement of solute atoms in this phase [38]. This is shown in Fig. 2.5.The difference between the two proposed structural models is that in the second model an extra layer of solute atoms is present in Z=1/2 layer and at the same positions as Z=0 layer. This arrangement of atoms results in a composition of Mg_7RE that is closer to what has been reported for *β'* from atom probe analysis [36]. On the other hand,

recent study on Mg-0.5 at% Nd showed that the lattice parameter b is quite different for different rare earth elements. The difference is attributed to dissimilar arrangement of solute atoms in the microstructure of *β'* phase. In this regard, for Mg-Nd alloy, this parameter is determined to be $b_{\beta'}$=1.11 nm.

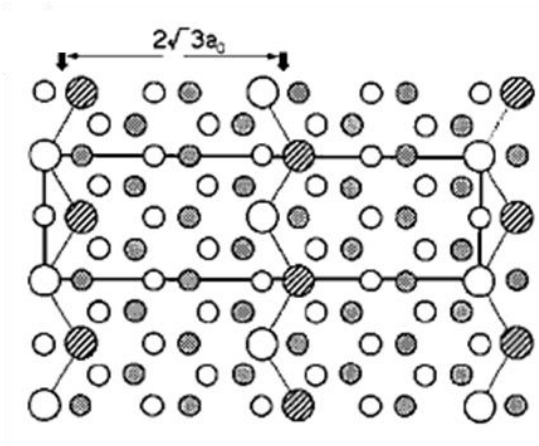

Fig. 2. 5. Schematic of the arrangement of solute atoms (Gd) in β' precipitate in Mg-Gd binary alloy [38].

The β_1 precipitates are formed on prismatic planes $(10\bar{1}0)$. The structure of this phase was determined from HREM and diffraction patterns to be FCC with $a_{\beta 1}$=0.744 nm. Fig. 2. 6. shows schematic of the structure of β_1 precipitate. As reported in literature, this phase appears at later stages of aging, mostly in over aged samples. Due to structure of this phase and the orientation with the matrix, β_1 precipitates are semi coherent with the matrix. The composition of this phase is reported to be Mg_3Nd. The EDS results acquired from this phase were consistent with the composition predicted for this phase [34].

The final precipitate in the sequence of precipitation is the equilibrium *β* phase. Similar to *β'*, different structure and lattice parameters have been reported for this phase. In a research by Pike

et al, this phase was determined as a base centered tetragonal lattice with a_{β}=1.031 nm and c_{β}=0.593 nm. The composition of β was also determined to be $Mg_{12}Nd$ [7]. However, in some research conducted on Mg-RE alloys [8, 34], a FCC structure has been reported with a=2.223 nm. The composition of β phase has been determined as Mg_5RE.

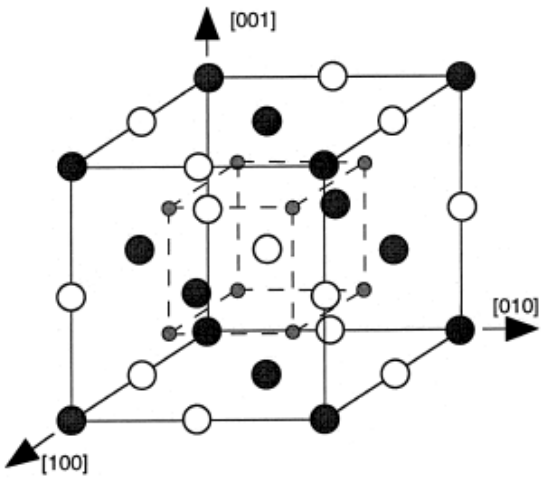

Fig. 2. 6. Schematic diagram showing unit cell of β_1 phase. Filled (large and small) circles represent Mg atoms, and open circles are Nd atoms [34].

2.4.2. γ series

There are two different reports on the structure of γ'' phase. In the TEM study on Mg- 2.8Nd-1.3Zn (wt. %) by Nuttell et al, the lattice parameter for γ'' is report to be an ordered hexagonal closed packed with $a_{\gamma''}=\sqrt{3}a_{mg}$; $c_{\gamma''}=3c_{mg}$ [9]. However, TEM and STEM analysis on a Mg-1Gd-0.4Zn-0.2Zr (at. %) showed the same lattice structure but with $c_{\gamma''}$ =0.444 nm (See Fig 2. 7.). Also the atom probe tomography (APT) investigation showed a composition of Mg-15 at. % Gd-15 at. % Zn for this phase. γ'' forms as plates on basal planes with a thickness of a single unit cell and aspect ratio of 60:1. The orientation relationship between γ'' and matrix is such that

$(0001)_{\gamma''}$// $(0001)_{Mg}$ and $[10\bar{1}0]_{\gamma''}$// $[2\bar{1}\bar{1}0]_{Mg}$ [40].

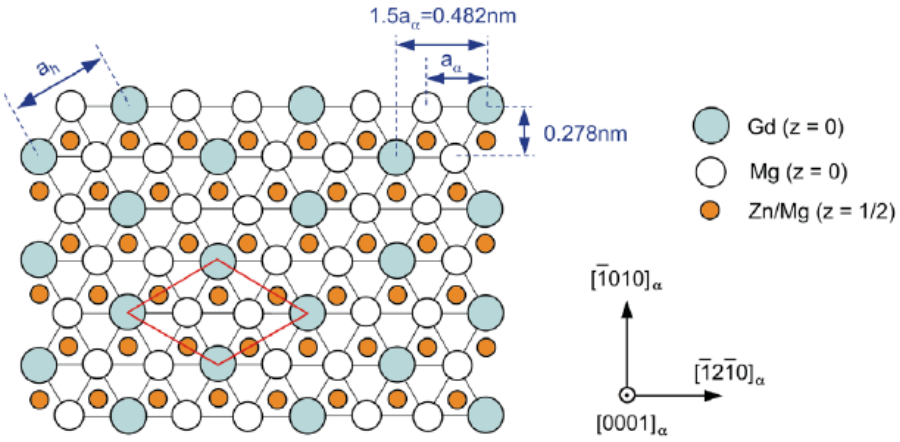

Fig. 2. 7. Schematic structure of a unit cell of *γ''* phase (marked by red lines) and its relationship with a-Mg lattice [40].

The next transition phase in the sequence is *γ'* which has been reported in Mg-Zn-RE alloys containing Gd and Nd [8, 40]. The TEM micrograph of *γ'* phase along with the proposed schematic of the *γ'* structure are shown in Fig. 2. 8. The *γ'* has a disordered HCP structure with $a_{\gamma'}$=0.321 nm and $c_{\gamma'}$= 0.781 nm. For Mg-Gd-Zn, the closely packed planes in *γ'* have ⋯ABCABC⋯ stacking sequence with Zn and Gd atoms in B and C planes. The composition of *γ'* has been reported to be the same as *γ''*. This phase also forms as plates on basal planes with a thickness of a unit cell height and very large aspect ratio. The orientation relationship between *γ'* and matrix is such that $(0001)_{\gamma''}$// $(0001)_{Mg}$ and $[21\bar{1}0]_{\gamma''}$// $[2\bar{1}\bar{1}0]_{Mg}$ [40].The thickness of this phase does not change throughout the whole aging process in such way that it remains under 1 nm for prolonged aging times [40].

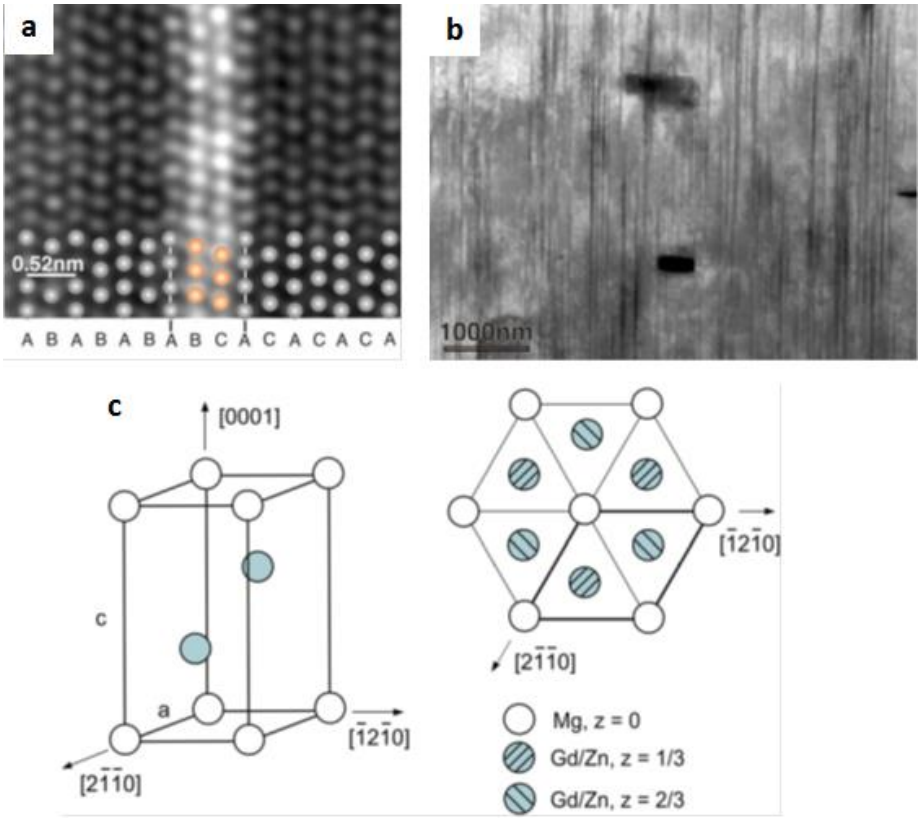

Fig. 2. 8. a) Fourier-filtered HAADF-STEM image of γ' viewed on $11\bar{2}0$; b) TEM image of γ' showing precipitates in samples aged for 1000 h at 250°C. the zone axis is $11\bar{2}0$; c) Schematic image of a γ' unit cell [40].

The proposed formation mechanism for *γ'* in Mg-Gd-Zn alloy is such that a unit cell of this phase is generated by propagation of Shockley partial dislocation (b=0.09 nm) on $\{10\bar{1}0\}$ planes. The shear strain in the vicinity of *γ'* phase that resulted from such mechanism is accommodated by formation of the second *γ'* in the vicinity of the first precipitate but with opposing shear strain. This mechanism was supported by the presence of *γ'* as pairs or clusters as seen in Fig. 2.9.

The last phase in this sequence is the equilibrium phase *γ*. This phase has an FCC structure similar to *β* with a_γ =0.744 nm. The structure and the lattice parameter of this phase are similar to the ones reported for β_1, however, the high amount of Zn and orientation with respect to the matrix are what make this phase different from β_1 [40].

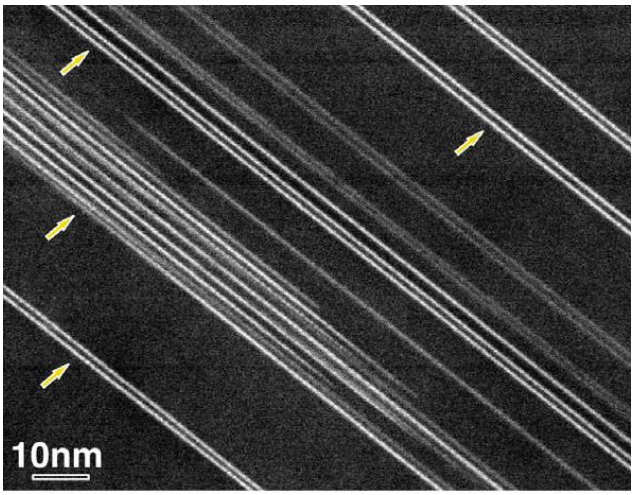

Fig. 2. 9. STEM micrograph of the sample aged at 250°C for 1000hr. The beam is parallel to $[2\bar{1}\bar{1}0]$. The presence of paired or clustered γ' precipitates is indicated with arrows.

2.5. Kinetics of precipitation

Design and development of an alloy and optimization of the processing techniques for improved performance require a better understanding of the kinetics of phase transformation and microstructure evolution during heat treatment. The progress of microstructural evolution depends on the time and temperature and can be identified experimentally. Resistivity measurements as well as thermal analysis such as DTA (differential thermal analysis) or DSC (differential scanning calorimetry) are common methods that have been used for kinetic studies of precipitation in age hardening alloys.

Quantitative determination of the reaction progress in terms of the changes in volume fraction, particle size, and number density cannot be performed easily using a single experiment. The common method for investigating this matter is quantitative transmission electron microscopy [41-44],. However, other techniques have been also used to quantify the precipitation in age-hardening alloys such as atom probe tomography (APT) [45, 46], and small angle x-ray scattering (SAXS) [47-49].

Although the aforementioned techniques are widely used to study the kinetics of precipitation in age hardening aluminum alloys, limited study has been conducted on precipitation kinetics in magnesium alloys.

2.5.1. Thermal analysis

There are different methods for calculating the kinetic parameters as reported in literature based on John-Mehl-Avrami- Kolmogorov (JMAK) relation [50-55]. The more common method is the Kissinger method which takes into account the shift of the peak position with respect to the heating rate in DSC traces of the heat treated alloys [51]. Woldt [34] proposed an extended form

of the Kissinger method which allows computing both growth parameter and the activation energy from non-isothermal curves.

According to Woldt analysis [56], for a random nucleation and an isotropic growth of m dimension in a system, the kinetics of transformation originating at t=τ can be written as the following if the extended volume is taken into account:

$$x = 1 - \exp[-\int_{\tau}^{t} g(\int_{\tau}^{t} G(\theta)d\theta)^{m} I(\tau)d\tau)] \qquad (1)$$

Where $I(\tau)$ is the nucleation rate and $G(t)$ is the growth rate. As shown in Fig 2. 10., the extended volume corrects for two things: 1) the nucleation on regions that are already transformed; 2) continuous growth of regions after impingement.

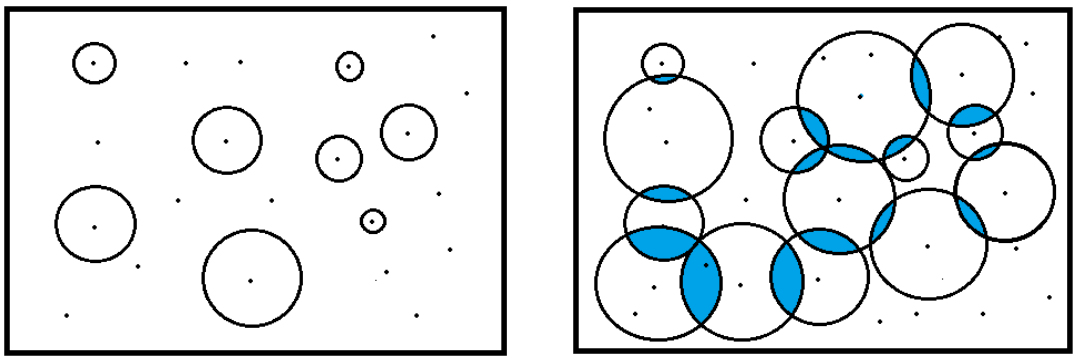

Fig. 2. 10. The schematic of the extended volume model. The shaded region shows the regions where the extended volume model is applied to.

The nucleation and growth of precipitate follow an Arrhenius behavior and can be written as:

$$I(t) = I_0 \exp(-\frac{Q_I}{RT}) \quad \text{(Nucleation rate)} \qquad (2)$$

and

$G(t) = G_0 \exp(-\frac{Q_Y}{RT})$. (Growth rate) (3)

Therefore, for non-isothermal heating where $\varphi = \frac{dT}{dt}$, equation (1) is solved and reduced to:

$$X(t) = 1 - \exp\{-gI_0G_0^3(\frac{\phi}{Q_Y})^n C \times [\frac{T^2}{\phi_i}\exp(-\frac{nQ_G+Q_I}{nRT})]^n\} \quad (4)$$

where g is a geometric constant, I_0 is the nucleation rate constant, G_0 is the growth rate constant, ϕ is the heating rate, n is the time exponent, C is a constant, T is the temperature, Q_I is the activation energy for nucleation, Q_G is the activation energy for growth, and R is the gas constant.

Rearranging equation (4) gives the following equation:

$$\ln\big(-\ln(1 - X_0)\big) = lnK_0 + n\ln[\frac{T_i^2}{\phi_i}\exp(-\frac{nQ_G+Q_I}{nRT})] \quad (5)$$

At a constant fraction X_0 for different heating rates (index i) the left side of the equation is a constant so the equation (5) can be simplified as:

$$\ln\frac{T_i^2}{\phi_i} = C_1 + \frac{nQ_Y+Q_I}{nRT_i} \quad (6)$$

The T_i here is the peak temperature at ϕ_i heating rate. Having peak temperatures at different heating rates and plotting $\frac{T_i^2}{\phi_i}$ against$\frac{1}{T_i}$, the slope of curve gives Q/nR $(Q=nQ_Y+Q_I)$. Substituting this value into equation (6) and computing for n will yield both activation energy and the time exponent for the specific transformation. In the case of site saturation, where all nuclei are present at the beginning of the process and no new nuclei are formed during the transformation, the Q_I term in the equation can be ignored and the total activation energy resembles Q_Y (growth

activation energy), therefore the slope will yield Q_Y/R. It is noteworthy that in case of continuous nucleation, the activation energy value is in fact a combination of both nucleation and growth activation energies and cannot be separated. In this case the slope value will be equal to Q/nR.

Chapter 3

3. Methods

3.1. Materials

The as-cast ingot with Mg-3 %wt. Nd-0.2 %wt. Zn-0.46 %wt. Zr composition (commercially known as NZ30K) was prepared by mixing of pure Mg, Zn, Zr, and Mg-20%wt. Nd master alloy in a 200 lb steel crucible under a protective gas mixture of SF_6/CO_2 and cast into a steel mold preheated to 200°C. The alloy melt was degassed by bubbling pure Argon for about 20 min at 740 °C, following which, the slag was removed prior to casting. The dimensions of the cast ingot was 15×10×3 cm^3.

3.2. Experimental procedure

3.2.1. Heat treatment

Samples with dimensions 10×10×5 mm^3 were cut from the ingot, polished, and cleaned in ethanol. The samples were then wrapped in tantalum foil (to prevent reaction between the

samples and the glass tube) and quickly encapsulated in glass tubes under helium atmosphere to prevent oxidation. Solution treatment of samples was performed at 540 °C for 5 hr in a horizontal tube furnace followed by quenching in water at room temperature.

Artificial aging

Solution-treated alloys were polished after quenching in water to remove the oxide from the surface, cleaned with ethanol, and placed in an oil bath at 200 °C for different lengths of time between 30 min and 64 hr. After designated aging times, samples were taken out of the bath and cooled down in air. Aged samples were mounted on AFM specimen discs and glued down to a stainless steel cylinder for hardness measurements. They were then grinded and polished using diamond polishing laps from 15 micron down to 0.1 micron. The polished samples were cleaned with ethanol and dried with air.

Natural aging

Solution-treated samples were stored at room temperature for different length of time. The mean temperature was recorded to be 22 ±3 °C. After designated times, samples were prepared and polished with the same procedure explained above for artificial aging.

3.2.2. Microhardness measurements

Microhardness measurements were performed to study the effect of heat treatment on mechanical properties of artificial and naturally aged samples as well as deformed samples. Vicker's tests were conducted at room temperature using a Wilson Tukon 1102/1202 micro-hardness tester. The Vicker's test uses a diamond tip indenter which creates a pyramidal

diamond on the surface. By measuring the two diagonals, the Vicker's hardness is calculated as:

$$H_v = \frac{2Fsin\left(\frac{\gamma}{2}\right)}{d_1 d_2}$$

Where γ is 136°, F is the load, and d_1 and d_2 are the two diagonals. 200 gr were used as the load for all measurements. For each sample with specific heat treatment condition, 10- 15 indents were performed randomly on the surface of the sample and the average was reported as the hardness. Error bars were calculated based on standard deviation of the hardness measurements on each sample.

3.2.3. X-Ray Diffraction

The crystal structure of the heat treated samples were analyzed using a Stoe (Darmstadt, Germany) and D8-Bruker high resolution (Billerica, MA) X-ray diffractometers. After heat treatment, samples were polished and cleaned before running the test. A corundum sample was used for calibration of the D8-Bruker instrument.

3.2.4. Scanning Electron Microscopy

The microstructure of the as-cast and heat treated samples were observed using a Leo 1530 scanning electron microscope (SEM) with field emission gun and equipped with energy dispersive spectroscope (EDS). The composition map of each sample was acquired using 25 kV beam. The data analysis was performed by NORAN system 7 software.

3.2.5. Differential Scanning Calorimetry

Differential Scanning Calorimetry technique was utilized to study the phase transformation,

kinetics of precipitation, and to quantitatively analyze the precipitation in aged samples at 200°C.

Phase transformation analysis

To study the phase transformation, as-quenched samples, naturally aged samples, samples aged at 130°C for different length of time, and samples aged at 200°C for different length of time were examined on a DQ100 differential scanning calorimeter (DSC) at 10°C/min. For quantitative analysis, only aged samples at 200°C were analyzed. Standard aluminum pans were used as references and to encapsulate the samples. Nitrogen gas was used as the protective atmosphere. Before each run, samples were grinded and polished to a disc shape with about 5 mm diameter and 500 micrometer thickness. In the DSC measurements the samples underwent cyclic thermal treatment (e.g. heating and cooling). The cyclic runs were repeated 3 times for each sample between 25 °C and 400 °C. The samples were held at 25 and 400 °C for 2 min upon reaching these temperatures at each cycle. The second and third cycles were used to establish a background (over-aged condition). Background for each sample was then subtracted using the third heating curve for that sample.

Kinetics of precipitation

As quenched samples were prepared following the same procedure above. Each sample was analyzed at four different heating rates of 5, 10, 15, and 20 °C/min using the same cyclic run explained above. Third heating trace was used to subtract the background. Peak temperatures were then measured and recorded for analysis.

3.2.6. Optical Microscopy

Optical microscopy was conducted to study the microstructure of the heat treated samples as well as pre-deformed aged samples. Optical microscope observations were conducted on a Motic BA310Met optical microscope equipped with light polarizer. To better show the microstructure of the alloys, samples were color etched by soaking them in a solution of 5 ml acetic acid, 6 gr picric acid, 13 ml water, and 100 ml ethanol for 25-35 seconds. Samples were washed thoroughly using alcohol immediately after removing from etchant solution and dried with air.

3.2.7. Transmission Electron Microscopy

Transmission electron microscopy and high resolution electron microscopy were used to study the microstructure and precipitation evolution in the heat treated alloys. A Philips CM200 operating at 200 kV with a resolution of about 0.18 nm and FEG-Tecnai-TF30 operating at 300 kV with a resolution of about 0.19 nm were used for TEM and high resolution purpose. A Tecnai-T12 operating at 120 kV equipped with EDS was used for TEM and diffraction pattern analysis.

For TEM quantitative analysis three aged samples were selected in accordance to hardness measurements; the 2 hr (under-aged), 8 hr (peak-aged), and 64 hr (over-aged) aged samples. The samples were prepared quickly after aging treatment in order to reduce any chance of microstructure alteration.

The wedge TEM samples were prepared using Allied Multiprep machine by using diamond lapping films with different grid sizes from 10 μm down to 0.1 μm. The wedge samples were further thinned by ion-milling. The thickness of the samples was measured by electron energy

loss spectroscopy (EELS) on regions where microstructure was analyzed. For each region three EELS runs were performed and the average thickness value was used. The absolute thickness values were extracted by measuring the beam convergence angle and EELS semi collection angle [57]. The method to calculate the angles is described in appendix 2.

3.2.8. Scanning Electron Transmission Microscopy

Scanning electron transmission microscopy (STEM) was used to study the microstructure of the aged and pre-deformed aged samples and to identify the metastable phases that evolve during aging, specifically at early stages of precipitation. Subsequently, the structure of these phases were examined and constructed. STEM analysis were performed on a TITAN microscope with Cs corrector operating at 200 kV. The Cs corrector allows achieving resolution of about 0.07 nm. Acquired images were analyzed using TIA and Digital micrograph softwares.

3.2.9. Compression tests

Compression tests were performed to study the effect of deformation on precipitation and consequently mechanical properties of the alloy. For this purpose, samples were machined into cylinders of 5 mm diameter and 7 mm height. After solution treatment and quenching in water, To study the effect of deformation on precipitation, samples were deformed to different amount of strains and subsequently aged at 200°C for desired times. A universal MTS test system (Eden Prairie, MN) was used for compression loadings. Aged samples were then cut with precision diamond saw (Struers Accutom 5) or diamond band saw to a size of about $2\times1\times1$ mm^3. The cut sample was used to make a wedge TEM sample.

The effect of twinning in age hardening alloys was investigated by performing two sets of compression tests. In the first set, samples were compressed to a certain strain, unloaded, and loaded immediately to a final strain. In the second set, samples were compressed to a certain strain, unloaded, aged at 200°C for desired times, and loaded to a final strain. The results were compared and discussed.

3.2.10. Atom Probe Tomography

Atom probe tomography (APT) technique was employed to analyze the composition of metastable phases evolved in aged and pre-deformed aged samples. APT analyses were performed on a LEAP 3000X HR (CAMECA, Madison, WI). Voltage pulse method was used with a pulse fraction of 20%, evaporation rate of 0.5% and pulse repetition of 160 Hz at 30K. Needle shaped samples were made using a Zeiss focused ion beam. The procedure for sample preparation is brought in appendix 3.

3.2.11. Electron Probe Microanalysis

Electron Probe Microanalysis (EPMA) was carried on to investigate the composition of the metastable phases in the deformed aged sample. For this purpose, an 8hr aged sample that was pre-deformed to 5% compression was mounted on an AFM disc and polished using 0.3 micron alumina powder and 0.05 micron colloidal silica. The prepared sample was analyzed using an EPMA CAMECA SX51 instrument.

Chapter 4

4. Results and Discussion

The main findings in this chapter can be summarized as follow:

1) The precipitation sequence in the Mg-Nd-Zn is somehow similar to what is reported for binary Mg-Nd alloy but with the presence of some new phases. The precipitation sequence for this alloy was identified as: *Super saturated solid solution (SSSS)→ Clusters of atoms → G. P. zones (I, II, III)* → β' → β_2 → β_1 / γ' → β.
2) Our measurements showed different lattice parameter for the β' phase with orthorhombic than the one reported for Mg-RE alloys.
3) A new intermediate phase designated as β_2 was detected in this study. This phase has not been reported previously for magnesium alloys.
4) A revised structural model was proposed for the β_1 phase. Although the structure of this phase is shown to be FCC in literature, microstructure analyses showed that the structure of β_1 is indeed BCT rather than FCC.

5) The higher yield strength of pre-deformed alloys may be associated with the pinning effect resulted from segregation of solute atoms into the defects. In addition, analysis showed that the presence of atom clusters can enhance the pinning effect of solute atoms.
6) Kinetic studied revealed that the concentration of quenched in vacancies is critical in growth kinetics of G. P. zones and β'/β_2.
7) DSC analysis of the deformed alloys revealed that the deformation enhances the kinetics of β_1 precipitation while it has slight negative effect on precipitation of prior phases. The negative effect was attributed to the annihilation of quenched in vacancies. The positive effect on β_1 precipitation was attributed to the effect of shear strain, caused by basal dislocations and twins.

In the following sections, these findings are presented and discussed in details.

4.1. Solution treatment

Fig. 4. 1. (a) shows BSE image and EDS maps of an as-cast sample. The brighter region in BSE image is the eutectic product which is distributed on grain boundaries. This phase appears during casting and is enriched in neodymium and zinc as seen from EDS map. In literature the composition of this phase in a binary Mg-Nd alloy is reported to be $Mg_{12}Nd$ [7]. In addition, a distribution of small particles enriched in Zr can be detected within the grains. These particles are intermetallic of Zr and Zn which form during casting at high temperature and act as grain refiner in this alloy [8].

Fig. 4. 1 (b) shows BSE image and EDS maps of a solid solution treated alloy. As seen in the BSE image as well as in EDS maps, the eutectic product is no longer present in the

microstructure which confirms a good condition for solution treatment. However, the Zr-rich particles are still visible within the grains. These particles are randomly oriented with the matrix and are on the order of 50-300 nm, as was observed by TEM (Fig. 4. 2).

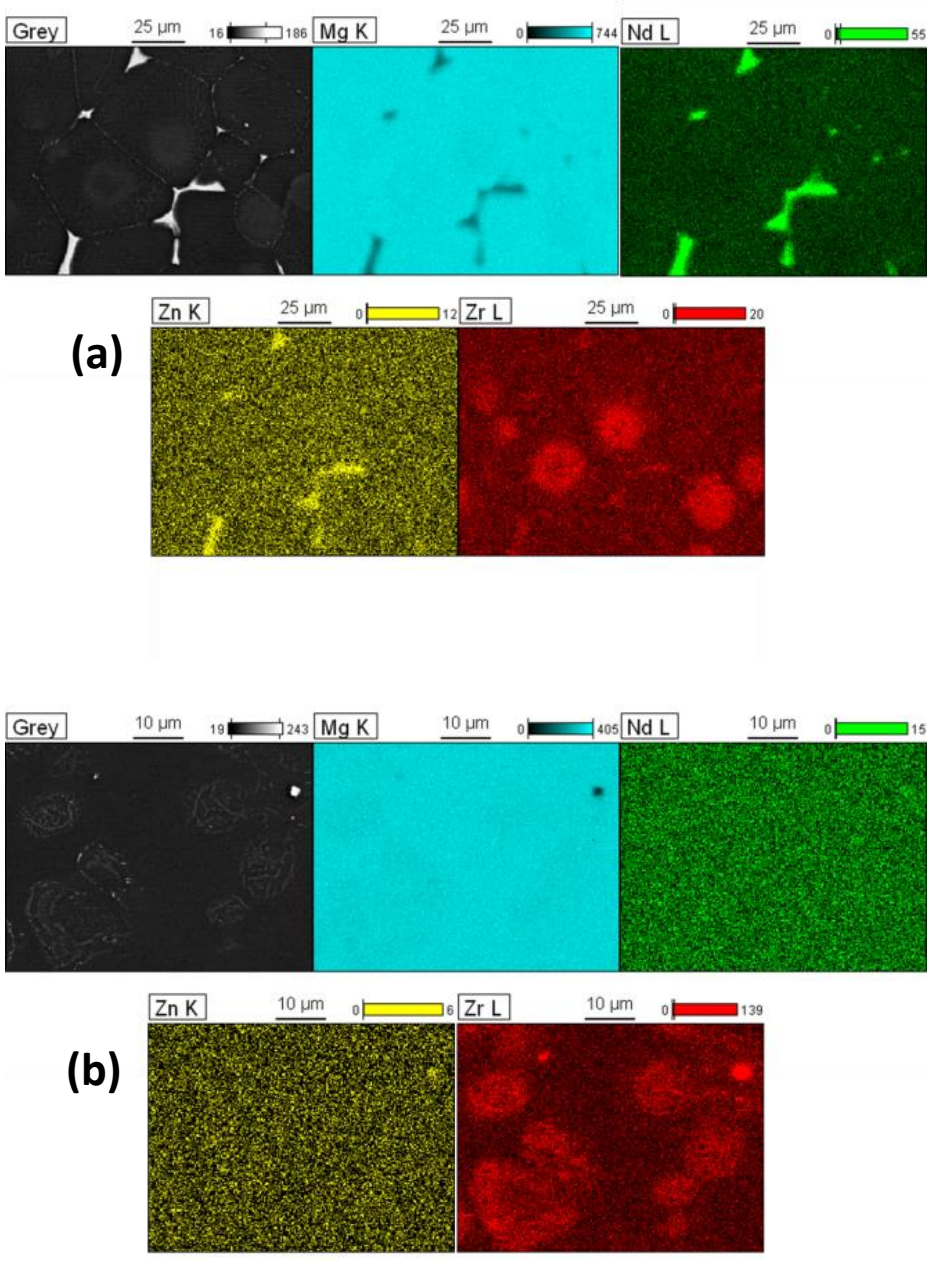

Fig.4. 1. BSE image and elemental maps acquired from EDS for a) as-cast and b) as-quenched samples. The concentration of neodymium and zinc on grain boundaries is visible in as-cast sample. These phases disappear after 5hr of aging at 540°C as seen in Fig. 4. 1 b.

Since these particles form during casting and at temperatures around 700°C, their concentration remains unchanged during solution treatment at 540°C. The presence of Zr-rich phase does not alter the aging behavior of the alloy due to stability of the phase at the aging temperature [8].

In terms of aged alloys, the microstructure did now show any evidence of the precipitates, and the microstructures were similar to as-quenched sample. EDS and electron probe microanalysis (EPMA) also were not able to detect any compositional difference with the matrix due to small size of the precipitates.

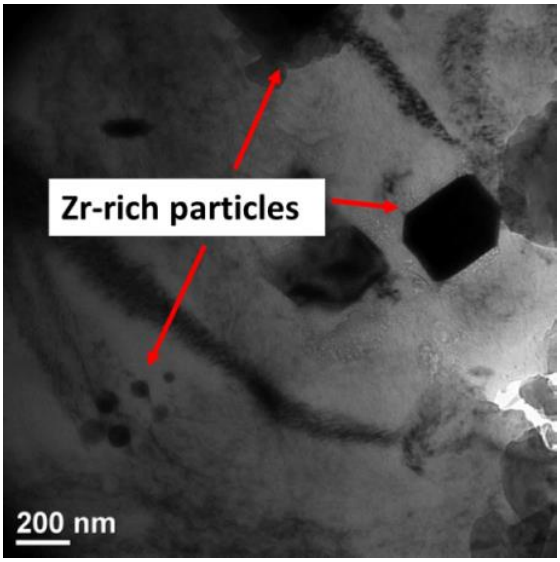

Fig. 4. 2. Bright field TEM of zirconium particles in an as cast sample of Mg-3Nd-0.2Zn. The particles are distributed within the grains.

4.2. Age hardening

Fig. 4. 3. shows the hardness values obtained from samples naturally aged at room temperature. As seen the hardness of the samples increases slightly after 76 days. That implies very slow precipitation kinetics at room temperature for the studied alloy. However, aging at higher temperatures (artificial aging) has shown significant age hardening effect. In this regard, solution treated samples were aged at 200°C for different length of time and hardness measurements were performed on each aged alloy. The results are presented in Fig. 4. 4. The hardness values are compared with some reported measurements in previous works for the same alloy (NZ30K) [1, 8, 26]. As seen from the graph, the peak hardness occurs at aging times between 4-8 hours. This is consistent with the trend reported previously for the same alloy [1, 8, 26], although the aging time for maximum peak hardness is slightly different in some of the other research [1, 26].

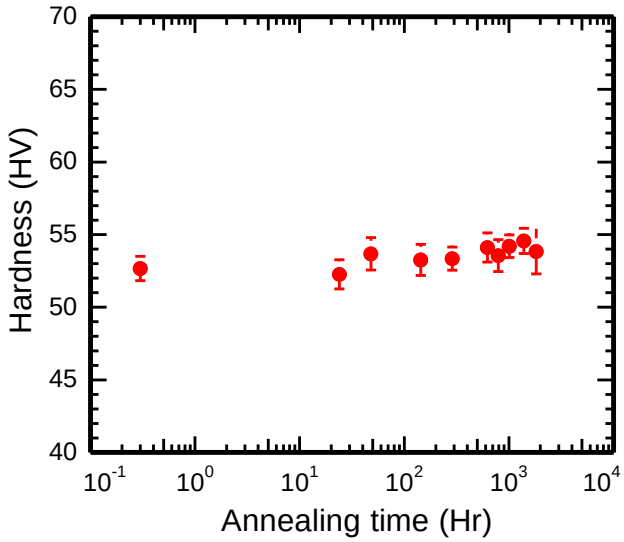

Fig. 4. 3. Hardness vs. annealing time for the Mg-0.2 wt. %Zn- 3 wt. % Nd samples naturally aged at room temperature.

The interesting point is that the maximum hardness in this work is about 12% higher than reported values for this alloy. This might be due to different sample preparation conditions such as our pre-aging of the sample at 273 K for 24 hours. The pre-aging is known in other systems to promote clustering in the solid solution leading to higher densities of nuclei during heat treatment [21]. In addition, quenching in water at room temperature (~22 °C) vs. hot water (~70 °C) in the other works (i.e. ref. 8 and 13) can result in faster quenching rate and higher vacancy concentration in the samples studied here. These vacancies play significant role in precipitation, especially in early stages of precipitation and in the formation of clusters of atoms or G.P. zones [7, 9]. Other factors such as different casting or extrusion conditions, which lead to different grain structure, can affect the hardness readings as well.

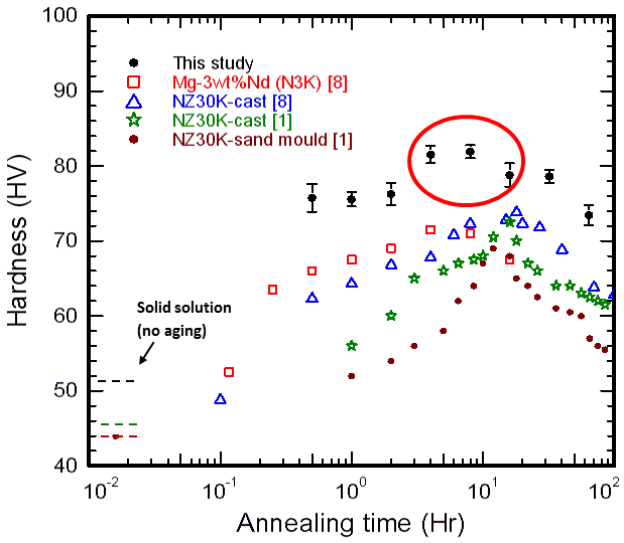

Fig. 4. 4. Hardness vs. annealing time for the Mg-0.2 wt. %Zn- 3 wt. % Nd samples aged at 200°C. Reported values for the same alloy are presented from literature for comparison [1, 8, 26].

4. 3. TEM analysis of microstructure

Fig. 4. 5. shows a background-subtracted DSC curve acquired at 10 °C/min heating rate from an as-quenched sample. A quick look at the DSC trace reveals the presence of three exothermic peaks and 2 endothermic peaks, as identified in the graph. A closer examination of the graph also shows that the first exothermic peak is composed of small overlapping exothermic peaks. In addition, the second exothermic peak contains two overlapping peaks. The first endothermic peak at around 470K appears to be due to dissolution of the phases that formed during first peak (i.e. peak A). Similarly, the second endothermic peak (peak E) results from the dissolution of the phases that formed during peak C and D.

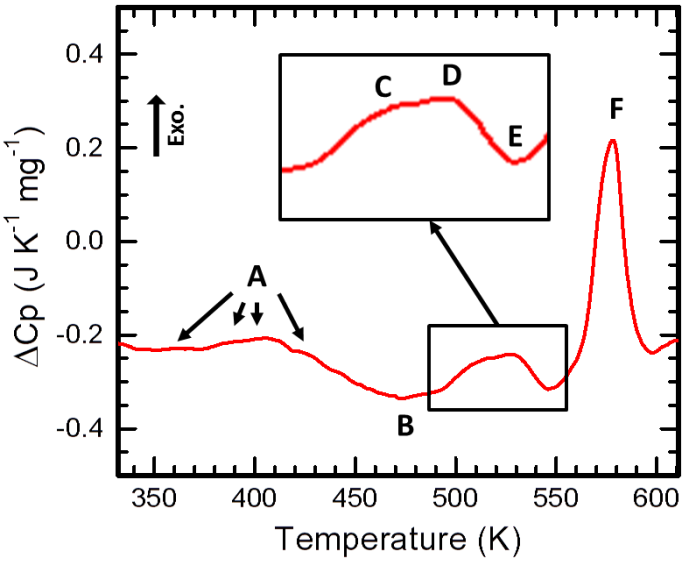

Fig. 4. 5. DSC curve of solution treated sample at 10 °C/min. Three exothermic peaks and two endothermic peaks are present in the trace.

To better understand the significance of each peak, three different aging treatments were performed at temperatures close to the temperature of each peak. The microstructures of each sample were studied using TEM and HREM. The first treatment was done on a sample at 140°C

(~410 K) for 15 minutes. The corresponding microstructure is shown in Fig. 4. 6 (a). For this sample, the bright field images did not reveal any precipitation of the second phase in the matrix. However, HREM images showed the presence of some dark spots (Fig. 4. 6. (b)) as well as weak streaks on prismatic planes (i.e. $(1\bar{2}10)$) that were distributed in some grains (Fig. 4. 6. (c)). These streaks are on the order of 1-2 atomic layer thick and about 5-10 nm long. The corresponding diffraction patterns at different zone axes did not show any signature or extra spots related to the second phase [58, 59]. Previous researches on similar systems [60-62] have shown that the first peak can be attributed to either formation of clusters of solute atoms in the matrix or G. P. zones. The presence of the dark spots as well as weak streaks in HREM observations of the aged sample may be evidence to formation of clusters or G. P. zones in this aging condition.

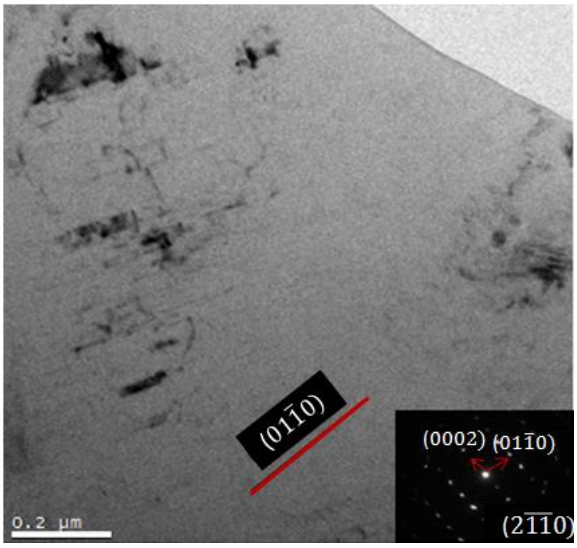

(a)

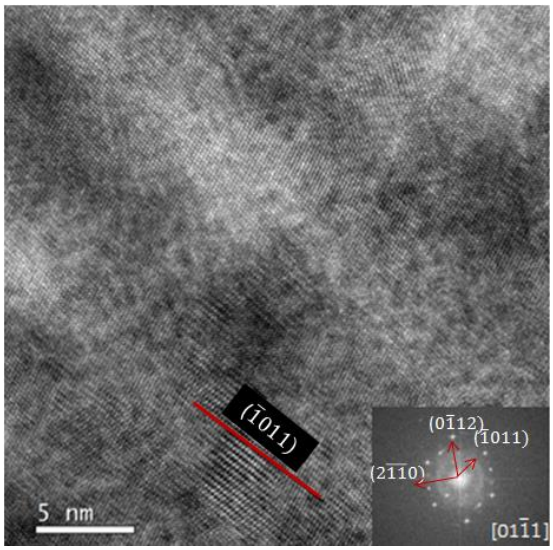

(b)

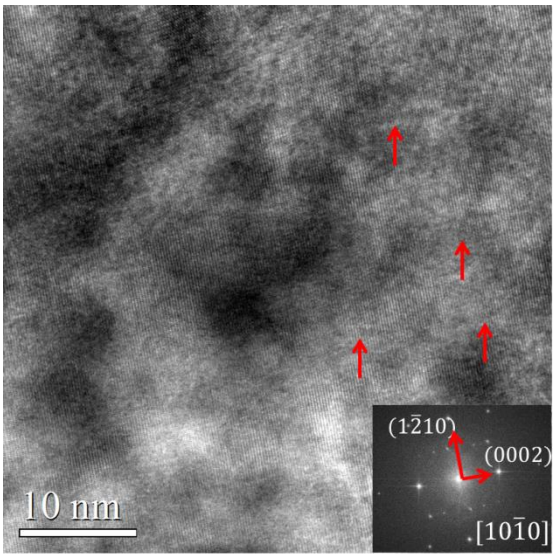

(c)

Fig. 4. 6. (a) TEM micrograph of the solid solution treated sample, aged at 140°C for 15 minutes. The beam is parallel to: (a) [1$\bar{2}$10] zone axis, (b) and (c) HREM images of the sample aged at 140°C for 15 minutes. The beam is parallel to [01$\bar{1}$1] and [10$\bar{1}$0]zone axes respectively.

The second heat treatment was performed at 250°C (~520K) around the second exothermic peak temperature for 5 minutes. We chose a shorter aging time for this sample because the second peak occurs close to the third peak, therefore, shorter time can help to avoid the formation of the third type precipitate. Figs. 4. 7. (a)-(f) show TEM and HREM images of the precipitates in the sample on [$\bar{2}$4$\bar{2}$3], [0001] and [01$\bar{1}$0] zone axes, respectively. Figs. 4. 7. (a) and (b) taken on [$\bar{2}$4$\bar{2}$3] and [0001] zone axes confirm the existence of these precipitates on prismatic planes type I (i.e. (10$\bar{1}$0)). Fig. 4. (c), taken with beam parallel to [01$\bar{1}$0] direction, shows that this type of precipitation also occurs on prismatic (1$\bar{2}$10) planes (type II). As reported in literature, these orientations with respect to the matrix (prismatic precipitation of type I and II), and the size range are signatures of *β"* and *β'* precipitates with D019 ($a_{\beta"}=2a_{Mg}$ and $c_{\beta"}= c_{Mg}$) and BCO ($a_{\beta'}$ =0.642 nm, $b_{\beta'}$=2.223 nm, $c_{\beta'}$=0.521 nm) structures, respectively [7, 8]. The primary conclusion was that both β" and β' precipitates are present in the microstructure at this condition, although

no extra spots from precipitates were observed in the corresponding diffraction patterns.

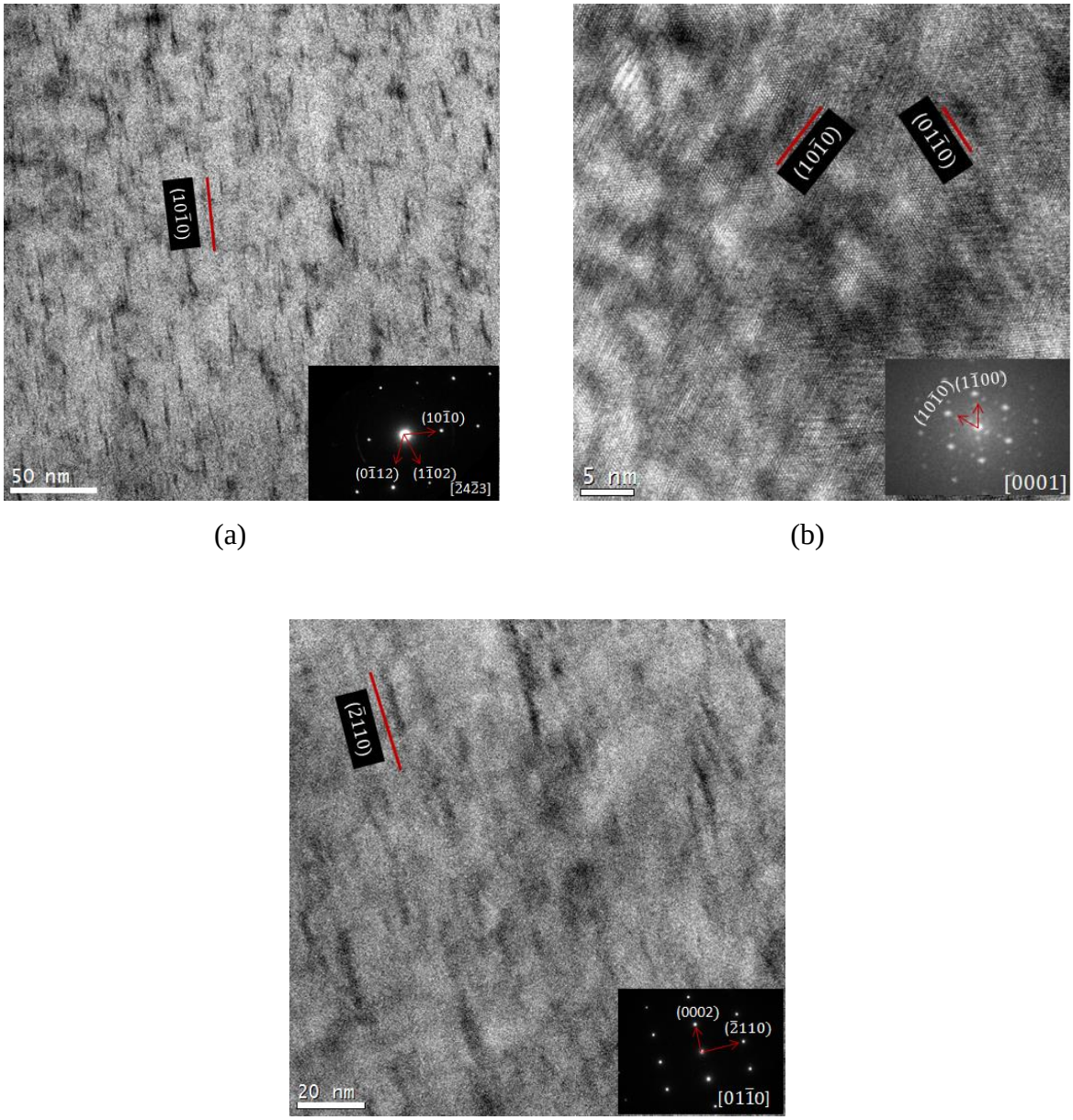

Fig. 4. 7. TEM micrographs of the sample aged at 250°C for 5 minutes: (a) BF image with beam parallel to $[\bar{2}4\bar{2}3]$; (b) HREM image with beam parallel to [0001]; (c) HREM image with beam parallel to $[01\bar{1}0]$; (d) BF image with beam parallel to $[01\bar{1}1]$; (e) BF image with beam parallel to $[1\bar{2}1\bar{3}]$; and (f) HREM image of β" precipitate with beam parallel to $[1\bar{2}1\bar{3}]$ zone axes.

The third heat treatment was performed at 300°C for 30 minutes. Figs. 4. 8. (a)-(c) show bright field TEM images of this sample taken with beam parallel to $[1\bar{2}1\bar{3}]$, $[\bar{2}4\bar{2}3]$ and $[1\bar{2}10]$ directions, respectively. According to the corresponding selected area diffraction pattern (SADP), these precipitates are in the form of plates that lie on $\{10\bar{1}0\}$ planes. The size of these precipitates varies from less than 100 nm to 500 nm in length and 10 - 30 nm in thickness.

In addition, extra spots were observed in the diffraction pattern acquired from $[\bar{2}4\bar{2}3]$ zone axis (Fig. 4. 8. (b)). HREM analysis of these precipitates (see Fig. 4. 8. (d) and (e)) revealed that the extra spots belong to the second phase in the matrix. The orientation, size, and Bravais lattice of the detected phase is consistent with β_1 phase reported in Mg-RE alloys [8, 34]. β_1 is a semi-coherent phase and has a face centered cubic (FCC) structure with $a_{\beta 1}$ =0.74 nm [8, 34].

Furthermore, HREM images showed that this phase is coherent in $[10\bar{1}0]$ direction of the matrix but there is a slight misorientation (about 5°) in $[1\bar{1}02]$ direction. It is evident from the corresponding fast Fourier transform (FFT) of the image (Fig 4. 8. (c)) that β_1 has a larger lattice parameter that leads to loss of coherency as the precipitate grows.

The final phase in the sequence of precipitation in Mg-RE system is the equilibrium β phase [7, 8 34]. In this research, β phase was detected on some grain boundaries after 30 minutes of annealing at 300°C as shown in Fig. 4. 8. (f). However, no evidence of the precipitation of this phase within the matrix was found. Another interesting feature in the microstructure was the presence of precipitate free zone (PFZ) with ~200 nm thickness at both sides of the grain boundaries. PFZs are attributed to depletion of vacancies and solute atoms near grain boundaries during aging [63].

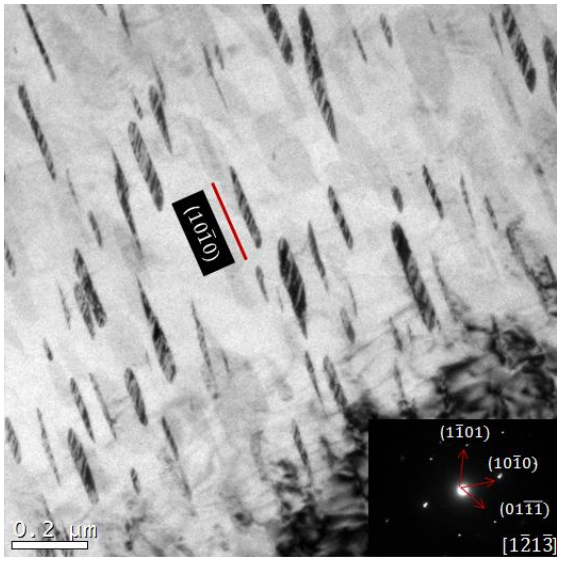
(10$\bar{1}$0)
(1$\bar{1}$01)
(10$\bar{1}$0)
(01$\bar{1}$$\bar{1}$)
[1$\bar{2}$1$\bar{3}$]
0.2 μm

(a)

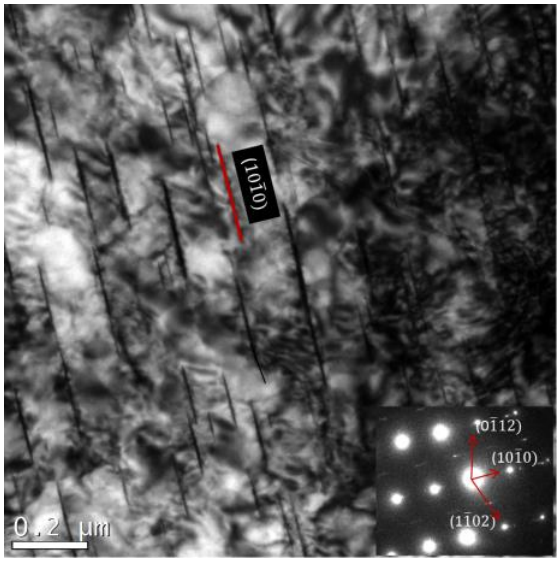
(10$\bar{1}$0)
(0$\bar{1}$12)
(10$\bar{1}$0)
(1$\bar{1}$02)
0.2 μm

(b)

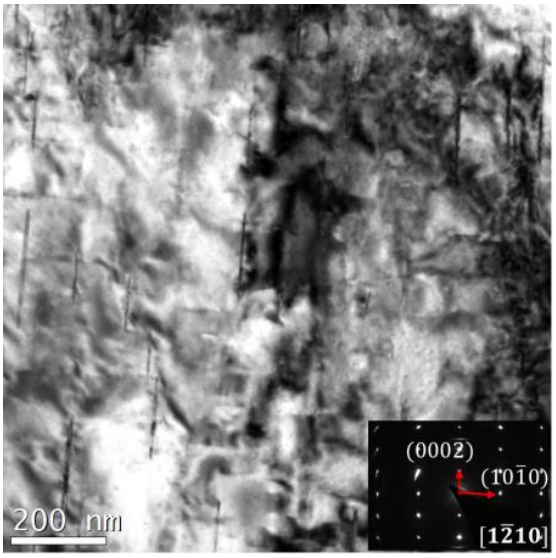
(0002)
(10$\bar{1}$0)
[1$\bar{2}$10]
200 nm

(c)

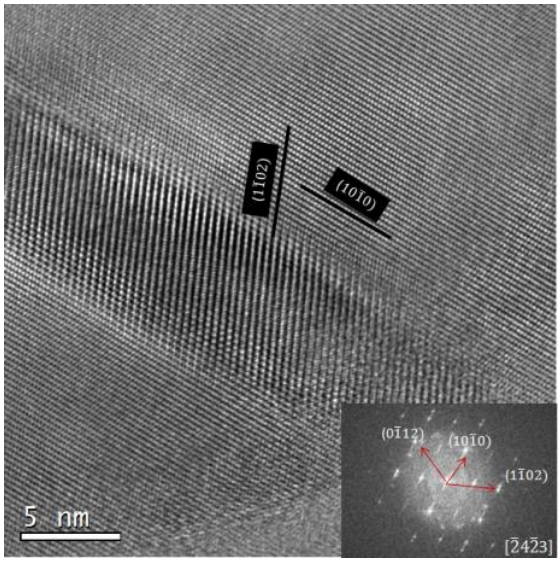
(20$\bar{1}$1)
(10$\bar{1}$0)
(0$\bar{1}$12)
(10$\bar{1}$0)
(1$\bar{1}$02)
[$\bar{2}$4$\bar{2}$3]
5 nm

(d)

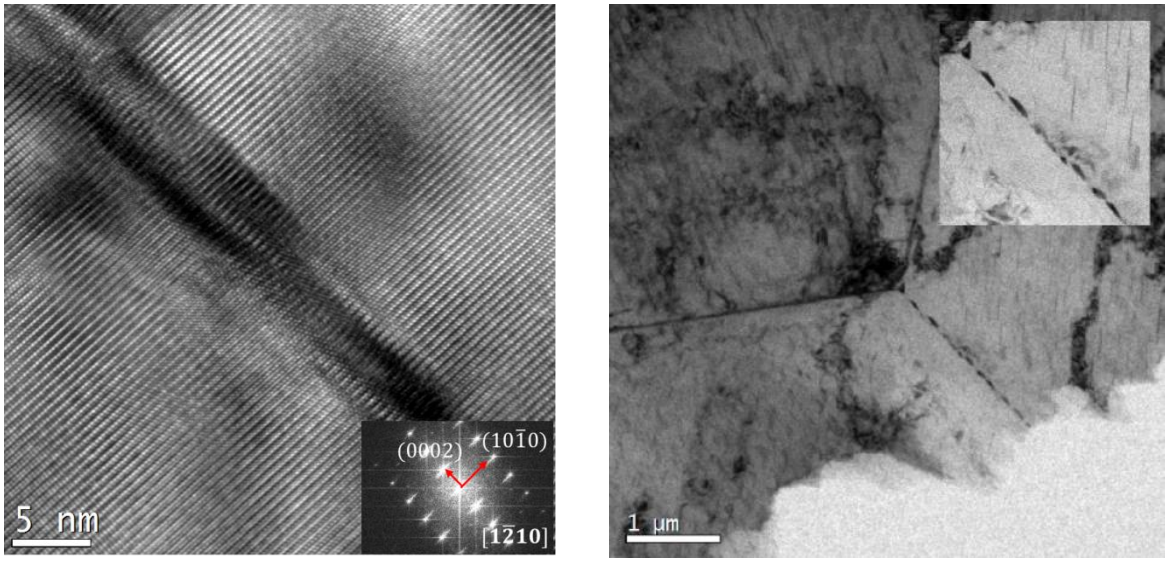

(e) (f)

Fig. 4. 8. Bright field TEM images of the sample aged at 300°C for 30 minutes taken with beam parallel to: a) [1$\bar{2}$1$\bar{3}$] and b) [$\bar{2}$4$\bar{2}$3] zone axes; (c) HREM image of the sample with beam parallel to [$\bar{2}$4$\bar{2}$3] zone axis; (d) image of a triple joint in Mg matrix. *β* precipitates are visible on grain boundaries.

It should be noted that in a few grains, an uneven distribution of needle shape precipitates was found as shown in Fig. 4. 9. (a) and (b). These precipitates lie on basal planes (0001) and are 20-30 nm long and 3 atomic layers thick. The orientation of these precipitates with the matrix and their structure are signatures of *γ'* reported in Mg-Zn-Nd and Mg-Zn-Gd system [8, 40]. The length of these precipitates is shorter than the reported length in Mg-Zn-Gd system but it is close to the one reported in Mg-Zn-Nd system. The strong strain contrast around each precipitate shows that these precipitates are coherent with the matrix. The structure of this phase is hexagonal with $a_{\gamma'}$ = 0.321 nm and $c_{\gamma'}$ = 0.781 nm [8, 40].

A primary conclusion from DSC and TEM results showed that the sequence of precipitation in this system can be described as clustering of atoms or short range ordering → *β''*/ *β'*→ *β1*/ *γ'* → *β*. This sequence is the same as the one reported in Mg-Nd [7] except in this system *β1* and *γ'*

precipitates were detected in later stages of precipitation. However, the sequence is completely different from the one reported for Mg-Nd-Zn alloy with higher zinc content (i.e. more than 0.5 wt. %) [9]. Due to coherency of the evolving phases especially at early stages of precipitation and complex contrast in TEM images, we were not able to deduce information on the structure and arrangement solute atoms in these phases. Therefore, STEM analyses were performed on aged alloys to further investigate this matter. The results are shown and discussed in the section 4.5.

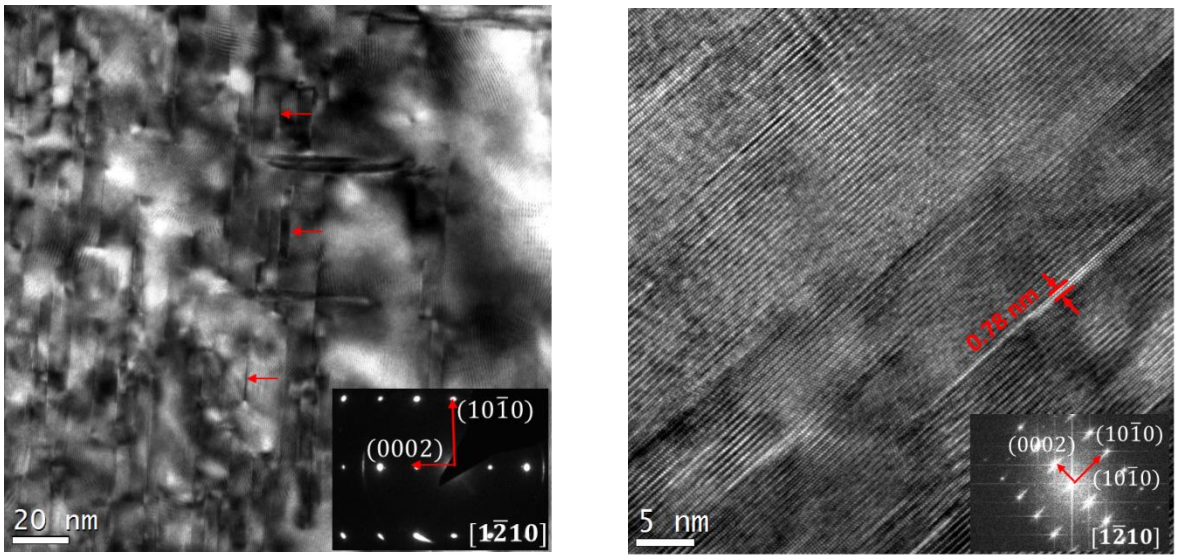

(a) (b)

Fig. 4. 9. Bright field TEM images of the γ' in the matrix for sample aged at 300°C for 30 min. Images are taken with electron beam parallel to [1$\bar{2}$10].

4.4. DSC analysis of aged alloys

The DSC traces of samples at three different heat treatment conditions were obtained. Fig. 4. 10. shows the DSC graphs of the samples naturally aged for different length of time. As seen from the graphs, there is not a significant change in the height and width of the exothermic and endothermic peaks with increasing aging time. This behavior is in agreement with the results of microhardness tests and indicates that natural aging for this alloy is a very slow process.

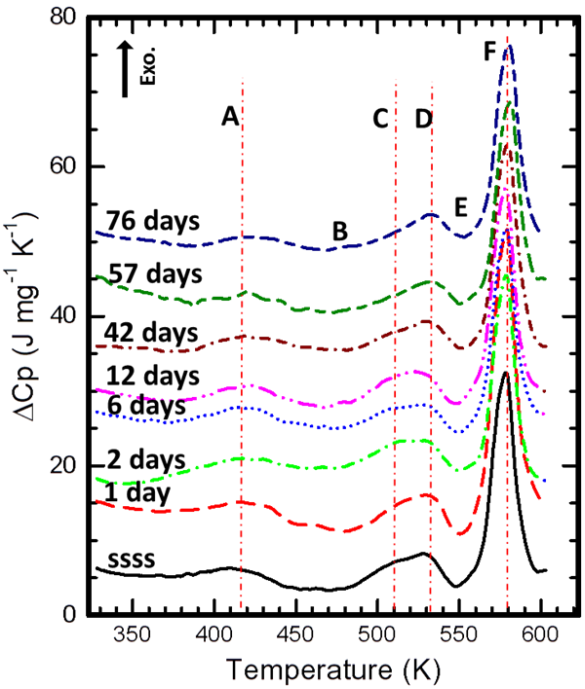

Fig.4. 10. DSC traces of samples naturally aged for different length of time. The DSC experiments were conducted at 10°C/min.

Although there is no report on studying the clustering of atoms in Mg alloys, for age-hardening aluminum alloys, the clustering of atoms is evident in DSC traces after 1 week natural aging [64-68]. The absence of such evidence after 10 weeks in our system may indicate that the clustering of atoms in this system either involves a very small amount of heat evolution that cannot be

resolved by DSC or the clustering does not happen for this system. Clustering phenomena has not been reported previously for magnesium alloys containing neodymium. It was postulated then that the first peak is mainly related to the formation of a second phase in the matrix, although formation of clusters of atoms is possible.

As the aging temperature increases, the kinetics of precipitation accelerates. This is evident in the DSC traces of samples aged at 130°C (see Fig. 4.11). The DSC trace of as-quenched sample shows the presence of an exothermic peak around 400K (~130°C). This peak diminishes as the aging starts and disappears after 30 mins aging. On the other hand, the height and width of the exothermic peaks D and F remain unchanged throughout the aging. This condition implies that the microstructure mainly contains the first type precipitate and formation of the second and third type precipitates do not happen at this aging condition. Our earlier observations of the microstructure of the sample aged at 140°C (Fig. 4. 6.) showed the possible presence of G. P. zones in the matrix. Therefore, it can be postulated that at this aging condition, microstructures mainly contains G. P. zones.

The endothermic peak B, which is a broad peak at as-quenched state, starts to become sharper and narrower as the aging proceeds to longer times. The width of the peak is associated with the size distribution of the second phase. Therefore, at the beginning of the precipitation, a wide size distribution of the second phase is present in the matrix. However, by increasing aging time and the growth of the precipitates, a more uniform size distribution of the precipitates is achieved. In addition, an observed shift in the position of the endothermic peak implies an increase in the size of the precipitates with prolonged aging times [69].

As seen earlier, aging at 200°C resulted in significant increase in the microhardness of the as-

quenched alloy. DSC analysis of the samples at 200°C (Fig. 4.12) showed that the precipitation kinetics at this temperature is significantly higher than the other two aging conditions.

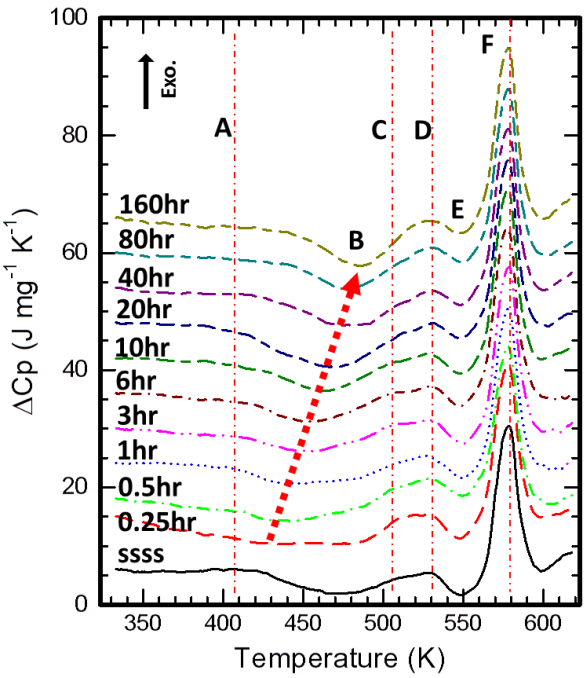

Fig.4. 11. DSC traces of samples aged at 130°C for different length of time. The DSC experiments were conducted at 10°C/min.

The first exothermic peak, associated with clustering of atoms or formation of G.P. zones (~140 °C) [25], is present on the DSC trace of as-quenched sample as well as samples aged up to 2 hr. The height of the peak decreases as the aging starts and completely disappears after 1hr aging time. In contrast, the heat evolution associated with the endothermic peak B increases as the aging proceeds to longer times. In addition, the position of the Peak B changes due to increase in the size of the precipitates.

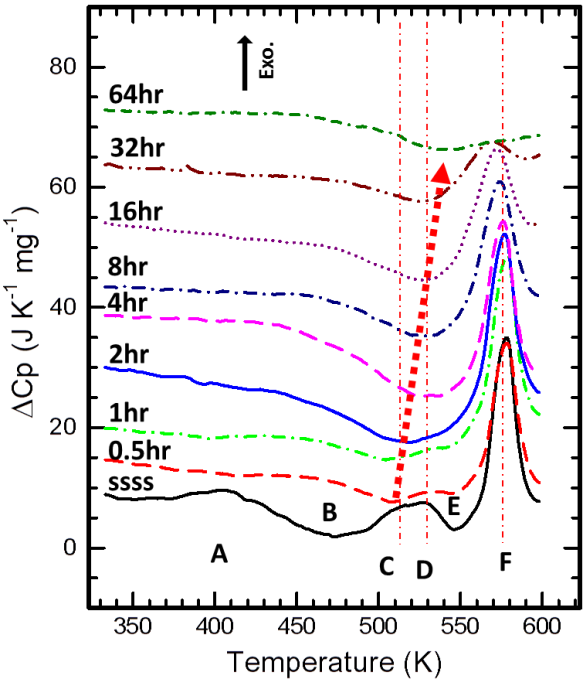

Fig.4. 12. DSC traces of samples aged at 200°C for different length of time. The DSC experiments were conducted at 10°C/min.

In terms of the exothermic peaks C and D at around ~250 °C (520 K), the height of the peaks significantly decreases after 30 min of aging which implies the formation of the second phase during the first 30 mins of aging at 200°C. The exothermic peak D completely diminishes after 2hr aging time and is replaced with an endothermic peak. The endothermic peak can be associated with the dissolution of the precipitates formed during isothermal aging or during initial heating in DSC. In other words, although the endothermic peak B is initially related to the dissolution of the G. P. zones or clusters, the dissolution of the second phase (formed during aging) in co-existence with G. P. zones/clusters would lead to a continuous shift of the endothermic peak to higher temperatures. Since all phases co-exist in the microstructure of the under-aged alloys prior to heating in DSC, it is not possible to deconvolute the dissolution peak associated with G. P. zones, clusters, and the second phase.

The third exothermic peak is centered at around 570K (300°C). The height of the peak does not

change until 8hr aging which implies that the third phase is not present significantly in the matrix. However, as isothermal aging proceeds to 8hr aging and longer, the height of the peak starts to decrease and at 64hr completely disappears. The decrease in the heat evolution with increasing aging times is due to presence of the third phase in the aged alloy which leads to a lower potential for precipitation of this phase during heating in DSC.

4.5. STEM analysis of the aged alloys

4.5.1. Under-aged condition

To better understand the origin of each peak and the sequence of precipitation in this alloy, three samples aged at 200°C for different length of time were chosen for STEM analysis; the 2hr aged sample (under-aged condition), the 8hr aged sample (peak-aged condition), and the 64hr sample (over-aged condition). Fig. 4. 13. (a) and (b) show the low angle bright field and high angle annular dark field (HAADF) images of the sample aged at 200°C for 2hr. The images are taken with the beam parallel to [0001] direction.

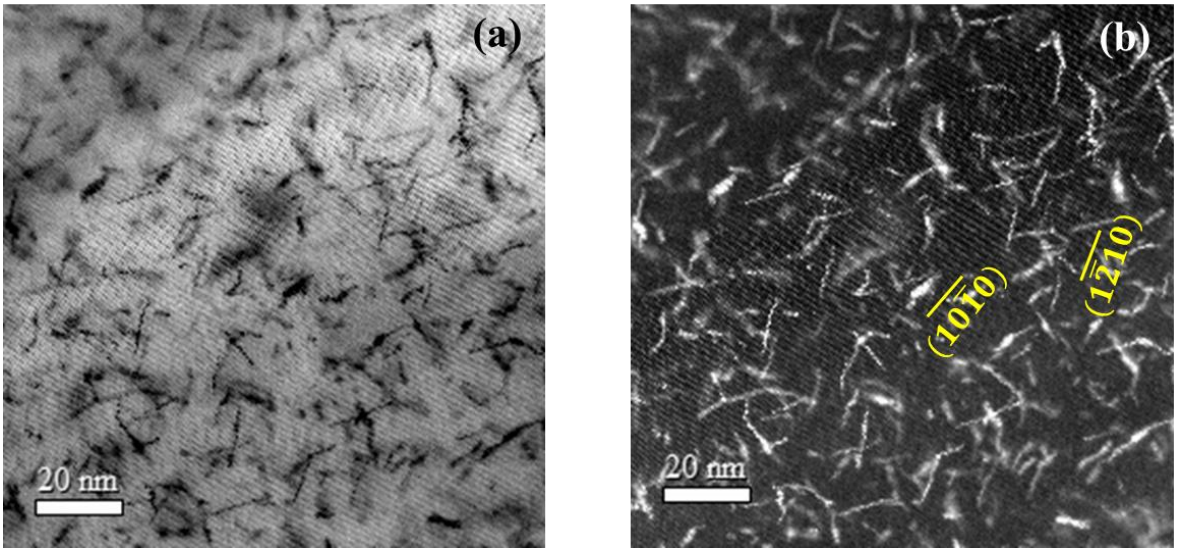

Fig.4. 13. STEM micrographs taken from sample aged at 200°C for 2hr: a) low angle dark field image; b) high angle annular dark field image. The beam is parallel to [0001] direction.

Precipitates are on both types of prismatic planes; however, the image contrast is different from one precipitate to another. Higher contrast in STEM images can be associated to presence of heavier solute atoms (i. e. higher atomic number) or larger quantity of heavy solute atoms in the

precipitates. A closer examination of the macrostructure revealed the presence of four distinct structures in the microstructure. This is shown in the high resolution HAADF image in Fig. 4. 14. as marked regions 1- 4. The first structure, marked as 1, is a very thin precipitate that is a few nanometers thick and has discontinuity along the phase. The second structure is an ordered structure with discontinuity normal to the long axis of the phase and with higher thickness than the first phase. The third type has specific arrangement of atoms such as hexagons and is denser compared with the first two types. The fourth structure is however more packed and has the highest contrast with the matrix. In the following, each phase was analyzed and discussed in more details.

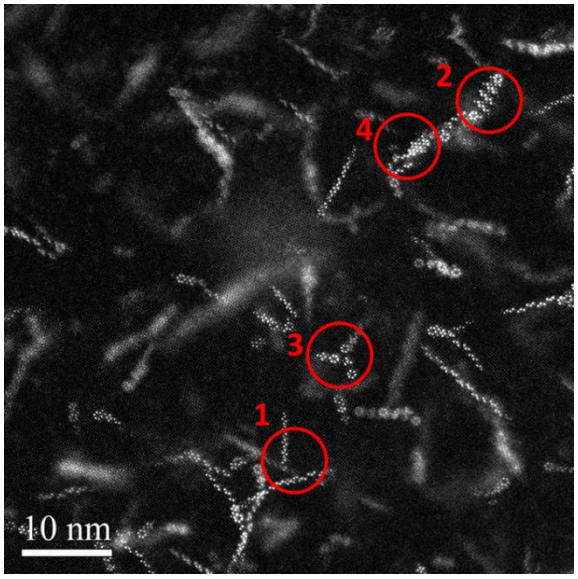

Fig. 4. 14. High resolution HAADF-STEM image of the sample aged at 200°C for 2hr. Four distinct features are visible in the microstructure.

First type

The FFT image taken from the region containing this phase (see Fig. 4. 15.) shows a D019

structure arrangement of the atoms [36, 37]. However, no complete unit cell of a D019 structure was found for this type of precipitate. To further analyze this phase and the corresponding structure, high resolution HAADF images from three zone axes were obtained from the 2hr aged alloy at 200°C. The images were then modeled to obtain the position of the solute atoms in the matrix and consequently the structure of this phase. The results are brought in Fig. 4. 16. (a)-(f). In the modeled structure, Mg atoms in layer Z=0 and Z=1/2 are shown with small yellow and red spheres and Nd atoms in layer Z=0 and Z=1/2 are displayed with larger blue and purple spheres.

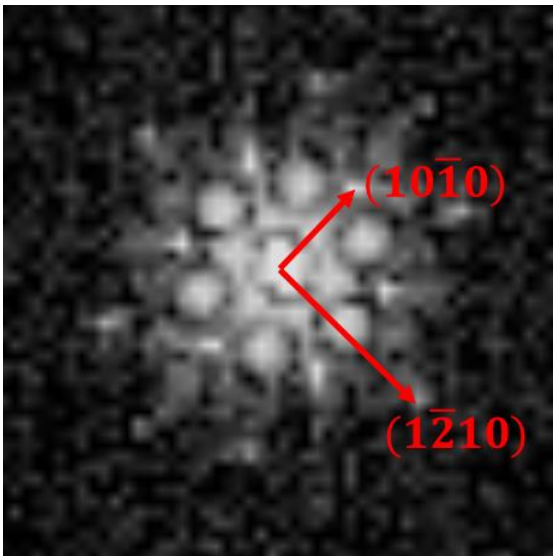

Fig. 4.15. FFT image of the region containing first type precipitate in the sample aged at 200°C for 2hr. The diffraction spots show a D019 orientation of atoms.

As seen in Fig. 4. 16. (a), this phase has a discontinuous ordered structure along prismatic directions. In addition, no periodic arrangement of atoms in a wide range in {0001} planes is seen for this phase throughout the matrix.

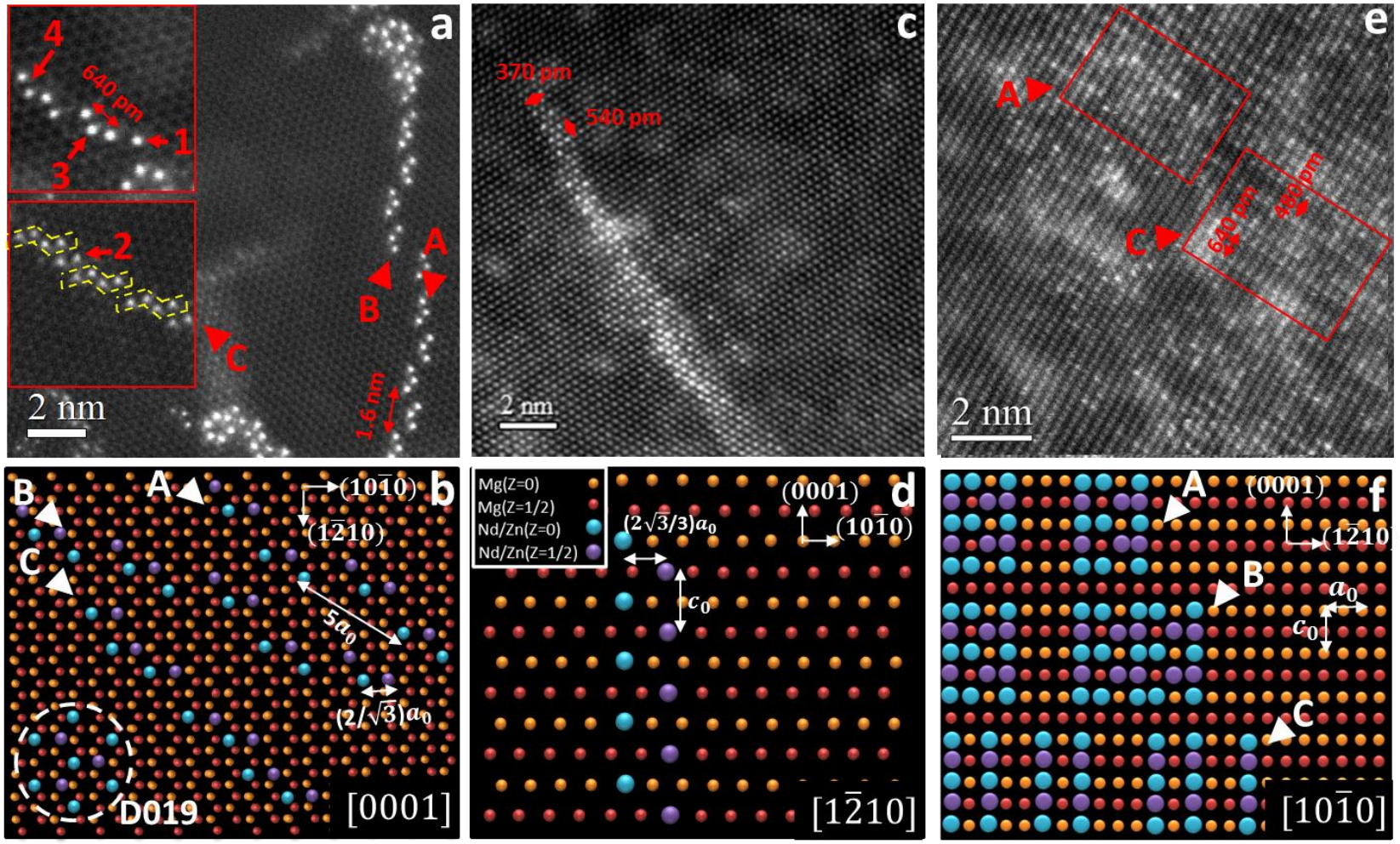

Fig. 4. 16. High resolution HAADF-STEM images and corresponding modeled atomic arrangements for the first type precipitate in the alloy aged at 200°C for 2hr. The beam is parallel to: a) and b) [0001] direction; c) and d) [1$\bar{2}$10] direction; e) and f) [10$\bar{1}$0] direction. In the modeled structure, Mg and Nd atoms at different layers are denoted with smaller and bigger circles and different colors

The arrangement of atoms in this phase range from 1 atomic column component to a series of 2, 3, and 4 atom columns components. The position of solute atoms in components with more than one atomic column is such that they occupy the second nearest neighbor in the matrix on prismatic planes. The components containing 3 and 4 atom columns have a D019 arrangement (shown in Fig. 4. 16. (b) inside the dashed circle) with 0.37 nm intervals between atom columns, as reconstructed in the model structure in Fig. 4. 16. (b). The shape of these components is obtained by replacement of Nd atoms with Mg atoms in HCP lattice positions in the first and second layer. The arrangement of the components varies in the chain from all 3 to a combination of 1, 2, 3, and 4 atom columns components. However, three main combinations were found as shown in Fig. 4. 16. (b). These combinations include all three (A), 3-3-3-4-4 (B), and 4-4-4-2 (C). The atomic distance between repeating components is different in each type of combination. For A and B type chains, the distance between repeating three atom columns components is 1.6 nm ($5\times a_0$). However, the distance between 4 atom column components in B type chain reduces to 850 pm. In C- type chain, the distances between 4-4 combinations varies to 550 and 850 pm and for 4-2 combination this distance is 550 pm. It is noteworthy to mention that the A and B type precipitates (containing 3 atom columns components) lie on prismatic planes type I ($\{10\bar{1}0\}$) where type C with even number of atom column components lie on prismatic planes type II ($\{1\bar{2}10\}$).

Furthermore, Fig. 4. 16 (c) and (e) reveal that this phase is elongated along z direction in about 10- 20 nm. The periodic arrangement of the atoms is the same as Mg lattice; hence the lattice parameter in Z direction equals the one for Mg lattice. In addition, this phase can be referred to as plate-like precipitate on prismatic planes. Since this phase is spread in just two directions, it can be referred to as plate-like precipitates.

As was observed earlier in Fig. 4. 16 (a) and (b), this phase does not fully develop a unit cell of D019 and was found only in a short range order. Therefore, considering the size and ordered structure of these precipitates, it is logical to refer to them as G. P. I zones or pre-β" precipitates.

A structural model for the D019 arrangement of Nd atoms in Mg is shown in Fig. 4. 17. A complete unit cell of D019 with same arrangement of atoms results in Mg_3Nd composition. However, the composition of G. P. I zones cannot be determined based on the structure due to lack of defined unit cell.

The arrangement of atoms in this phase is isomorphic with HCP structure; hence precipitation can progress by replacement of Nd atoms with Mg atoms. G. P. I zones has not been reported previously in the Mg-Zn-Nd alloying system.

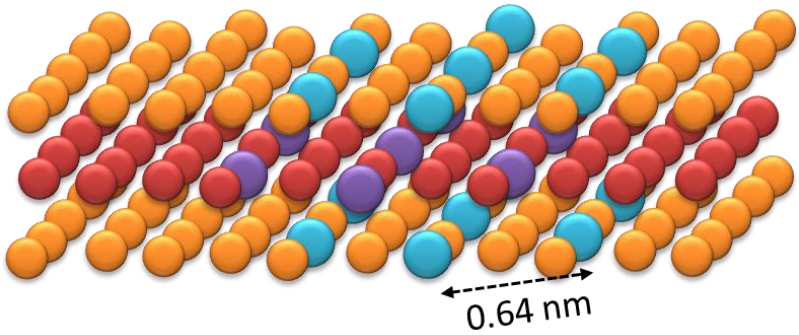

Fig. 4. 17. Atomic model for the G. P. zones obtained from high resolution HAADF-STEM images.

Second type

The FFT image taken from the region containing second type precipitate is shown in Fig. 4. 18. The extra spots from the precipitate show a diffraction pattern for an orthorhombic structure. In

rare earth containing magnesium alloys, base centered orthorhombic (BCO) structure is reported for the metastable β' phase [8, 36, 37, 40, 70-72].

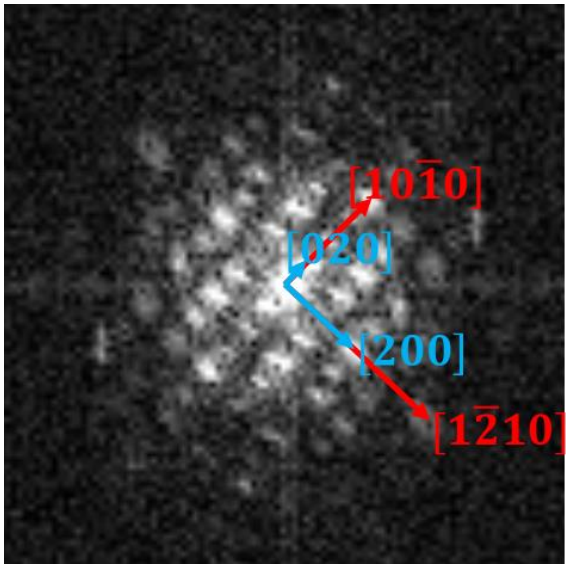

Fig. 4.18. FFT image from the region containing second type precipitate in the sample aged at 200°C for 2hr. The diffraction spots show a typical arrangement for orthorhombic structure.

To better understand the microstructure of this phase, high resolution HAADF-STEM images were obtained from three different zone axes. Images were then modeled to reconstruct the position of solute atoms in the matrix and deduce the structure of this phase. The results are brought in Fig. 4. 19. (a)-(f).

In the image taken with beam parallel to [0001] direction (Fig. 4.19. (a)), an array of zigzag chains is observed that are 1.1 nm apart from each other. The position of atoms inside the chains is similar to 4 atom column components observed in G. P. zones. The zigzag chains are lying on prismatic planes type I ($\{10\bar{1}0\}$) while the precipitate is extended along prismatic planes type II ($\{1\bar{2}10\}$).

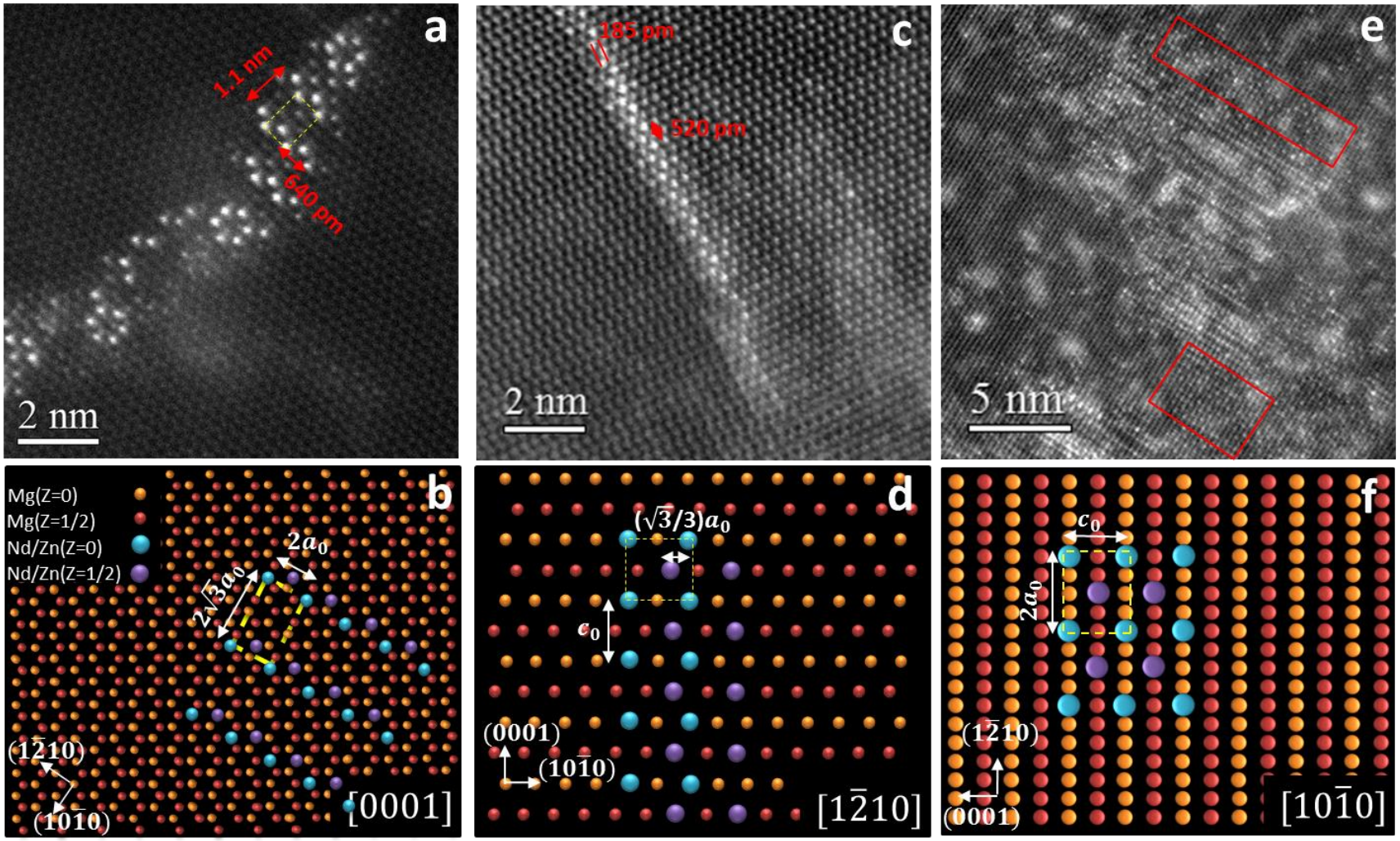

Fig. 4. 19. High resolution HAADF-STEM images and corresponding modeled atomic arrangements for the second type precipitate in the alloy aged at 200°C for 2hr. The beam is parallel to: a) and b) [0001] direction; c) and d) $[1\bar{2}10]$ direction; e) and f) $[10\bar{1}0]$ direction. In the modeled structure, Mg and Nd atoms at different layers are denoted with smaller and bigger circles and different colors.

These precipitates are about 2 nm thick and 4 nm long on basal planes. However, the images taken with beam parallel to prismatic directions show an extension of about 10-20 nm in z direction. Therefore, similar to G. P. zones, these precipitates have a plate-like shape.

The arrangement of chains in the matrix as seen in Fig. 4. 19 (a)-(f) creates an orthorhombic structure. From these images, the structural model for this phase was deduced and presented in Fig. 4. 20. The lattice parameters measured for this type of precipitate are: a_{ppt}= 0.64 nm, b_{ppt}= 1.1 nm, c_{ppt}= 0.52 nm. As was mentioned earlier, the orthorhombic structure is a signature of *β'* precipitates in Mg-RE alloys and therefore the second type precipitate observed in this study is referred to as *β'*.

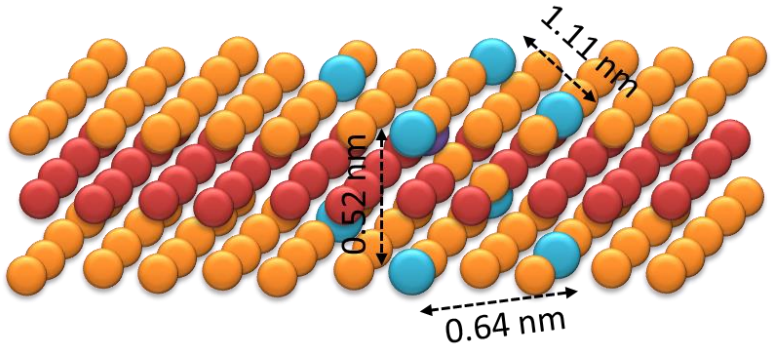

Fig. 4. 20. A 3D model for the *β'* precipitate deduced from high resolution HAADF-STEM images.

Despite TEM studies on Mg-Gd-Y [37] and Mg-Zn-Nd [8] systems which reported a base centered orthorhombic (BCO) structure with $a_{\beta'}$= 0.64 nm, $b_{\beta'}$= 2.23 nm, $c_{\beta'}$= 0.52 nm, our observations showed a simple orthorhombic arrangement of solute atoms in this phase with an extra solute atom at $\{\frac{1}{2},\frac{1}{6},\frac{1}{2}\}$ and a different value for the lattice parameter $b_{\beta'}$. No direct observation of the lattice is reported in any of these systems. However, in the STEM analysis that was performed on Mg-Gd alloy a slightly different arrangement of zigzag chains was observed

which leads to a larger $b_{\beta'}$ lattice parameter (refer to chapter 2, Fig. 2. 5) [38].

From the structure of the *β'* phase, the composition of this phase can be obtained as Mg_7Nd similar to what is reported in literature for *β'* [8]. However, the habit plane observed in this research for this type of precipitate is the common plane reported for *β''* and has not reported for *β'* in Mg-Zn-Nd alloy [7, 8]. The orientation relationship with the matrix can be written as $(10\bar{1}0)_{Mg}//(010)_{\beta 1}$ and $(1\bar{2}10)_{Mg}//(100)_{\beta 1}$.

A closer examination of the microstructure showed that *β'* indeed exists as single unit cells in the matrix. Although it is expected that this phase forms through transformation of the G. P. zones or *β''*, independent formation of *β'* unit cell was observed on prismatic planes $\{1\bar{2}10$ as is apparent in Fig. 4. 21. On the other hand, the size and ordered structure of this components and their uniform presence in the matrix is consistent with formation of G. P. zones. Therefore, to distinguish with *β'* precipitates this phase is designated as G. P. II zones or pre-*β'*.

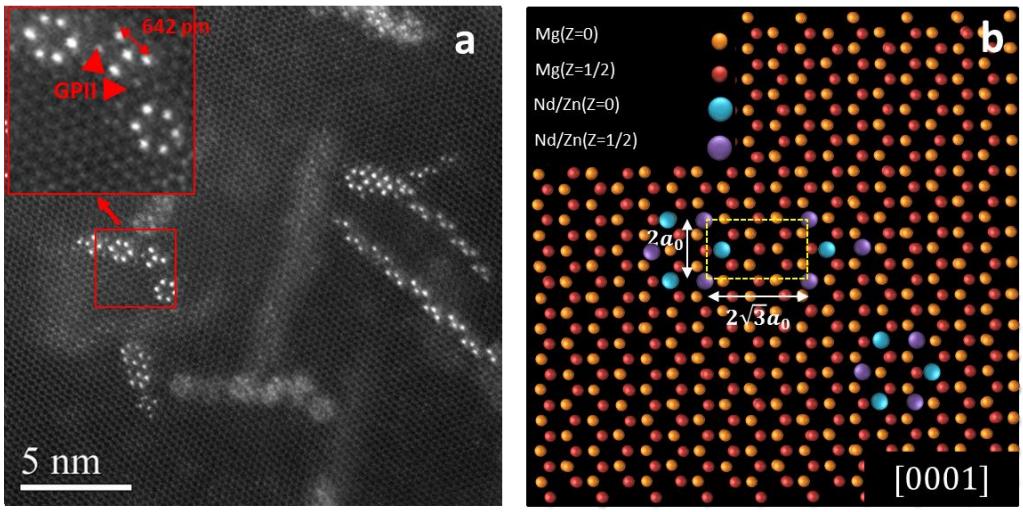

Fig. 4. 21. a) High resolution HAADF-STEM image and b) its model, showing second type G. P. zones detected in the sample aged at 200°C for 2hr. The region containing G. P.II type is magnified in the left image.

The interesting point about this phase is the presence of hexagon arrangement of atoms in the structure. This arrangement is also observed in *β'* precipitates. As seen earlier in Fig. 4. 19. (a), the hexagon arrangement of atoms usually occurs near the end sides of the precipitate (in longitudinal direction). A possible explanation is that the hexagon arrangement of atoms is indeed two opposing 3-atom column components that belong to two variants of *β'* precipitate. This is consistent with the position of atoms in the modeled images in Fig. 4. 19 and 4. 21.

Third type

The third precipitate was detected with a uniform distribution in the matrix. Fig. 4. 21. represents a FFT image taken from the region containing this phase. The orientation and arrangement of spots in the pattern is the same as orthorhombic structure and the one observed for *β'*. However, the spots at ½ $\{10\bar{1}0\}$ are no longer visible.

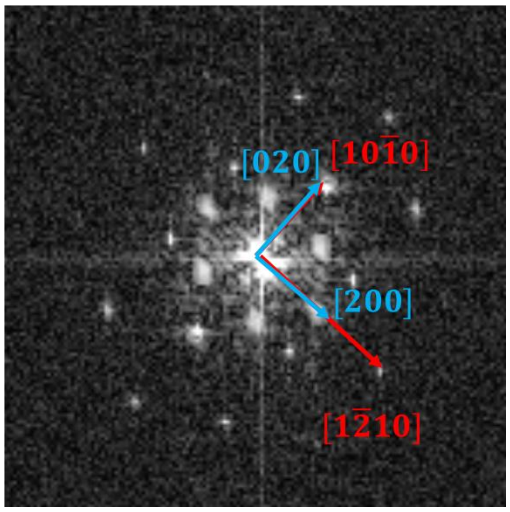

Fig. 4.21. FFT image from the region containing third type precipitate in the sample aged at 200°C for 2hr. The diffraction spots show atomic arrangement for orthorhombic structure.

Fig. 4. 22 (a) and (b) show HAADF-STEM image and the corresponding modeled image of the matrix containing the third type precipitate. According to the images obtained, the size of this phase is measured to be about 5 nm long and 2 nm thick. In addition, the lattice structure of this phase was found to be an orthorhombic structure, similar to β'. The lattice parameters for this phase are measured as a_{ppt}= 0.64 nm, b_{ppt}= 0.56 nm, c_{ppt}= 0.52 nm. Fig. 4. 23 shows a structural model for this phase. It can be seen that the b lattice parameter is half of that for *β'*. In addition, the composition of this phase was calculated based on the structure as Mg_3Nd. This composition is similar to what was reported previously for *β''* and β_1.

This phase has not been reported previously for Mg-RE alloys. Therefore, to distinguish with other phases, the third type was designated as β_2. From STEM images, the orientation relationship of β_2 with the matrix was obtained as $(10\bar{1}0)_{Mg}//(010)_{\beta 2}$ and $(1\bar{2}10)_{Mg}//(100)_{\beta 2}$.

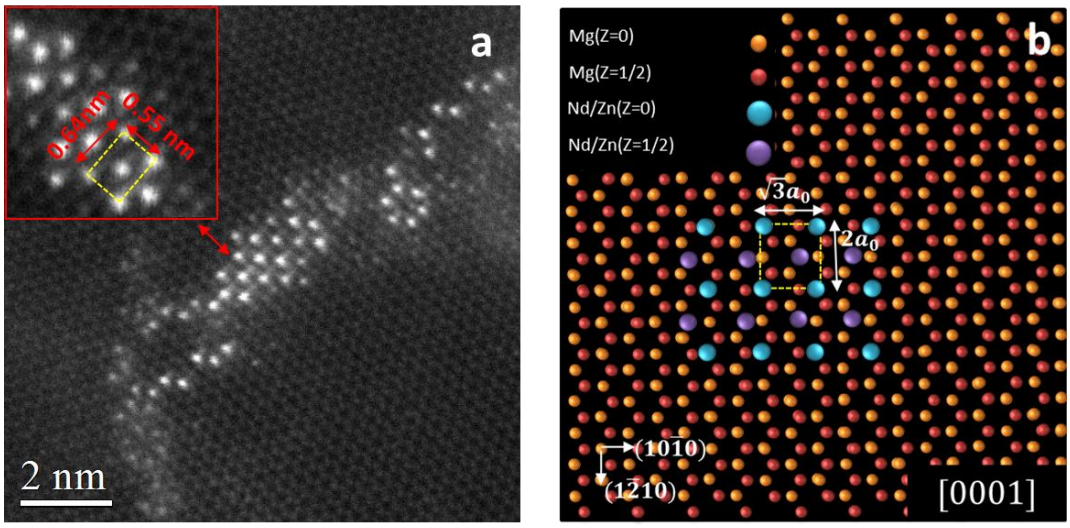

Fig. 4. 22. a) High resolution HAADF-STEM image and b) its model, showing third type precipitate in the sample aged at 200°C for 2hr. The region containing β2 and a unit cell of this phase are magnified and shown in the left image.

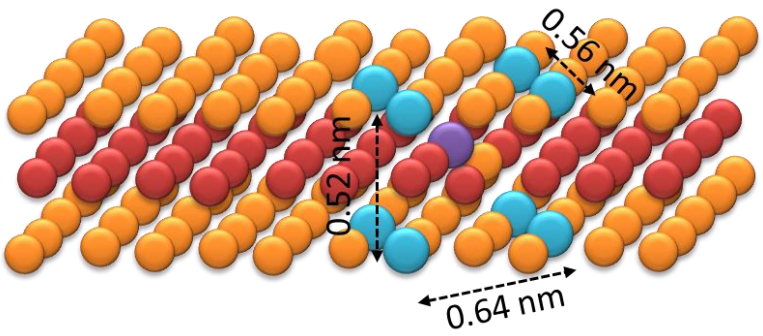

Fig. 4. 23. Structural model for the β_2 phase deduced from high resolution HAADF-STEM images.

Analysis of the microstructure showed that similar to β' phase, β_2 also forms independently as single unit cells in the matrix (See Fig. 4. 24). For this type of precipitate, a combination of hexagon arrangement of atoms (shown with blue arrow) and cross shape (shown with red arrow heads) or all cross shape were detected in the microstructure. The former combination appears in the form of hexagon-cross, and hexagon-cross-cross as indicated by 1 and 2 in Fig. 4 24. (a)-(c), respectively. On the other hand, the latter combination comes in the form of cross pairs, indicated by 3 in Fig. 4. 24 (b) and (c). If the combination contains only one cross shape, the precipitate lie on prismatic planes type II ($\{1\bar{2}10\}$) where in the case of combination with two cross shape, the precipitate form on prismatic planes type I ($\{10\bar{1}0\}$). The interesting point is that in either combination of hexagon-cross-cross or cross-cross, there is a 90° rotation between the crosses which creates the orthorhombic arrangement of atoms. Similar to first type precipitate, the cross shape does not form a complete unit cell, however, it appears as a short range ordered structure in the microstructure. Therefore, to distinguish with the more developed β_2 phase, they were designated as G. P. III zones or pre-β_2.

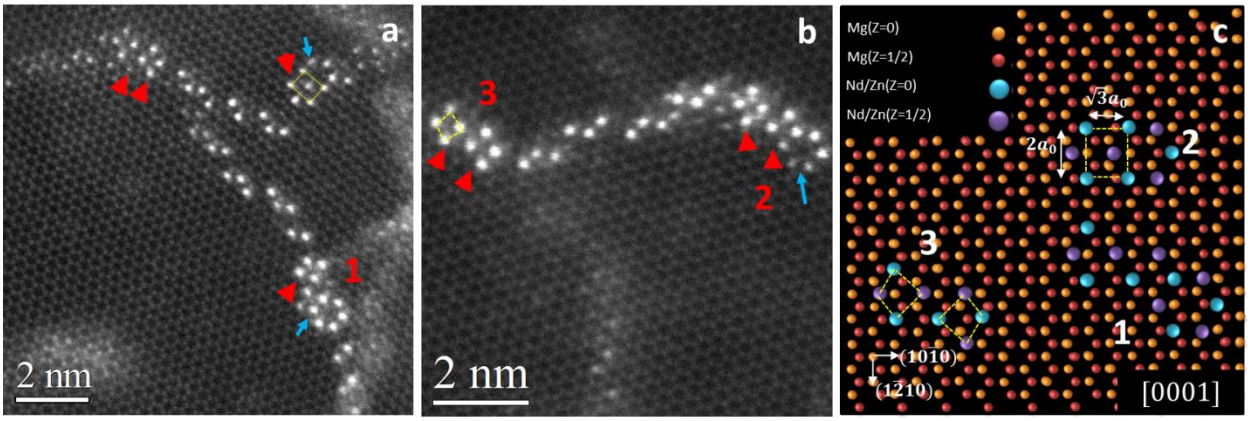

Fig. 4. 24. High resolution HAADF-STEM images and the modeled image showing the presence of G. P. III zones in the microstructure. The beam is parallel to [0001] direction.

Fourth type

The fourth type precipitate was detected sparsely distributed in the matrix. The FFT image (Fig. 4. 25) taken from the region containing this phase showed similar pattern to β_2. However, it appears that the position of atoms in this phase has been shifted with respect to β_2. In addition, as can be noticed, the spots from the precipitate do not fall at the same place as for Mg. Therefore, this phase may not be fully coherent with the matrix in all directions.

Fig. 4. 26 (a)-(f) show high resolution HAADF-STEM images taken from the fourth type phase with beam parallel to basal and prismatic directions. The modeled images are included to better identify the arrangement and position of atoms in the structure. From the STEM images, it is evident that this phase precipitates on both types of prismatic planes at this aging condition.

As seen from Fig. 4. 26. (a) and (b), this phase is coherent along $[10\bar{1}0]$ direction and the distance between atomic planes in this direction is measured as 0.52 nm, close to $2\times d_{10\bar{1}0}$. However, in the $[1\bar{2}10]$ direction at the interface, there is a slight difference between the distance

of atomic planes (0.37 nm for the precipitate atomic planes vs. 0.32 nm for Mg atomic planes).

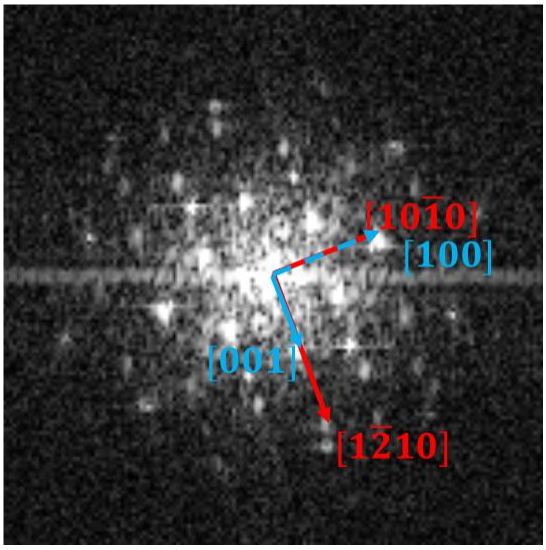

Fig. 4. 25. FFT image from the region containing fourth type precipitate. The sample is aged at 200°C for 2hr. The diffraction spots show similar pattern reported for β1 phase.

Examination of the images taken from three zone axes (i.e. Fig. 4. 26. (a)-(f)) reveals a similar atomic arrangement to β_1 in Mg-RE alloys. The structure of β_1 is reported to be FCC with a=0.74 nm [8, 34]. However, from high resolution HAADF-STEM images and the corresponding modeled images, we constructed the position of solute atoms as well as Mg atoms inside the precipitate. It was found out that the lattice structure of this phase is in fact a body centered tetragonal (BCT) lattice with extra atoms at $\{0,\frac{1}{2},\frac{1}{4}\}$. $\{\frac{1}{2},1,\frac{1}{4}\}$, $\{0,\frac{1}{2},\frac{3}{4}\}$, $\{\frac{1}{2},1,\frac{1}{4}\}$, $\{0,1,\frac{1}{2}$, $\{1,0,\frac{1}{2}\}$, $\{0,0,\frac{1}{2}\}$, $\{1,1,\frac{1}{2}\}$, $\{\frac{1}{2},\frac{1}{2},0\}$ and $\{\frac{1}{2},\frac{1}{2},1\}$ positions. From the modeled images, the lattice parameters were calculated as $a_{\beta1}$= 0.52 nm, $b_{\beta1}$= 0.52 nm, $c_{\beta1}$= 0.74 nm. The structural model for this phase is presented in Fig. 4. 27. The composition of this phase, based on the structure is calculated as Mg_3Nd similar to what previously reported for this phase.

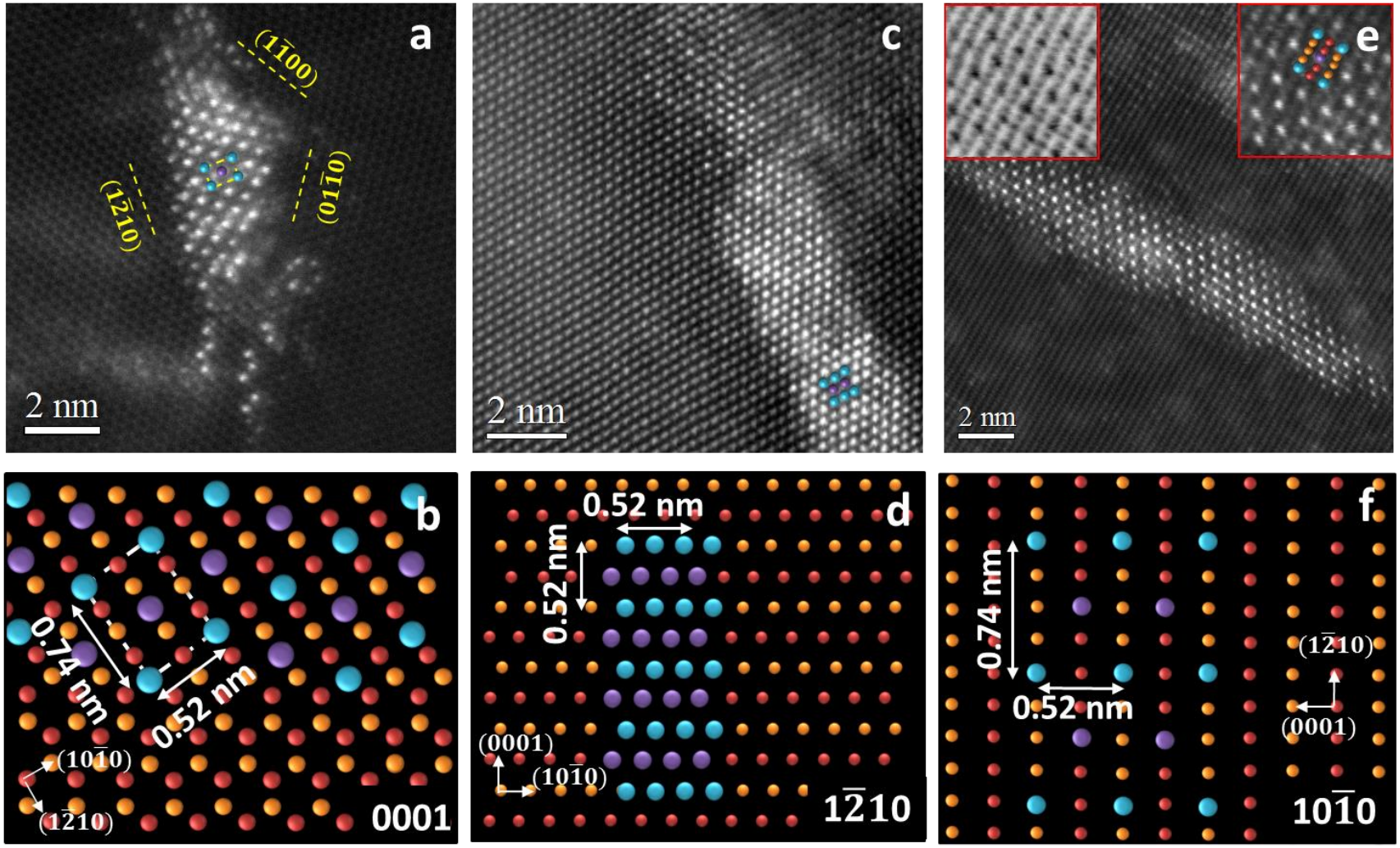

Fig. 4. 26. High resolution HAADF-STEM images and corresponding modeled atomic arrangements for the fourth type precipitate detected in the alloy aged at 200°C for 2hr. The beam is parallel to: a) and b) [0001] direction; c) and d) [1$\bar{2}$10] direction; e) and f) [10$\bar{1}$0] direction. In the modeled structure, Mg and Nd atoms at different layers are denoted with smaller and bigger circles and different colors.

A unit cell of BCT β_1 identified in this study is indicated in the model, as dashed white lines in Fig 4. 23. The previous structure (FCC) for this phase is also presented in yellow lines [34]. One can see that the FCC structure does not represent the smallest repeating unit in this structure. Therefore the fourth type phase in this alloy was identified as β_1 with BCT structure. The orientation relationship of BCT β_1 with the matrix can be written as $(10\bar{1}0)_{Mg}//(100)_{\beta 1}$ and $(1\bar{2}10)_{Mg}//(001)_{\beta 1}$.

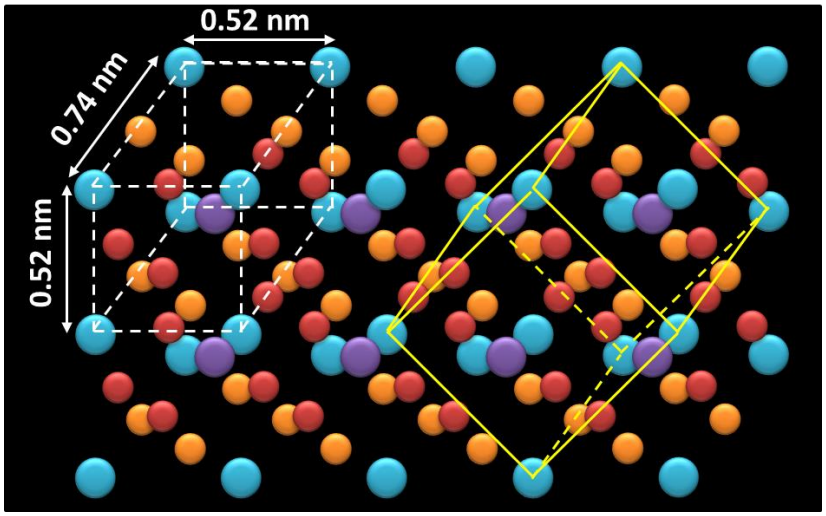

Fig. 4. 27. Structural model for β_1 phase with body centered tetragonal structure. The FCC lattice previously reported for this phase is shown in yellow lines for comparison.

Clustering of atoms

Although no strong evidence of clustering of atoms was found in the TEM micrographs as well as DSC traces of the aged alloys, HAADF-STEM images showed a significant concentration of bright spots in some regions of the matrix. Fig. 4. 28 (a)- (c) shows the presence of these spots in the micrographs taken from three zone axes. These spots usually appeared as a group of brighter atom columns with about 1 nm or less in diameter and a lower contrast than identified phases.

Since the micrographs from different zone axes show the same size and morphology for these spots and also no specific structure or ordering could be found, these features should be in the form of a congregate or clusters of atoms in the microstructure. In addition, we performed atom probe tomography analysis on the sample aged at 200°C for 2hr. Data analysis of clustering showed the a sparse concentration of small clusters of Nd-Zn (less than 1 nm) in the structure which is in agreement with microstructure observations. Despite there is no report on the presence of clusters of atoms in Mg-Nd alloys, the results of our STEM and APT analyses are evident to formation of clusters of solute atoms in this system. In addition, the absence of any clustering evident in DSC traces of naturally aged samples is in agreement with uneven and sparse distribution of clusters in the structure of under-aged sample. This may show that clustering is not the main mechanism in formation of new phases at early stages of precipitation in Mg-Nd-Zn system.

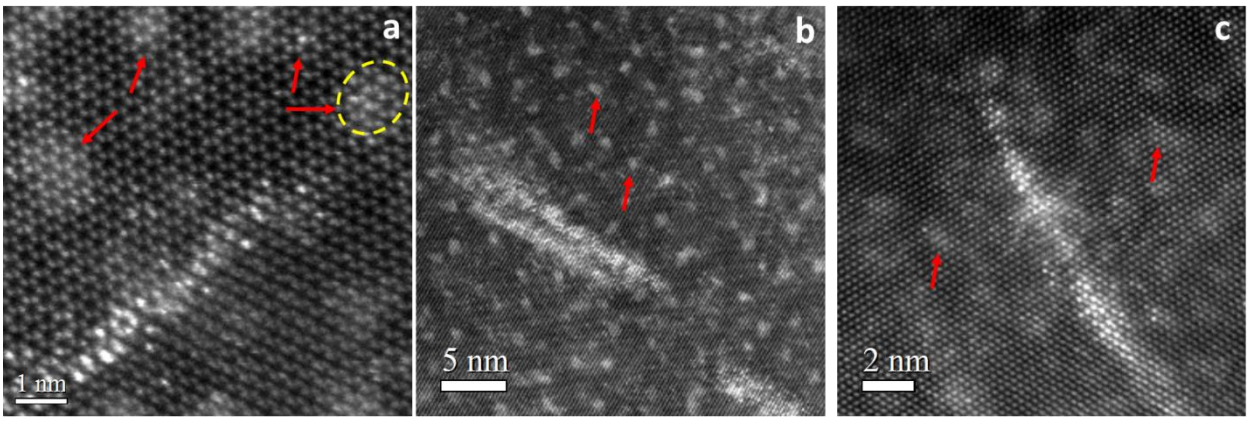

Fig. 4. 28. High resolution HAADF-STEM images showing the presence of clusters of atoms in the 2hr aged sample. The beam is parallel to a) [0001]; b)[$10\bar{1}0$]; and c) [$1\bar{2}10$].

4.5.2. Peak-aged condition

As was seen earlier, the peak-aged condition for the studied system occurs at aging times around 8hr for the aging temperature of 200 C°. The microstructure of the sample at this aging condition was studied by means of STEM to investigate the evolution of precipitation with respect to time. Fig. 4. 29 (a) shows a HAADF-STEM image of a uniform distribution of the precipitates in the matrix.

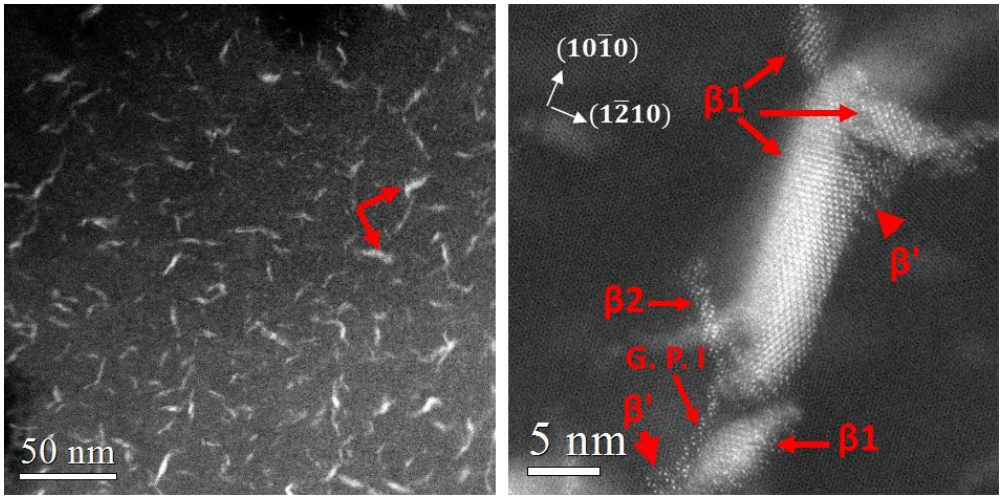

Fig. 4. 29. a) HAADF-STEM image of the 8hr aged sample; b) high resolution image showing the presence of different phases in the microstructure at this aging condition. The beam is parallel to [0001] direction.

In this aging condition, the length of the precipitates in the matrix ranges from 5-30 nm and the thickness of the precipitates varies from 2-10 nm. Our high resolution HAADF-STEM images revealed the presence of all phases that were identified in the 2hr aged sample. (see Fig. 4. 29. (b)). However, for the peak-aged condition, significantly higher number of β_1 phase was detected in the system where as other phases were found less abundant. The size of the β_1 varies from 10-30 nm in length and 5-10 nm in thickness.

Although a uniform distribution of β_1 was detected in the matrix, a sparse presence of large β_1 phase was detected in some grains as is evident in Fig. 4. 30. The size of these precipitates were about 300-400 nm long and 10 nm thick. In addition a large PFZ was detected around this phase with about 200 nm thickness (see Fig. 4. 26). From the size of these precipitates and the presence of PFZ around them, it can be postulated that these precipitates form at early stages of precipitation. Due to inhomogeneity introduced by PFZ, formation of this region has a negative effect on mechanical properties of the alloys.

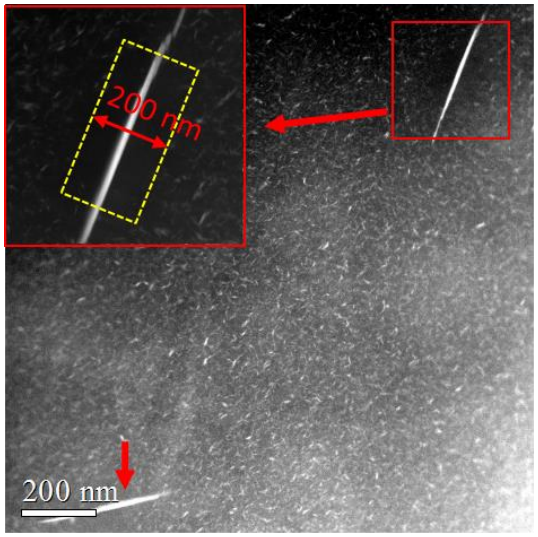

Fig. 4. 30. HAADF-STEM image of the microstructure of the 8hr aged alloy showing the presence of large β1 precipitates and PFZ region around them.

4.5.3. Over-aged condition

The last studied sample was a 64hr aged sample at 200°C. Fig. 4. 31. (a) and (b) show the HAADF-STEM images taken near $[10\bar{1}0]$ and $[1\bar{2}10]$, respectively. Examination of the microstructure revealed that in this condition, β_1 is the main existing precipitate in the

microstructure. In addition to this phase, the presence of the equilibrium β phase was detected at gain boundaries as seen in Fig. 4. 31. (a).

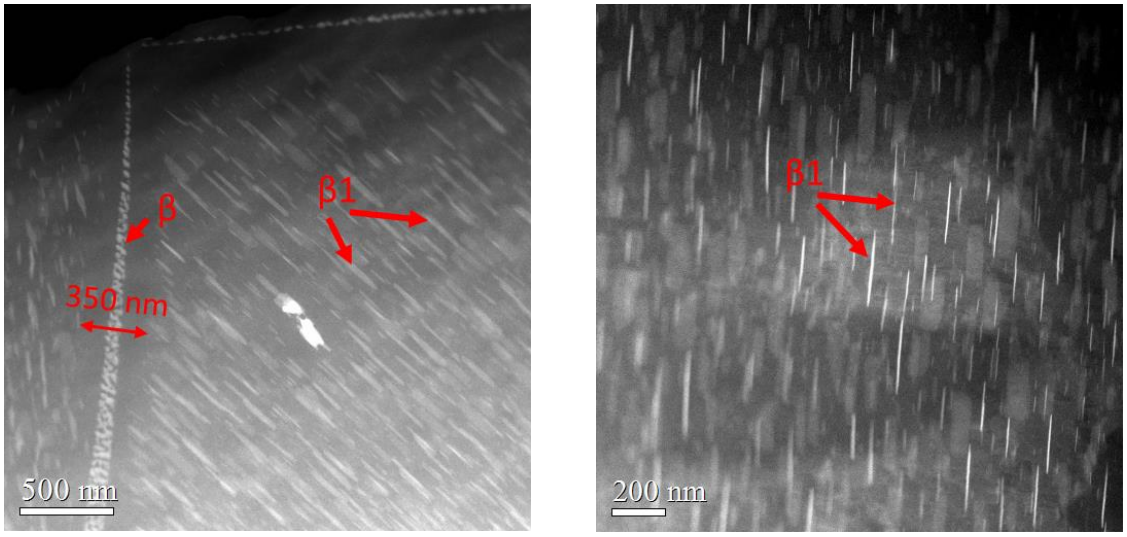

Fig. 4. 31. HAADF-STEM images of the sample aged at 200°C for 64hr (over-aged condition). The beam is parallel to: a) $[10\bar{1}0]$ and b) $[1\bar{2}10]$. The presence of β1 and β was detected at this aging condition.

Our TEM analysis of the β phase on grain boundaries revealed an FCC lattice structure for this phase with a_{β} = 1.11 nm, as calculated from Fig. 4. 32 (b)-(d). The FFT in Fig. 4. 32 (e), which is taken from the 4. 32. (b) image, shows a matrix/precipitate orientation of $(10\bar{1}0)_{Mg}//(\bar{2}00)_{\beta}$ and $(1\bar{2}12)_{Mg}//(020)_{\beta}$.

The possible structural model for this phase with respect to the $Mg_{12}Nd$ composition is shown in Fig. 4. 33. In this model Nd/Zn atoms are placed at {½, ½, ½} positions where Mg atoms fill the FCC positions. In addition, a simple cubic arrangement of Mg atoms inside FCC lattice exist with a lattice parameter half of that for FCC lattice.

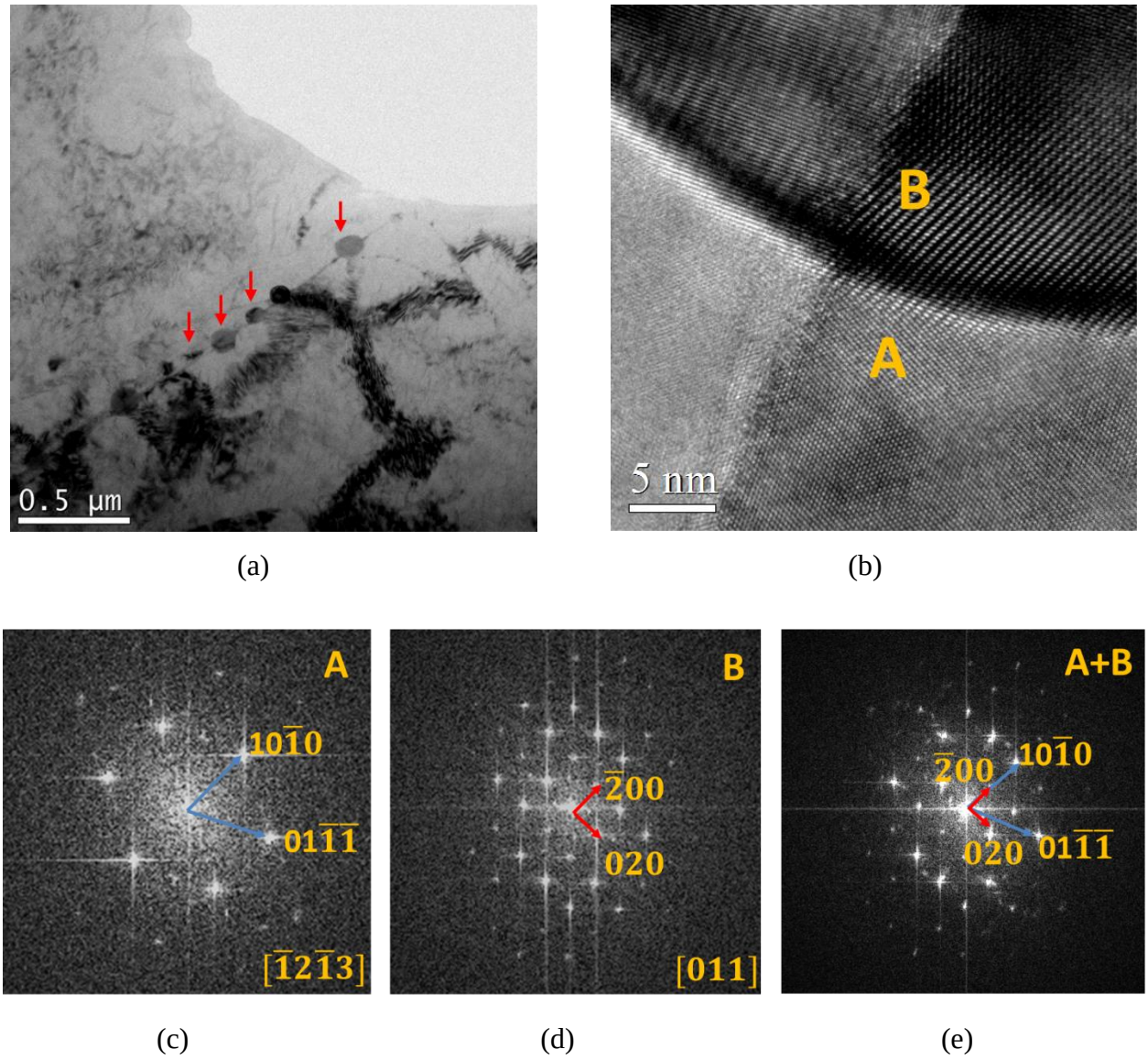

Fig. 4. 32. TEM micrographs of the sample aged 64hr at 200°C. a) BF image showing the β phase on grain boundaries; b) HREM image of the β on grain boundary; c) FFT taken from region A; d) FFT taken from region B; e) FFT of the (b) image.

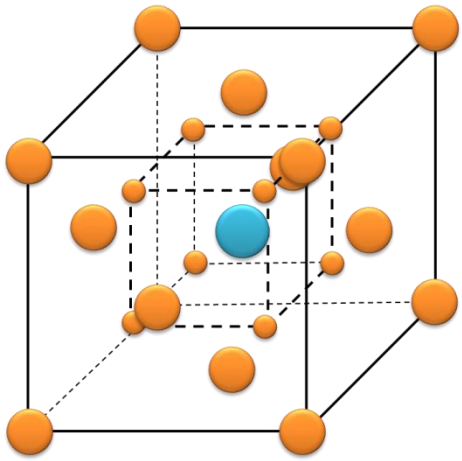

Fig. 4. 33. Structural model for β phase unit cell. The small and large orange circles represent Mg atoms inside a unit cell where the large blue circle represents Nd atom.

4. 5. 4. Phase formation mechanisms

G. P. I zones formation

As was seen earlier, G. P. I zones are the first ordered structure that form in the matrix during isothermal annealing at 200° C. In addition, G. P. I zones were mainly composed of 3 and 4 atom column components. Since this phase is isomorphic with the matrix, G. P. zones grow by simply replacement of solute atoms with Mg atoms in the matrix.

β' formation

As the aging proceeds, G. P. zones transform into the coherent β' phase. β' phase is composed of an array of zigzag chains with 3 atomic planes apart in $<10\bar{1}0>$ direction. According to microstructure analysis, formation and growth of β' can occur through two main mechanisms:

1) G. P. I zones are mainly composed of 3 and 4 atom column components. The arrangement of atoms in the components is similar to the atomic structure in β' chains but with the difference

that in G. P. I zones there is a disconnection between the components. Since these units are isomorphic with the structure, they can shift in the matrix simply by substitution of solute atoms with Mg atoms. As shown in Fig. 4. 34, a successful transition of the 3 or 4 atom column components in $<1\bar{2}10>$ direction and by a distance equal to a_0 (Mg lattice parameter) results in formation of a zigzag chain similar to what was seen for β' structure.

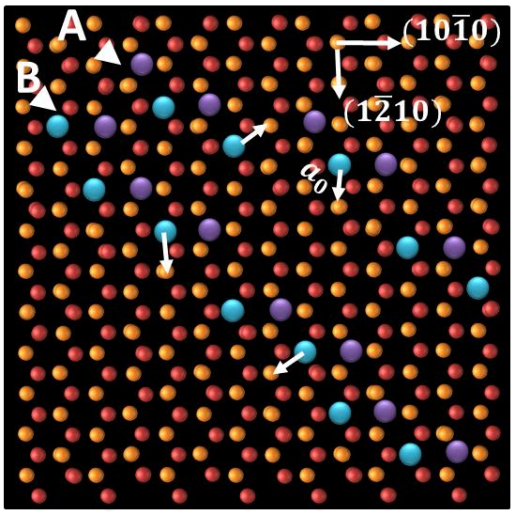

Fig. 4. 34. The schematic diagram showing proposed mechanism for the transformation of G. P. I zones into *β'* at early stages of precipitation.

2) Although the transformation of G. P. I into *β'* may occur through the mechanism explained above, earlier analysis revealed the presence of G.P. II or pre-*β'* phase in the matrix with exact lattice structure. Therefore, growth of G. P. II zones by substitution of solute atoms with Mg atoms can produce a structure of the *β'* phase.

Since the presence of *β"* was not detected in the microstructure, the transformation of G. P. zones I and II into *β'* is most likely the dominant formation mechanism of *β'* phase at early

stages of precipitation.

β_2 formation

It was found out that both *β'* and *β_2* have a BCO structure. However, the lattice parameter b for *β_2* phase is half of that for *β*'. From microstructure observations it was found out that *β_2* formation indeed occurs by addition of a zigzag chain at half distance between the existing chains in the *β*' structure. This mechanism is evident in Fig. 4. 35 (a) and (b). Since the distance between existing chains in *β*' structure is three atomic plane in $<10\bar{1}0>$ direction, the extra atomic chain is formed on the second atomic plane, as shown in Fig. 4. 35 (c). This addition does not change the lattice structure of the phase but leads to a decrease in lattice parameter b to half of that for *β*'. Similar to *β*', *β_2* also forms on prismatic planes type II.

In addition, the formation of *β_2* structure can occur through the growth of G. P. zones III or pre-*β_2* phase detected in the microstructure. Similar to *β*', the growth may continue by replacement of Nd/Zn atoms with Mg atoms in the matrix.

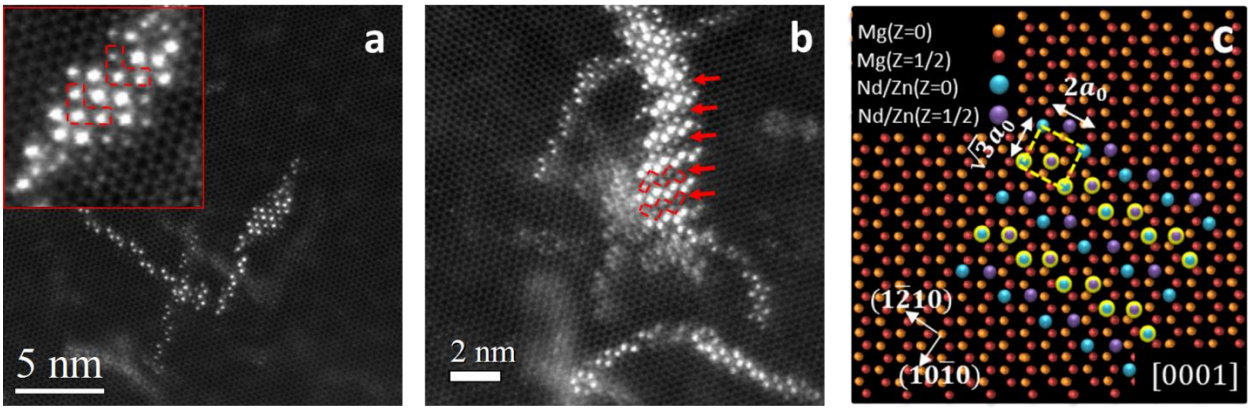

Fig. 4. 35. a) and b) High resolution HAADF-STEM images; c) modeled atomic arrangement showing the transition of β' transition β_2.

β_1 formation

Since the structure of β_2 is different from β_1, the transformation cannot simply occur by substitution or addition of atoms in the matrix. In addition, it was deduced earlier that β_1 is not fully coherent with the matrix. Therefore, a transformation in β_2 phase should occur to create the new lattice structure. Since the composition of the two phases is the same, the number of atoms inside each unit cell remains unchanged. By taking into account the position of the solute atoms and Mg atoms in the first and second layers, a possible mechanism for transformation of β_2 to β_1 can be identified as deformation of β_2 lattice. This is shown in Fig. 4. 36. (a)-(d). As seen from Fig. 4. 36 (b), the transformation occurs by expansion of the β_2 lattice in $[01\bar{1}0]$ direction followed by shearing of the β_2 lattice in $[2\bar{1}\bar{1}0]$ direction. The magnitude of the deformation was calculated from the atomic positions as ε=0.08 and γ=0.18. Considering the position of the atoms, a successful transformation causes the white dashed rectangle in Fig. 4. 36 (b) to transform into a rhombus, drawn in Fig. 4. 36 (d). This transformation creates the β_1 unit cell (shown in yellow lines in Fig. 4. 36 (d)) out of orthorhombic arrangement of atoms in β_2 (Fig. 4.36 (b)). Since the transformation of β_2/β_1 occurs through shearing of the origin phase, this transformation is analogous to martensitic transformation in steel [73] and NiTi alloys [74]. Similar mechanism have been reported in literature for the transformation of β_1 (FCC) from Mg matrix in Mg-Y-Nd [34], γ (Ag_2Al, HCP) in Al-Ag (FCC) alloys [75], θ' (Al_2Cu, tetragonal) in Al-Cu alloys [76].

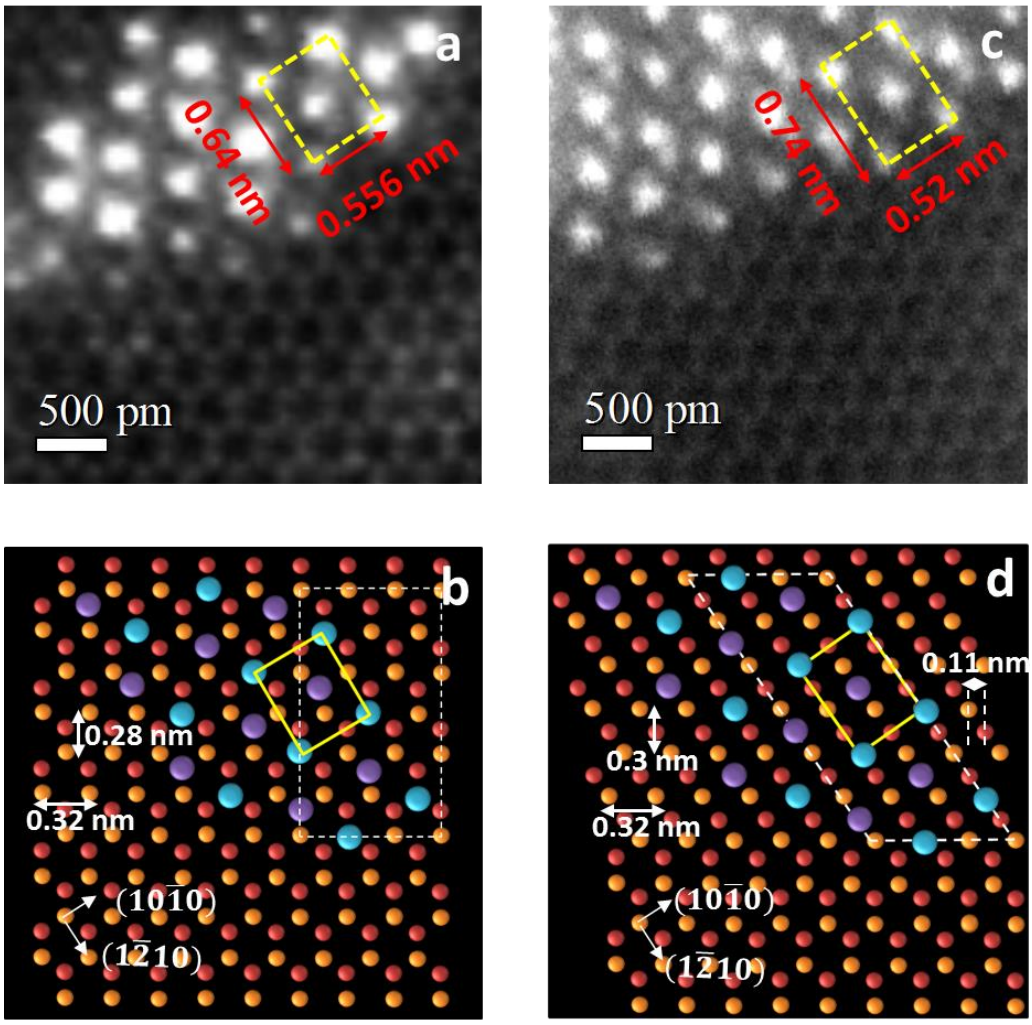

Fig. 4. 36. High resolution HAADF-STEM images showing arrangment of solute atoms in a) β_2 precipitate and b) β_1 precipitate; c) and d) are the modeled images of a) and b), respectively. The models are reconstructed to deduce the structure and position of atoms in layer A and B of magnesium matrix.

In Mg-Y-Nd and Mg-Y-Gd alloys with no Zn, formation of β_1 occurs in a way that β' particles are in contact with the end facets of β_1 rather than the broad surface [34, 36]. Such behavior has been attributed to the tension and compression regions which result from shearing of the matrix (see Fig. 4. 37). Since larger solute atoms tend to occupy the regions with tension strain, β_1 grows from the end facets rather than the broad surface. In contrast, the vacancies tend to occupy the regions with compression strain.

This behavior was not observed for the growth of β_1 in our investigations of the microstructure. Instead β_1 grows on $(10\bar{1}0)$ and in $<1\bar{2}10>$ as plates from its broad surfaces. This difference may be attributed to the effect of Zn on β_1 growth. Upon deformation of the β_2 lattice, a compression and tension regions form as a result of the shear strain. Since the atomic radius of Zn (134 pm) is smaller than Mg (160 pm) and Nd (181 pm), the strain energy associated with the deformation is reduced by migration of Nd atoms into tension regions and migration of Zn atoms into compression region. As a result, the growth of β_1 continues on the broad surface.

In addition, if clusters of Nd-Zn are generated in the system, presence of such clusters near β_1 can promote the growth of β_1 in the matrix by aforementioned mechanism. In fact our APT analysis on formation of clusters showed the presence of Nd-Zn clusters in the 2hr aged sample. Furthermore, as shown later in this chapter, we confirmed the presence of Zn in β_1 phase by APT analysis that was performed on 2hr and pre-deformed 8hr aged samples. The presence of Zn in the structure of β_1 as well as existence of Nd-Zn clusters in the matrix are evidence that make our proposed mechanism more plausible.

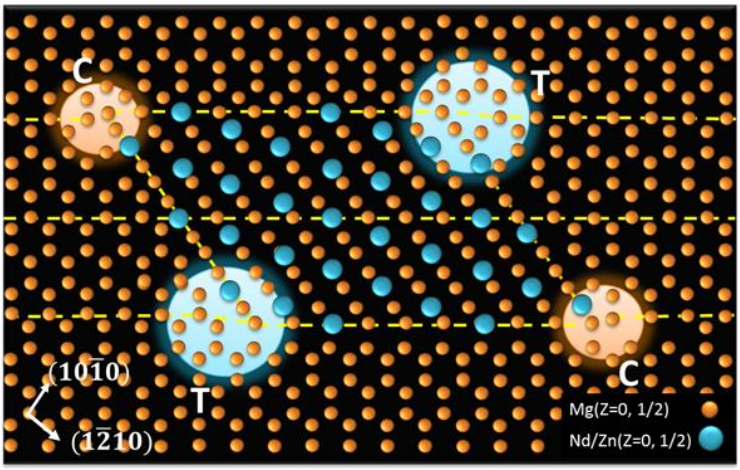

Fig. 4. 37. Schematic model of the structure showing β_1 precipitate in the matrix. The compression and tension regions, resulted from shearing of β_2, are indicated by C and T, respectively.

4. 6. Precipitation kinetics

DSC technique was employed to examine the kinetics of precipitation in the studied alloy. Fig. 4. 38 shows the DSC curves acquired at four different heating rates from as -quenched samples. As can be noticed, the positions of exothermic peaks change with respect to the heating rate; as the heating rate increases, there is a slight shift to higher temperatures.

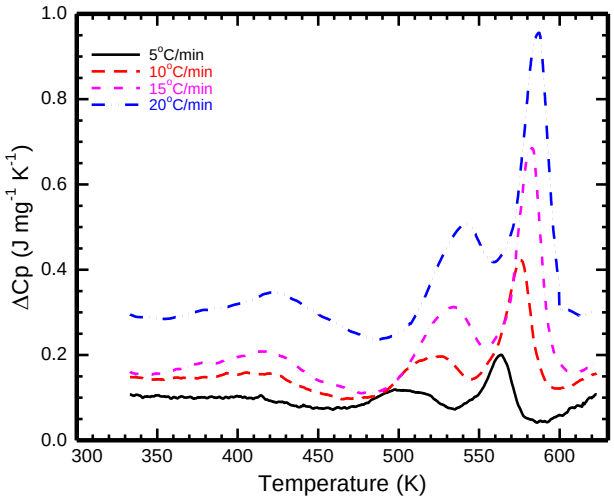

Fig. 4. 38. DSC traces of the as-quenched samples acquired at different heating rates. The peak temperatures were used to calculate the kinetic parameters.

The shift in the peaks is different from one peak to another. This behavior indicates that the reactions are thermally activated and kinetically controlled. Therefore, by using the method described by Woldt [55], the activation parameters were calculated and plotted in Fig. 4. 39 for the precipitation events.

Fig. 4. 39. (a) shows the graph of $\frac{T_i^2}{\phi_i}$ vs. $\frac{1}{T_i}$ for the curves shown in Fig. 4.39. for all exothermic peaks. With the assumption of site-saturation condition, the slope of each curve gives the

activation energy for that reaction. In terms of the second and third peaks related to precipitation of β' and β_2, there is a close overlap of these two peaks which makes it hard to precisely deduce the position of the peaks. However, to a good approximation, these peaks can be considered as one, hence, the calculated kinetic parameters were used for both. Indeed our earlier STEM analysis showed a close number density of these two phases in the microstructure, hence, it can be postulated that the kinetics follow a close trend.

Also the slope of the graph of $\ln\left(-\ln(1-X_0)\right)$ vs. $\ln[\frac{T_i^2}{\phi_i}\exp(-\frac{Q}{nRT})]$ will yield the value of n (Fig. 4. 39 (b)). The final values for activation energies and growth parameters are summarized in Table 4. 1.

The growth activation energy of G. P. zones and β'/ β_2 were obtained as 75 and 77 kJ/mol, respectively. These values are lower than the activation energy value reported for self-diffusion in magnesium (i.e. 134 kJ/mol) and higher than the value reported for vacancy migration in magnesium (i.e. 48 kJ/mol) [7, 9]. Since the studied alloys are all in as-quenched state, an excess concentration of vacancies exist in the microstructure. These vacancies can then assist in the formation of early stage precipitates which leads to lower activation energy values. Therefore, quenched-in vacancies play an important role in the growth of early stage precipitates. The presence of significant number density of G. P. I as well as G. P. II (pre- β'), and G. P III (β_2) zones in the microstructure of under-aged alloy could be an evident to this matter.

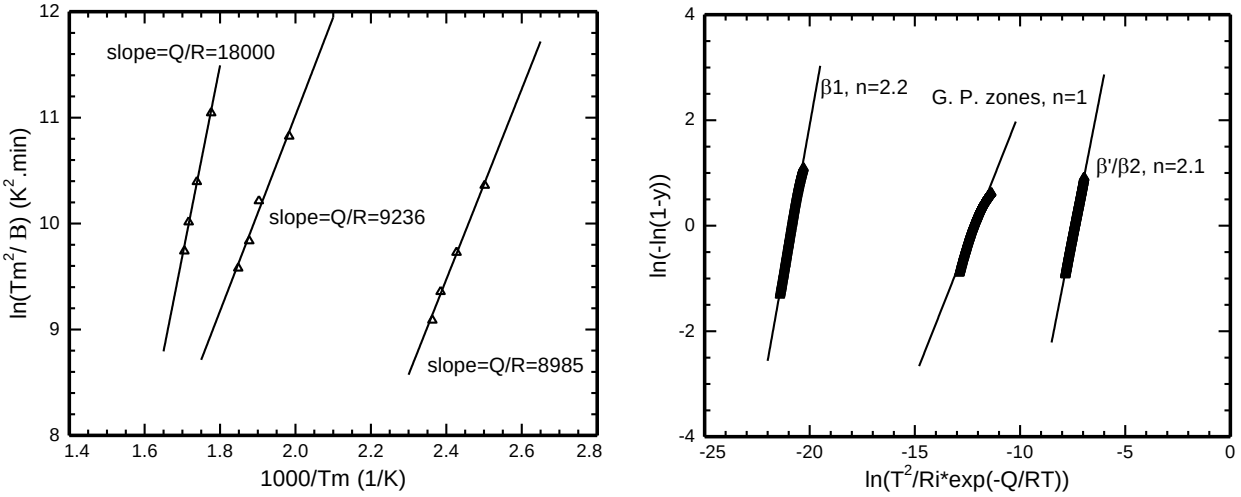

Fig. 4. 39. The activation energies calculated from DSC traces of the as-quenched samples presented in Fig. 4. 38.

In addition, the time exponent of about unity obtained for G. P. I zones is also an indicator of one dimensional growth for this type of reaction. Indeed, the growth of 1-4 atom column components of G. P. zones in Z direction, which produces a rod shape for these precipitates, is in good agreement with the calculated time exponent value. Similar value has been reported for the formation of G. P. zones in Mg-RE system [7].

Table 4. 1. Summary of the calculated activation energies and time exponents for the three types of precipitates

Phase	**G. P. zones**	***β'/ β₂***	***β₁***
Activation energy (Q) (kJ/mol)	75	77	150
Time exponent, n	1	2.1	2.2

In addition, the calculated time exponent for the growth of β'/β_2 (i.e. 2.1) indicates that β'/β_2 grow in two dimensions (i.e. planar growth). This is in agreement with the results of STEM analysis as these precipitates form as plates on prismatic planes.

The activation energy for β_1 was calculated to be 150 kJ/mol. This value is close to the self-diffusion activation energy in magnesium and shows that quenched-in vacancies are no longer effective in this type of precipitation. Instead, the growth proceeds with thermal concentrations of vacancies. Sparse concentration of this phase in the under-aged-sample and the abundance in 8hr aged sample is in good agreement with this matter. In addition, the time exponent value of 2.2 shows a planar growth for this type of precipitation which is consistent with microstructure of the aged alloys.

4. 7. Quantitative analysis of precipitates

Small angle x-ray scattering (SAXS) and TEM are common methods used for quantitative analysis of precipitation in age hardening alloys. Analysis of the XRD patterns (Fig. 4. 40) obtained from as-cast and as-quenched samples showed that peaks related to β ($Mg_{12}Nd$) phase disappear after 5hr solution treatment at 540 °C. However, XRD patterns of different aged samples did not reveal any additional peak from the precipitates. It seems that the precipitates in our system do not have a significant contrast with the matrix that can be resolved. This may be attributed to different effects such as coherency of the precipitates, structure of the precipitates, composition, etc.

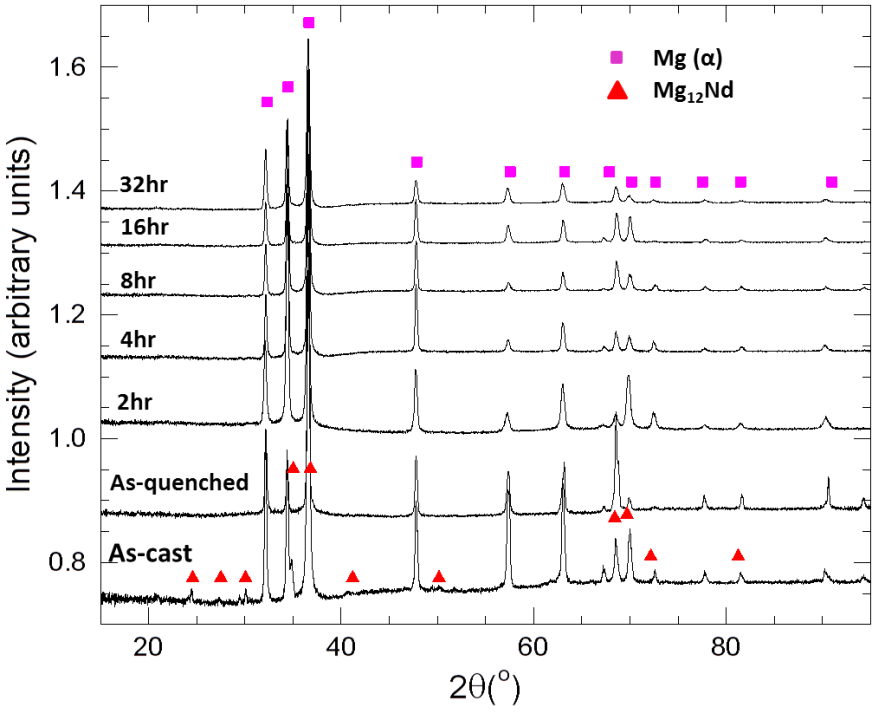

Fig. 4. 40. XRD patterns of the as-cast and heat treated samples. For the aged samples, aging was carried on at 200°C.

The absence of distinguishable peak compared to the as-cast and as-quenched samples shows that x-ray analysis such as SAXS cannot be useful in quantitative investigation of precipitation in this alloy. Therefore in this study, quantitative TEM coupled with DSC technique were used to quantitatively study the aging behavior.

4. 7. 1. Quantitative TEM analysis

Fig. 4.41 shows TEM micrographs taken from alloys aged at 200°C for 2hr (under-aged), 8hr (peak-aged), and 64hr (over-aged). The scale of the images is chosen to be the same for all three aged samples to give a better appreciation of the precipitate evolution. As was seen earlier in our STEM analysis, a combination of all phases exist in under-aged as well as peak aged samples. However, in the peak-aged sample, β_1 was found more abundant. This phase is finely distributed in the matrix. However, for the over-aged condition, only coarse distribution of β_1 was observed.

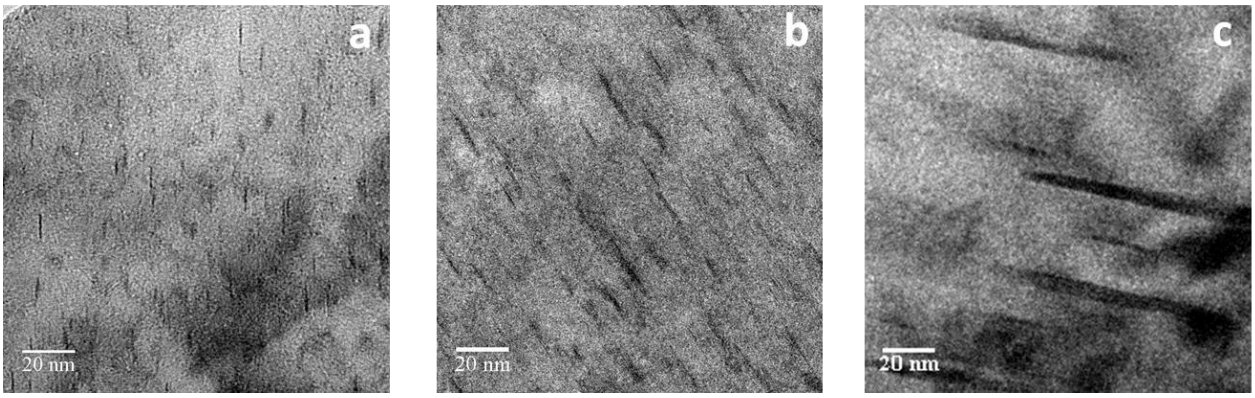

Fig. 4. 41. HRTEM micrographs of samples aged at 200°C for: (a) 2hr, (b) 8hr, and (c) 64hr. The beam is close to $[1\bar{2}10]$.

Quantitative measurements were carried out by counting the number of precipitates, and measuring the dimensions (i.e. the diameter and the width) of counted precipitates. For each

sample, at least three images were analyzed with approximately 80 counts on each image. In the measurements, it is approximated that the precipitate distribution is uniform through the volume; hence, the number of precipitates for each field of observation was calculated as three times of the number of cross sections counted. The number density of the precipitates was calculated by dividing the number of counts by the volume (image size times the thickness) of the region (counts/m^3). In addition, the volume fraction was obtained for each analyzed image using:

$$V_f = N \times V_p, \quad (1)$$

where N is the number density of precipitates (counts/m^3), and V_p is the mean precipitate volume (m^3). The mean volume of a precipitate was calculated by measuring the mean radius, and mean thickness of precipitates at each aging time. The mean radius and mean thickness are the average values of the radius and thickness of the precipitates measured from TEM micrographs.

The results of quantitative TEM analysis are summarized in Table 4. 2. It was observed that the dimensions of the precipitates increase with time while the number density decreases. However, the overall volume fraction almost plateaus after 8hr which is consistent with hardness measurements (see Fig. 4. 4) and implies the over-aged condition after 8hr. In addition, the decrease in number density of the precipitates is consistent with Ostwald ripening mechanism [77] which can be written as (in diffusion controlled mode):

$$R^3 - R_0^3 = \frac{8\gamma c_\infty v^2 D}{9 R_g T} t \quad (2)$$

In this equation R is the average radius of all particles at time t, R_0 is the average radius of all particles at the beginning of aging, γ is the interface energy of the particle, c_∞ is solubility of the particle material, v is molar volume of the particle material, D is the diffusion coefficient of the

particle material, R_g is the gas constant, T is the absolute temperature, and t is the time duration. It should be noted that due to small size of the precipitates compared to the thickness of the sample at early stages of precipitation, detection of all precipitates is not feasible which introduces some error in the measurements.

Table 4. 2. The quantitative TEM analysis of the Mg-3Nd-0.2 alloy aged at 200°C for different length of time.

sample	Average dimension of precipitates (nm)		Number density (nm^{-3})× 10^{-6}	Volume fraction (%)
	Diameter	**Width**		
2 hr	7.9	0.8	173	0.8
8 hr	20.9	2.3	44.5	4.7
64 hr	48.4	4.2	4.5	4.3

4.7.2. Quantitative DSC analysis

Volume fraction measurements

The DSC traces shown in Fig. 4. 10 for the samples aged at 200°C were used for quantitative measurements. In DSC traces, the area under (or above) each peak is indictor of the amount of heat released (or absorbed) during the reaction (i.e. the enthalpy of the reaction) and can be obtained by the following integral:

$$\Delta H = \int_{T_1}^{T_2} (\frac{\delta q}{dT}) dT \qquad (3)$$

For aged samples, the area under endothermic peak varies with respect to the aging time. The reason is that for each aged sample, a fraction of the reaction is completed at that aging time.

Consequently, the amount of heat exchange during DSC heating is a measure of the incomplete portion of the reaction.

Looking at DSC traces of aged samples, an overlap exists between the precipitation/dissolution peaks related to β', β_2 and β_1. However, deconvolution of these peaks is not feasible since it will introduce significant error in the measurements. Esmaeili et al proposed a method to calculate the evolution of volume fraction without any peak separation [78, 79]. In this method, the area of the curve selected for calculating the volume fraction covers the reactions (peaks) that contribute to the volume fraction. Although this method has been used for different aluminum alloys, we will investigate the applicability of this method to magnesium alloys.

With the assumption that the formation of clusters of atoms or G. P. zones does not happen during heating in DSC (completed during aging at 200°C), the area chosen for volume fraction measurements is from 200-325°C which covers the first dissolution peak and the precipitation peaks associated with β', β_2, and β_1. In addition, ΔC_p was chosen to be zero at 50°C for all DSC traces. Also it is assumed that the final state of the microstructure will be the same at the end of DSC cycle regardless of previous thermal history. With the assumptions above, the volume fraction of the precipitates can be calculated as follow:

$$v_f = \frac{|A_{ssss}| - |A_t|}{|A_{ssss}| - |A_{Peak-aged}|} \quad (4)$$

where $A_{Peak-aged}$ is the area under the curve at peak aging (i.e. 8hr), A_t is the area under the curve at t aging time, and A_{ssss} is the area under the curve at solid solution state. In equation 4, we assume that in the solid solution state (as-quenched), the reaction has not started and at 8hr aging time, the reaction for achieving peak hardness is complete (100%). Therefore, the

difference in the heat evolution of as-quenched and 8hr aged samples can be considered as the total heat evolved in completion of the reaction. The volume fraction of the precipitates after *t* time is then calculated as the ratio of the total heat evolved after *t* aging time (numerator in equation 4) to the total heat evolved upon completion of the reaction (denominator in equation 4).

Fig. 4.42 shows the variations in relative volume fraction of the precipitates as a function of temperature calculated from DSC traces. The sigmoidal shape of the curve is consistent with the three stages of nucleation and growth (i.e. incubation time, nucleation and growth, and coarsening) [63]. The calculated values are in good agreement with the values measured by quantitative TEM except for the 2 hr aging time. The large difference between DSC and TEM values for the 2 hr aged sample can be attributed to the contribution of either clusters of atoms or unresolved precipitates in the dissolution peak at early stages of precipitation. The smaller size of the precipitates compared to the thickness of the sample can also prevent the resolution of these precipitates by TEM. The difference between the DSC and TEM values can be used to roughly estimate the concentration of early stage precipitates (i.e. clusters of atoms or unresolved G. P. zones) at 2hr aging. These precipitates are formed during isothermal aging at 200°C or partially during initial heating in DSC (i.e. during first peak in DSC trace). The difference becomes less pronounced as the precipitates become large enough to be resolved by the instrument. It should be noted that the DSC results presented in Fig. 4. 42 are relative values for the volume fraction of the precipitates. However, since the conditions of the samples for DSC and TEM are the same, it is possible to calibrate the DSC data and extract the actual values of the volume fractions by using the values from TEM measurements (see Table 4. 2.).

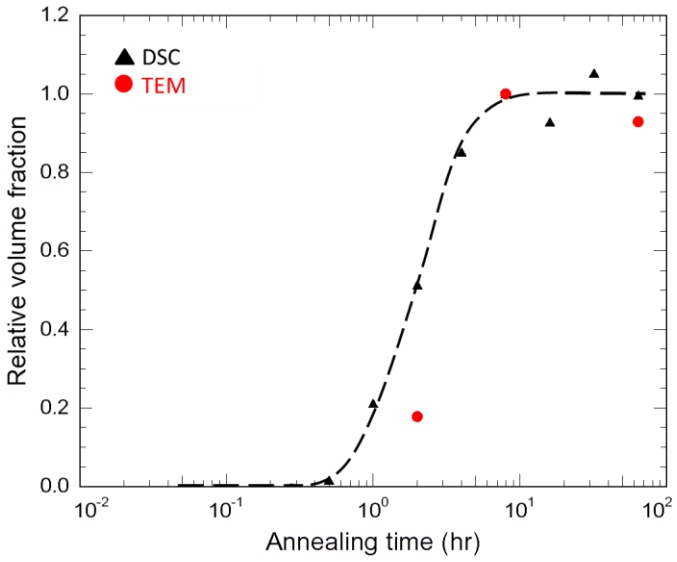

Fig. 4. 42. Relative volume fraction of precipitates as a function of time for the samples aged at 200 °C. The TEM measurements of selected aged samples are shown in the graph for comparison.

Precipitate size measurements

The evolution of precipitate size was studied by careful evaluation of the peak shift in DSC traces of aged samples. As the aging proceeds to longer times, a peak shift toward higher temperatures can be observed in DSC traces (see. Fig. 4. 4). The shift of the dissolution peak to higher temperature at constant heating rate is associated with the increase in the size of the precipitates which is consistent with Gibbs-Thompson model and indicates that larger precipitates are more stable (e.g. dissolution at higher temperature) in the matrix. The higher stability of larger precipitates can be attributed to lower Gibbs free energy of the system resulting from the smaller surface to volume ratio [63].

To find a relationship between the peak shift and the precipitate size, a numerical model was developed which takes into account the increase in half thickness for planar precipitates. According to Whelan [80], the relationship between the concentration profile and flux of the

solute atoms at the interface of dissolving precipitate, and under diffusion controlled process, for instantaneous radius *r* can be written as:

$$\frac{dr}{dt} = -\frac{kD}{2r} - \frac{k}{2}\sqrt{\frac{D}{\pi t}} \quad (5)$$

Where *D* is the volume diffusion coefficient in the matrix; $k = \frac{2(c_i - c_M)}{(c_p - c_i)}$, c_i is the concentration of the solute in the matrix at the precipitate-matrix interface, c_M is the solute concentration in the matrix and c_p is the composition of the precipitate. For a specific case of planar interface (where r~∞) the term *1/r* in equation (6) is negligible [80, 81]; hence, eqn. (5) integrates under isothermal conditions to:

$$r = r_0 - \frac{k}{\sqrt{\pi}}\sqrt{Dt} \quad (6)$$

where *r* is the half thickness of the dissolving precipitate at time *t*, and r_0 is the half thickness at *t*=0. For a planar precipitate, if the aspect ratio (i.e. the ratio of the diameter to the thickness) remains constant, the general relation between the dissolved fraction of the precipitates *y(T)* and volume fraction V_f of the precipitates at a given temperature can be written as:

$$y(T) = 1 - V_f = 1 - (\frac{r}{r_0})^3 \quad (7)$$

Here we assume that the number density of the precipitates remains constant during dissolution and the volume fraction of the precipitates decreases only by shrinkage of the precipitates (decrease in radius). Substituting equation (7) into equation (6) yields:

$$y(T) = 1 - (1 - \sqrt{\frac{k^2 Dt}{\pi r_0^2}})^3 \quad (8)$$

Equation (8) is applicable to isothermal condition. However, under non-isothermal condition and for a heating rate of $\alpha = \frac{dT}{dt}$, equation (8) can be modified to:

$$dy(T) = 1 - (1 - \sqrt{\frac{KdT}{\alpha r_0^2}})^3 \quad (9)$$

Where $K = \frac{k^2 D}{\pi}$. On the assumption that *K* follows an Arrhenius behavior ($K = K_0 \exp(-\frac{Q}{RT})$) equation (9) reduces to:

$$dy(T) = 1 - (1 - \sqrt{\frac{K_0 \exp(-\frac{Q}{RT})dT}{\alpha r_0^2}})^3 \quad (10)$$

Where K_0 is a constant and *Q* is the activation energy. By replacing $\theta = \frac{Q}{RT}$ **,** and integrating both sides of equation (10), the following relationship is obtained:

$$\int_{y_0}^{y_T} dy(T) = 1 - (1 - \int_{\theta_f}^{\infty} \sqrt{\frac{-K_0 \exp(-\theta)}{\alpha r_0^2 \theta^2} d\theta})^3 \quad (11)$$

Where $\theta_f = \frac{Q}{RT_f}$. Under the assumption that $\theta_f \gg 1$, the integral $p(\theta) = \int_{\theta}^{\infty} \frac{exp(-\theta)}{\theta^2} d\theta$ can be solved as [64]:

$$p(\theta) \approx \frac{exp(-\theta)}{\theta^2} \quad (12)$$

Therefore equation (12) can be written as:

$$y(T) = 1 - (1 - \sqrt{\frac{-K_0 \exp(-\theta)}{\alpha r_0^2 \theta^2}})^3 \quad (13)$$

To apply this model, the experimental curves for *y(T)* vs. *T* which have a sigmoidal shape should

be calculated. The fraction of the dissolved precipitates *y(T)* can be obtained from the dissolution peak using expression below:

$$y(t) = \frac{A(T)}{A_f} \quad (14)$$

Where *A(T)* is the area under the peak at temperature *T* and A_f is the total area under the peak. However, in the case of systems with a sequence of precipitation events where there is an overlap of two consecutive peaks (i.e. the dissolution peak and the β_1 precipitation peak), it is not possible to distinguish the end point of the dissolution peak. Therefore, the area under the peak cannot be defined precisely. To resolve this issue, equation (13) was numerically differentiated to yield the plot of ΔC_p as a function of temperature as below:

$$\Delta Cp = \delta \frac{dy(T)}{dT} \quad (15)$$

Where δ is a constant related to the heat content. The calculated dissolution peak from equation (15) was then fitted to the experimental peak by using the precipitate thickness (r_0) and kinetic parameter (K_0) as the fitting parameters. The activation energy *Q* was previously calculated to be 77 kJ/mol for the studied alloy aged at 200°C [13] and is in good agreement with the migration energy of magnesium-vacancy complexes (i.e. 0.59 eV-0.71 eV) [82, 83]. To reduce the number of fitting parameters, the thicknesses of the precipitates measured from TEM micrographs at 2, 8, and 64 hr (see table 4. 2.) were inserted into equation (13). The values for K_0 were then obtained by fitting the calculated peak into experimental one. The average of the values was then chosen for K_0 (2.43×10^{-5} m^2/s) parameter and inserted into equation (13). This resulted in reducing the fitting parameters to one parameter. The mean size of the precipitates for all aging times were found by fitting the calculated peaks from equation (15) into the experimental peaks as shown in

Fig. 4. 43, using r_0 as the fitting parameter. The results are shown as a plot of the mean thickness of the precipitates vs. aging time in Fig. 4. 44. The measured thickness values from TEM micrographs are also shown in the plot for comparison.

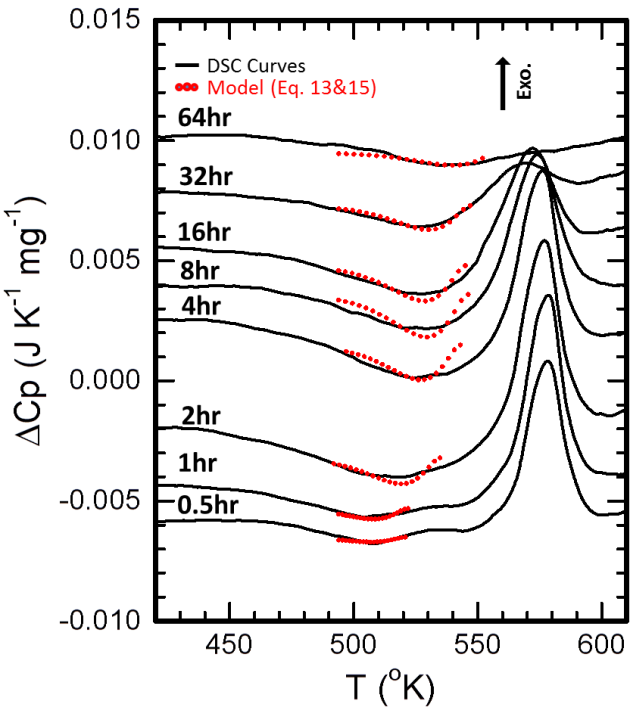

Fig. 4. 43. DSC traces of 8 aged samples at 200 °C. The modeled dissolution peak (using equation 15) is fitted into experimental peak to find the mean thickness values for precipitates. The heating rate for all the tests was 10°C/min.

The DSC values are in good agreement with TEM measurements and follow the same trend. For aging times higher than 8hr, the thickness *h (=2r)* variations with respect to aging time follows a power law relationship. The relationship for this regime can be written as:

$$log(h) = 0.26\, log(t) + 0.09 \qquad (16)$$

The power law exponent value (0.26) obtained from this regime is comparable to the one in equation (2) for Ostwald ripening (0.33) in a diffusion controlled process. Therefore, it can be

postulated that the growth of the precipitates is controlled by Ostwald ripening mechanism in aging times longer than 8hr. The earlier trend obtained for volume fraction of the precipitates as well as TEM measurements are consistent with this finding. It should be mentioned that the measured thickness values in Fig. 4. 44 are representative of the average thickness of the precipitates at each aging time.

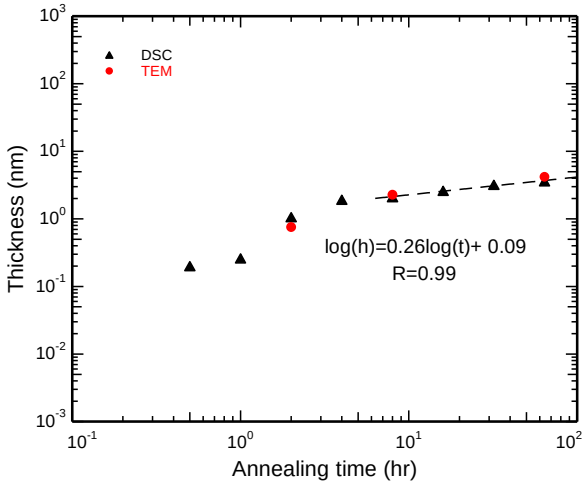

Fig. 4. 44. The thickness of β" precipitates as a function of time obtained from DSC traces for 8 samples aged at 200°C. The values from TEM measurements are brought for comparison.

Aspect ratio

In the case of planar precipitates with thickness h and radius r_p, the volume of a precipitate can be calculated as:

$$V_p = \pi r_p^2 h \qquad (17)$$

Since Equation (13) is able to compute the thickness of the precipitates, it is possible to determine the changes in radius of the precipitates if the aspect ratio (e.g. $a = \frac{Diameter}{thickness}$) follows

a constant trend. For the studied alloy, the aspect ratio of the precipitates was calculated from three samples analyzed by TEM and the results are shown in Fig. 4. 45. The measured values for the aspect ratio are in the range of values reported for disc-shape precipitates (e. g. $\frac{1}{a} < 0.25$) and are consistent with previous analysis on the shape of these precipitates [77]. In addition, to a good approximation, the aspect ratio of the precipitates remains constant ($a = 10$) after 2 hr for the entire range of studied aging time. Therefore, the mean radius and volume of the precipitates can be calculated.

Quantitative TEM was not feasible on samples aged less than 2 hr due to the small size of the precipitates and instrument capability. However, with regard to the obtained aspect ratio values, it can be postulated that any changes in aspect ratio of precipitate toward its equilibrium value (i.e. the equilibrium shape) takes place during the first 2 hr of heat treatment at 200°C. As mentioned in literature [84], the equilibrium or near-equilibrium shape of a precipitate is determined by the interplay between interfacial energy and elastic strain energy from thermodynamic point of view. For early stages of precipitation where the precipitate size is comparable to nuclei critical size, the elastic energy has a negligible effect compared to interfacial energy term and therefore the main factor controlling the shape change will be the interfacial energy. The interfacial energy driven shape change toward its equilibrium state has been also shown experimentally and in simulation of the precipitate growth for other systems [85-87].

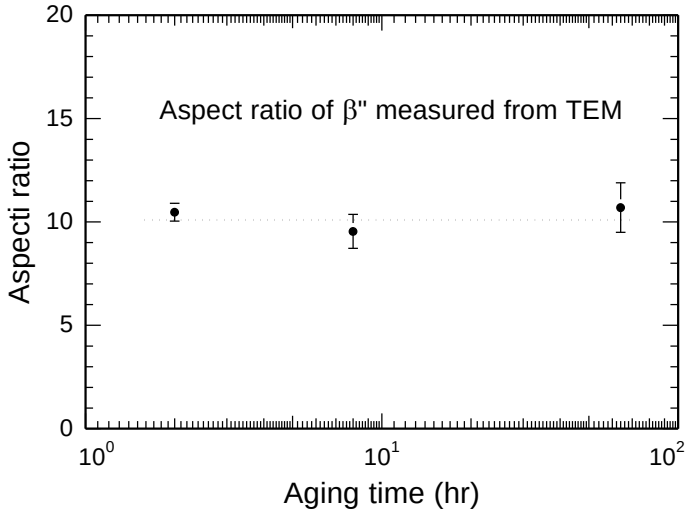

Fig. 4. 45. Aspect ratio (diameter/thickness) as a function of aging time, measured from TEM results for the samples aged at 200°C. The aspect ratio remains at around 10 for the entire aging time.

Furthermore, such a high rate of shape change during the first 2hr shows a faster growth mechanism operating than transfer of solute atoms from smaller precipitates to bigger ones. This is consistent with what was deduced from kinetics study; as quenched-in vacancies play an important role on growth rate of early stage precipitates.

Number density measurements

By inserting the measured aspect ratio value into expression (17), and substituting that expression into equation (1), the number density of precipitates can be calculated as:

$$N = \frac{0.04 V_f}{\pi h^3} \qquad (18)$$

The evolution of number density of the precipitates was obtained using the values in Fig. 4. 42. and 4. 44. for the volume fraction and thickness of the precipitates at each aging time. The results are shown in Fig. 4. 46. as a plot of number density of precipitates vs. aging time. The measured

values from TEM are also brought for comparison. The relationship between *N* and *t* for aging times longer than 8hr was obtained as a power law equation:

$$N=10^{-3.53}\times t^{-0.77} \quad (19)$$

The calculated values from DSC curves are consistent with TEM measurements. In addition, the rate of growth decreases as the aging proceeds to longer times and becomes constant at around 8hr which is indicator of the Ostwald ripening regime.

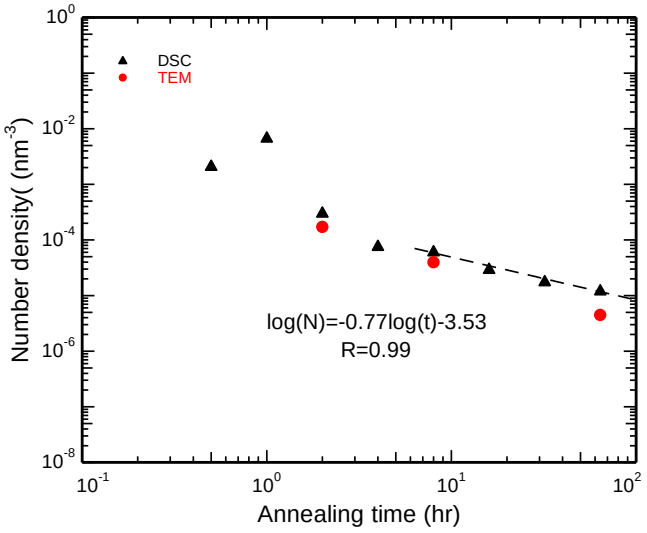

Fig. 4. 46. The variation in number density of precipitates as a function of aging time for the alloy aged at 200°C. The variation follows a power law trend for samples aged longer than 8hr.

4. 8. Effect of deformation on precipitation

4. 8. 1. Mechanical properties and microstructure analysis

The effect of deformation on age hardening was studied on the Mg- 0.2 wt. %Zn-3 wt. % Nd. Three cylindrical samples with same dimensions underwent a compression test at room temperature. The first sample (A), in as quenched state, was loaded to a compression strain of 2%, unloaded, and immediately reloaded to a total strain of 4%. The second as-quenched sample (B) was aged at 200°C for 1hr and then underwent the same loading steps. However, the third as quenched sample was first loaded to 2% compression strain and immediately aged at 200°C for 1hr. This sample (C) was then reloaded to 2% compression strain (total of 4%). The results are presented as true stress-strain curves in Fig. 4. 47.

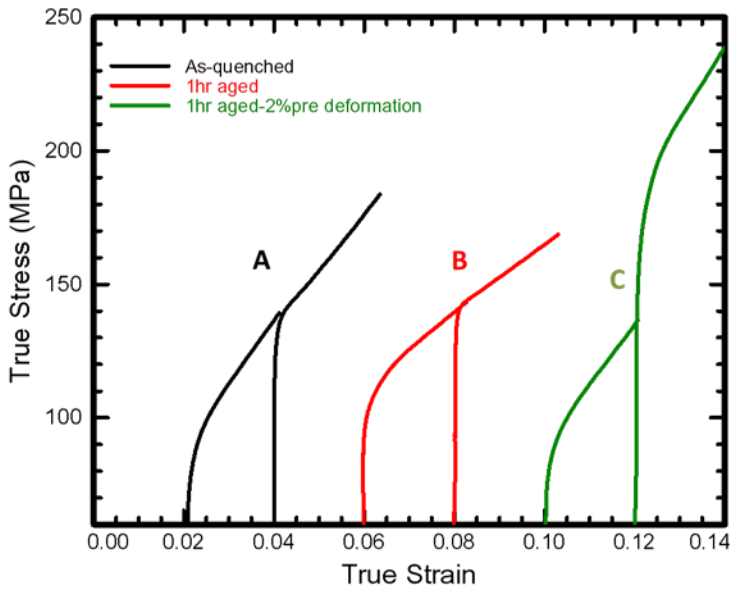

Fig. 4. 47. True stress–strain graphs of three cylindrical samples of Mg- 0.2 wt. %Zn-3 wt. % Nd alloy. Graph A is for the as-quenched sample loaded to 2%, unloaded, and immediately reloaded to total strain fo 4%. Graph B is for the as-quenched sample which is aged at 200°C for 1hr followed by the same compression procedure as the first sample. Graph C is for the as-quenched sample, loaded to 2%, aged at 200°C for 1hr, and reloaded to 2% more compression strain (total of 4%).

.

The plots showed that for sample A, yielding happens at around 85 MPa. This value increases to about 105 MPa for the 1hr aged sample which is expected. However, for sample C after the same heat treatment, the yield strength increases to about 170 MPa. The common expectation was that upon the heat treatment of the deformed alloy, the yield strength should drop due to annihilation of dislocations which happens during the recrystallization and recovery [63]. We examined the microstructure of this alloy by optical microscope. As was expected in magnesium, deformation at room temperature is accompanied by formation of twins in the grains. Fig. 4. 48 (a) and (b) show the optical micrographs after the first loading in the as-quenched sample. Also Fig. 4. 48 (c) and (d) present the optical micrographs taken from the same grains (a) and (b) after second loading.

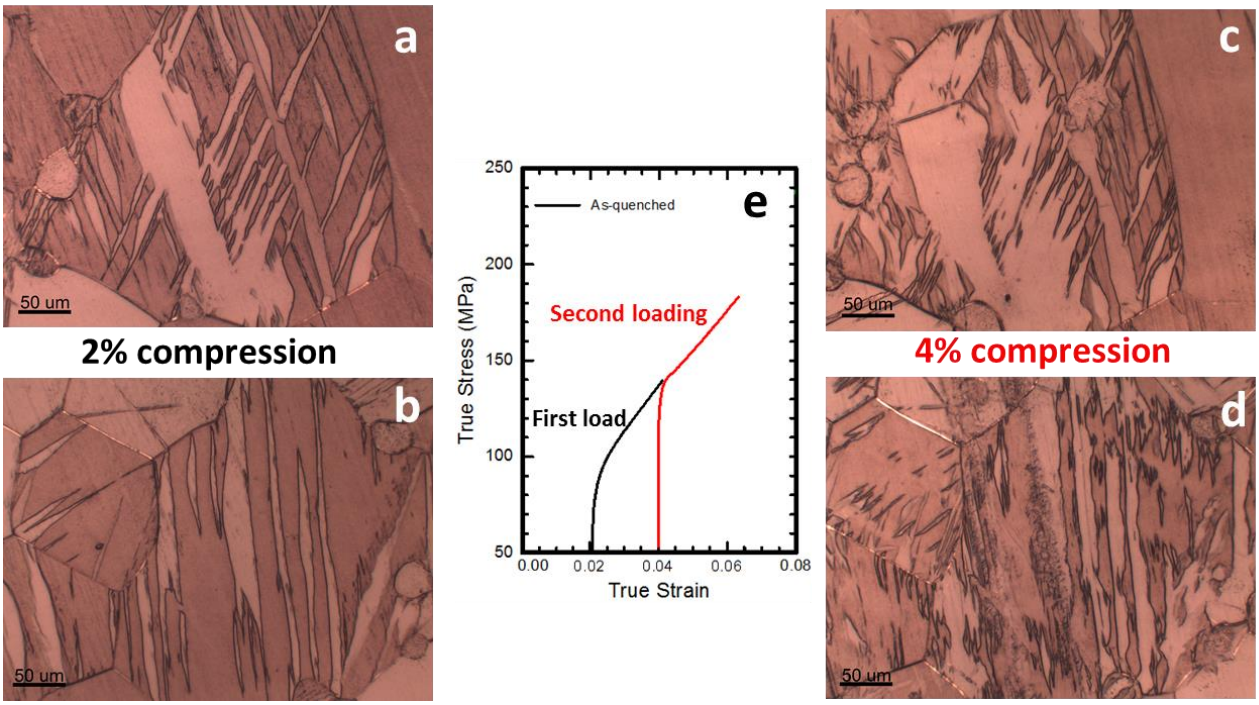

Fig. 4. 48. Optical micrographs of the as-quenched sample: a) and b) after first loading to 2% compression strain; c) and d) after second loading to a total compression strain of 4%. e) The true stress-strain curve is brought for clarification.

Careful comparison between the microstructure of the sample before and after loading revealed that the majority of the deformation twins continue to grow after second loading. Examples can be seen in Fig. 4. 48. (c) and (d). However, as shown in Fig. 4. 49 (a)-(d) for the pre-deformed 1hr aged sample, significant number of twins did not grow after second loading. Instead, new twins nucleated and grew in the grains (for instance compare Fig. 4. 49 (a) and (b)).

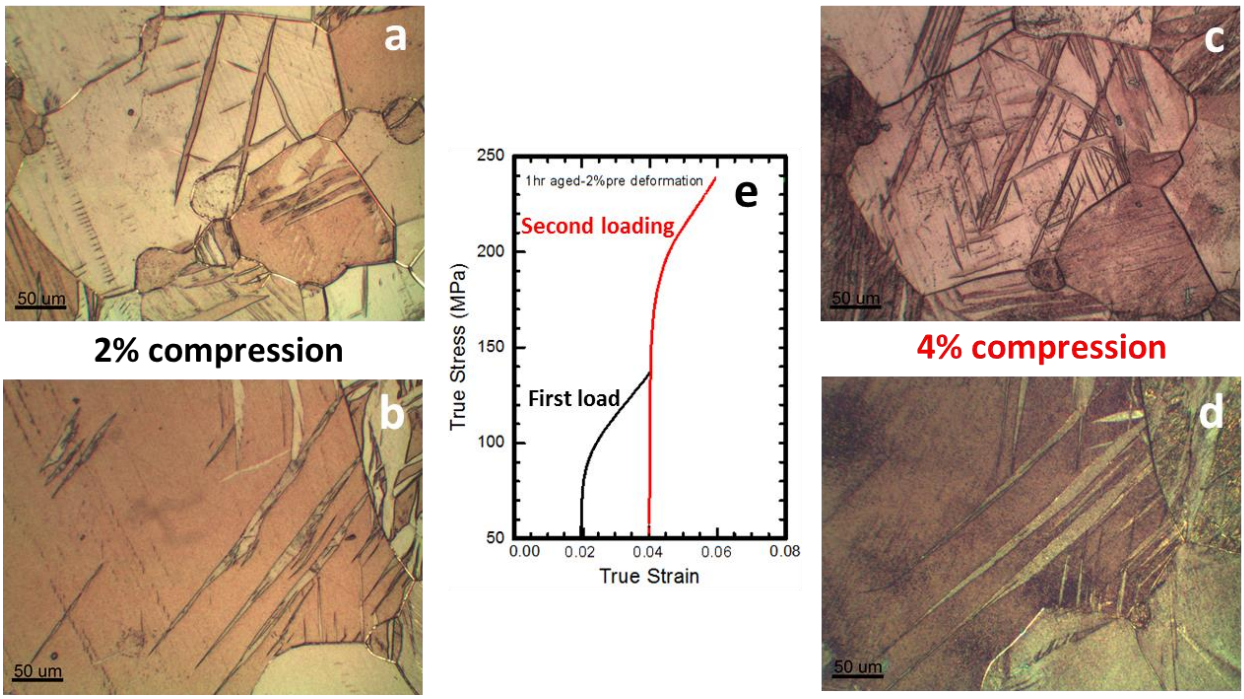

Fig. 4. 49. Optical micrographs of the as-quenched sample: a) and b) after first loading to 2% compression strain; c) and d) after second loading to a total compression strain of 4%. e) The true stress-strain curve is brought for clarification.

We postulated that this behavior may be attributed to the segregation of solute atoms along the existing twin boundaries. Since the atomic radius of solute atoms is quite different than Mg, segregation of these atoms along twin boundaries results in reducing the strain energy in the matrix, and pinning effect. The strain energy may come from the formation of defects or

presence of solute atoms with different radius in the matrix. Consequently, the deformation should continue by formation of new twins in the matrix which leads to higher observed yield strength in the pre-deformed alloy.

We further analyzed the microstructure of the pre-deformed alloy by means of HAADF-STEM technique. Fig. 4. 50 shows a low angle bright field and high resolution HAADF-STEM images of the pre-deformed 1hr aged sample taken with beam parallel to [0001]. In Fig. 4. 50 (a) and (b), we can notice the segregation of solute atoms on twin boundaries that introduce the pinning effect observed in Fig. 4. 49. Indeed, deformation of the sample leads to introduction of a large concentration of defects into the structure. These defects in the form of vacancies, dislocations, and twins act as heterogeneous nucleation sites for precipitation of the new phase. Therefore segregation of solute atoms into these sites, not only leads to pinning of the defects at early stages of heat treatment, but results in nucleation and growth of the new phase from these sites as aging proceeds. Fig. 4. 50. (c) which is taken from the region specified by red square (Fig. 4. 50 (b)) shows the formation of metastable phases on the twin boundary.

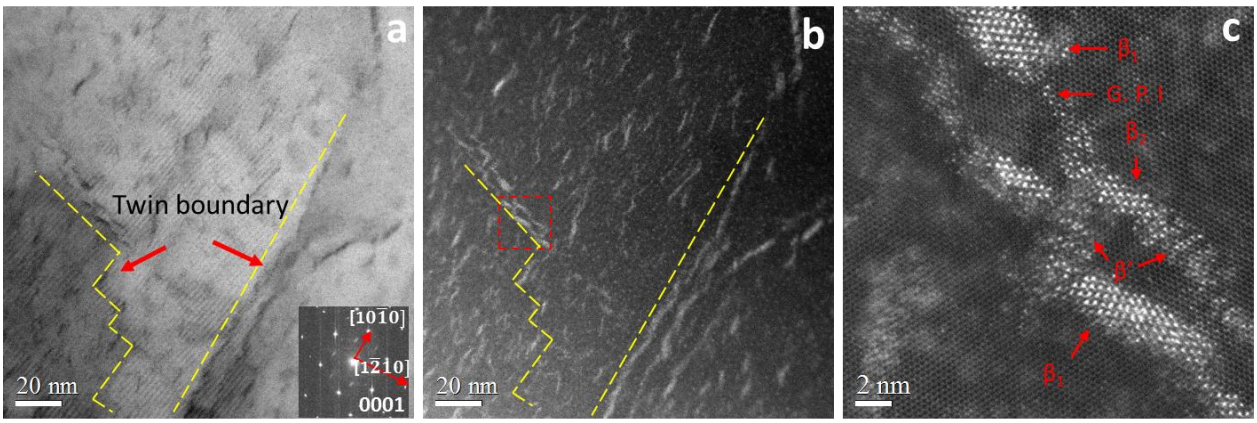

Fig. 4. 50. a) low angle bright field image of the sample, pre-deformed to 5% compression strain and aged at 200°C for 1hr; b) high resolution HAADF-STEM image from the same region as the first image; c) higher magnification of the region defined by red square in image (b).

Further investigations of the microstructure also revealed the segregation of solute atoms into basal dislocations. This is presented in Fig. 4. 51 (a)-(c). Formation of β' and β_1 phases and significant number density of these precipitates after only 1hr aging shows the effect of defects in acceleration of aging behavior in these alloys. The findings from STEM analysis are in excellent agreement with the results of compressions test and optical micrographs and confirm the solute segregation phenomenon in the deformed alloy.

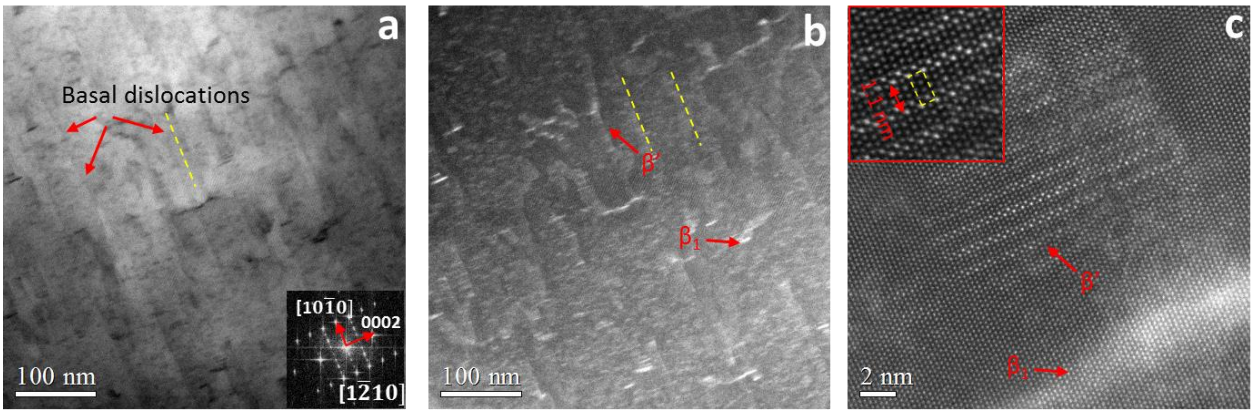

Fig. 4. 51. a) low angle bright field image of the sample, pre-deformed to 5% compression strain and aged at 200°C for 1hr; b) high resolution HAADF-STEM image from the same region as the first image; c) higher magnification of the region defined by red square in image (b).

As discussed earlier, the formation of small Nd-Zn atom clusters in the studied system was confirmed by APT analysis of the under-aged alloy. In addition, we identified and observed the segregation of solute atoms into the defects such as dislocations in the pre-deformed alloy. If a dislocation on basal plane is considered in an under-aged sample and the dislocation is in close proximity of Nd-Zn clusters, by gliding of the dislocation toward clusters, the strain energy of the dislocation can be reduced if clusters dissociate into the dislocation core. This may occur by segregation of larger solute atoms (Nd) into tension region and segregation of smaller solute

atoms (Zn) into compression region, as shown in Fig. 4. 52. Therefore, segregation of solute atoms into dislocations not only reduces the strain energy of a dislocation but decreases the strain energy produced by the presence of Nd (larger solute atom) and Zn (smaller solute atom) in the system which leads to a stronger pinning effect in Mg-Nd-Zn alloys.

The pinning effect of solute atoms can be also related to high creep resistance of these alloys. Since in magnesium alloys, the creep phenomenon occurs mostly through dislocation climb and viscous dislocation glide [40], pinning of the dislocations by segregation of solute atoms can result in higher resistance against dislocation motion and consequently higher creep resistance. Segregation of solute atoms into defects have been observed and studied in other systems as well [40, 89-92].

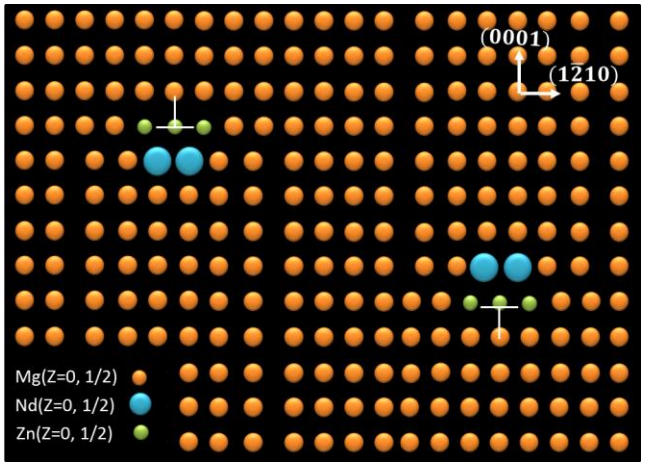

Fig. 4. 52. Schematic image of the Mg matrix showing the segregation of Nd-Zn clusters into basal dislocations. The Nd atoms replace the Mg atoms in tension zones while Zn atoms replace Mg atoms in compression zones of the two edge dislocations.

4. 8. 2. DSC analysis of deformed alloys

The effect of prior deformation on the kinetics of precipitation was studied by means of DSC technique. 16 identical samples were chosen and divided into 4 sets of 4 samples. The 4 sets were then loaded to 0%, 0.5%, 2.5%, and 5% compression strain. For each set of samples with same compression strains, DSC test were conducted at 4 hating rates of 5, 10, 15, and 20 °C/min. The results are presented in Fig. 4. 53. As can be noticed, at a constant heating rate, the position of the first peak (G. P. zones) slightly shifts to higher temperatures with the increase in compression strain while this shift for the second peak (β') is smaller. However, a large shift to lower temperatures is observed for the third exothermic peak (β_1) in a way that for 5% strain, the second and third peaks are almost merging into one.

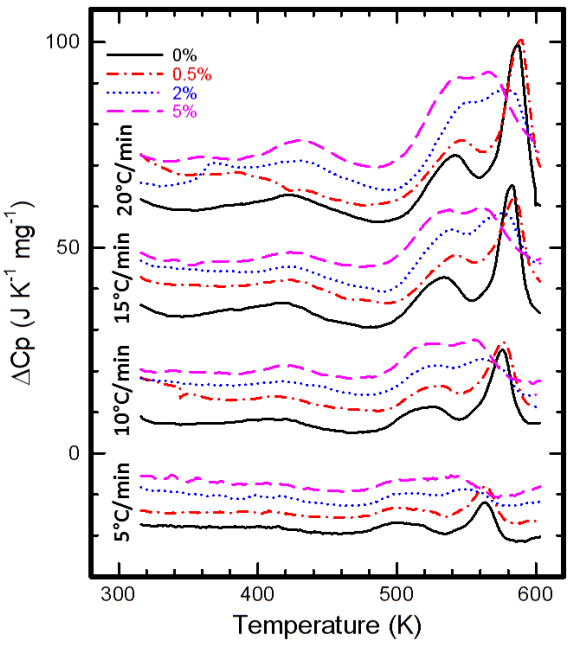

Fig. 4. 53. DSC traces of as-quenched samples strained to different amount of strains. A set of 4 samples with same amount of compression strain were analyzed at 4 hating rates of 5, 10, 15, and 20 °C/min.

This implies that deformation has a slight negative effect on precipitation kinetics of G. P. zones as well as β'/β_2 while there is a larger effect on precipitation kinetics of β_1 phase. This was more obvious when the microstructure of the 2hr aged sample was compared to the microstructure of the pre-deformed 1hr aged sample. The comparison revealed a lower density of early stage precipitates (i.e. G. P. zones) and higher number density of β_1 precipitates with larger size for the pre-deformed 1hr aged sample.

From the DSC traces, we calculated the growth activation energies of the phases in deformed samples. The results are presented in table 4. 3. As seen, the activation energy for the G. P. zones as well as β'/β_2 increases. However, the activation energy for the growth of β_1 significantly decreases to a value close to the activation energy of G. P. zones and β'/β_2. This indicates that β_1 phase can precipitate out at the same rate as the early stage precipitates. As was shown earlier, the formation of G. P. zones and β'/β_2 precipitates depends on the concentration of quenched-in vacancies. Upon introduction of the deformation in to the system, a large number of dislocations and twins are produced in the structure. These defects act as sinks for the excess vacancies, hence decrease the concentration of quenched-in vacancies in the matrix. Annihilation of vacancies into these defects results in dissolution of some solute-vacancy clusters leading to a lower growth kinetics (higher activation energy) for G. P. zones as well as β'/β_2 phases. Similar results have been reported in Al-Mg-Si system for the clustering of solute species [67].

In terms of the increase in the kinetics of β_1 precipitation, a possible reasoning can be described as follows. The precipitation of β_1 phase does not depend on the concentration of clusters. Instead, it depends mainly on the deformation of the origin phase as described in the transformation of β_2 to β_1. It was observed that for transformation of β_2 to β_1, a shearing of the origin phase in $[1\bar{2}10]$ has to take place. The magnitude of the shear strain was calculated as

0.18. Formation of dislocations of type $\{0001\}<1\bar{2}10>$ and $\{10\bar{1}0\}<1\bar{2}10>$ upon deformation of the matrix will introduce a shear strain in $<1\bar{2}10>$ direction. In addition, formation of twins in magnesium is accompanied by shearing of the matrix. For the twins of type $\{10\bar{1}2\}$ and $\{10\bar{1}1\}$, the shear strain introduced into the system is $1/3<1\bar{2}10>$ [93]. Therefore, introduction of dislocations as wells as twins into the system upon deformation of the alloy will assist the formation of β_1 through shearing of the matrix in the same direction. The proposed hypothesis well agrees with the decrease in growth activation energy of β_1.

Table 4. 3. Activation energies of the phases form during heat treatment of as-quenched samples. The values reported are activation energy values in kJ/mol.

Phase	G. P. zones	β'/β_2	β_1
0.0% deformation	75	77	150
0.5% deformation	87	80	143
2.5% deformation	91	82	119
5.0% deformation	92	93	94

4. 8. 3. Deformation analysis of peak-aged alloy

Hardness measurements on the aged alloys showed a peak-aging condition after 8hr aging at 200°C. Microstructure analysis of 8hr aged sample also revealed the presence of mainly β_1 in the structure. To further investigate the effect of deformation on peak aging condition, 4 as-quenched samples were deformed to 0%, 0.5%, 2.5%, and 5% compression strain.

Fig. 4. 54 shows the true stress-strain curves for the pre-deformed peak-aged samples. From these curves we noticed an increase in the compression yield strength as the deformation increases. For the 8hr aged sample, the yield strength at 0.002 strain was measured as 180 MPa (curve A in the Fig. 4. 54. (b)). For the 0.5% pre-deformed sample (curve B), there was no significant change in yield strength value. On the other hand, for the 2.5% (curve C) and 5% (curve D) strained samples, the yield strength increases to about 215 MPa and 250 MPa, respectively. Although the deformation of the matrix accelerates the kinetics of β_1 precipitation, we expected to observe an over-aged condition for the deformed 8hr aged sample. The increase in the yield strength may be attributed to two possible reasons as described below:

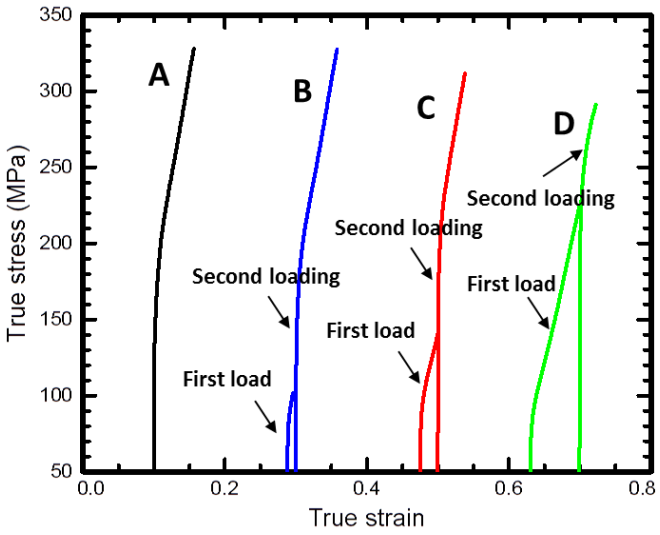

Fig. 4. .54. True stress-true strain curves for the pre-deformed samples. All samples are aged for 8hr at 200°C after deformation.

1) Higher magnitude of compression strain introduces a larger concentration of defects into the system. Therefore, segregation of solute atoms into these defects results in pinning of a large number density of defects in the system. This is evident in Fig. 4. 55, taken from the pre-

deformed 8hr aged sample. As noticed in Fig. 4. 55 (a), a trace of large number density of dislocations is visible in the matrix due to segregation of solute atoms into these defects. In addition, Fig. 4. 55 (b) and (c) show the segregation of solute atoms into twin boundaries in the same sample. The preventative role of solute segregation in dislocation annihilation and twin recovery after 8hr aging may lead to a higher strength for the deformed alloy.

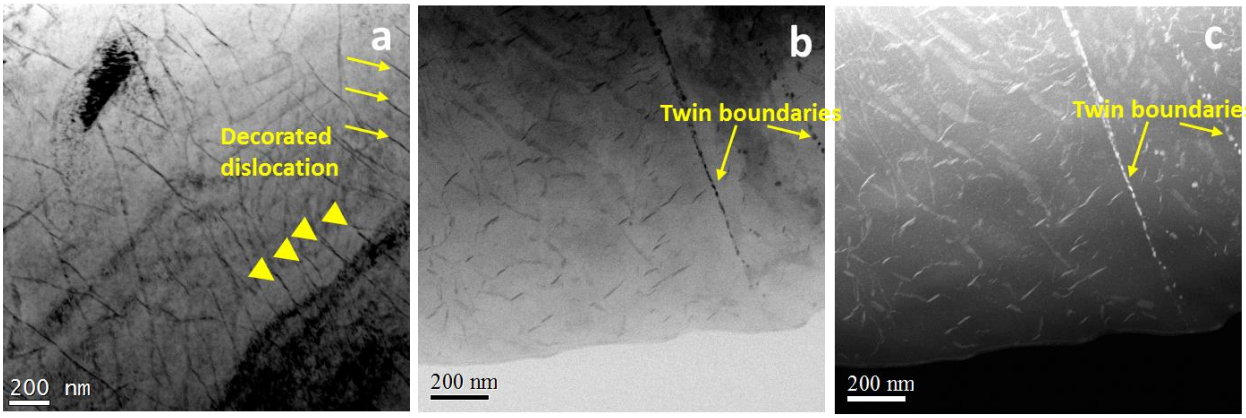

Fig. 4. 55. a) Bright filed TEM image showing solute segregation in dislocations in the matrix; b) low angle bright field and c)HAADF-STEM images showing solute segregation in the sample aged at 200°C for 8hr and pre-deformed 5%.

2) Fig. 4. 56 shows the DSC traces of the pre-deformed alloys. We observe a shift in the third peak toward lower temperatures, as was seen earlier for the as-quenched sample. The peak shift and a much lower height imply that the kinetics of precipitation for β_1 increases as the deformation increases, therefore a larger number density of β_1 is expected in the microstructure. Since this phase has the main contribution in the precipitation hardening, higher concentration of this phase in the alloy leads to a higher yield point for the alloy.

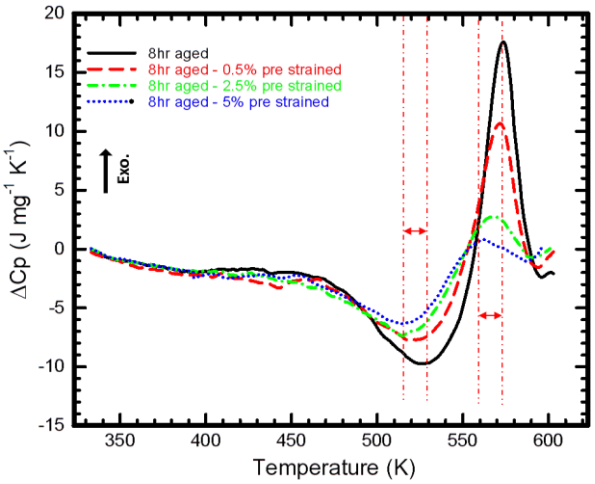

Fig. 4. 56. DSC traces of the samples aged at 200°C for 8hr. The samples are pre-deformed to different amount of compression strain prior to aging.

To investigate this matter, microstructure of the sample was examined by STEM. The sample is a 5% pre-deformed alloy aged to 200°C for 8hr. As seen from Fig. 4. 57 (a) and (b), the main detected phase in this condition is β_1 which is consistent with the DSC results. In addition to this phase, the presence of β' was detected in the matrix.

Another interesting feature in the microstructure of deformed alloys was significant presence of long zigzag chain precipitates indicated by yellow rectangles in Fig 4. 57. These chains are formed either by attachment of smaller β' precipitates on $\{1\bar{2}10\}$ planes (Fig. 4. 57 (a)) or smaller β_1 precipitates on $\{10\bar{1}0\}$ planes (Fig. 4. 57 (b)). High resolution images taken from these chains show that the chains start to form by formation of β' precipitates on $\{1\bar{2}10\}$ as shown in Fig. 4. 58 (a) with two atomic layer discontinuity in $\{2\overline{11}0\}$ between individual β' precipitates. These precipitates transform to β_1 by formation of β_2 phase at the interface of β'/β_1. The thickness of the transformation zone (i.e. β_2 phase) is on the order of a few atomic layers (Fig. 4. 58 (b)).

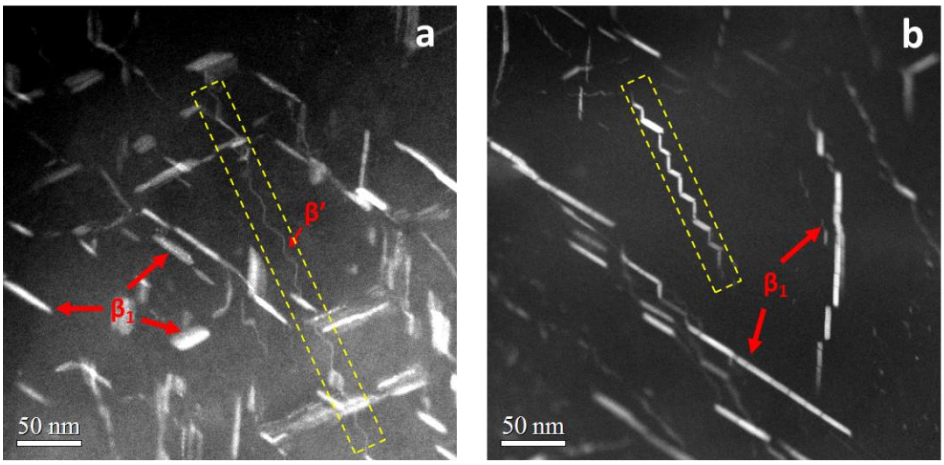

Fig. 4. 57. HAADF-STEM images of the sample aged at 200°C for 8hr. The sample was pre-deformed for 5% compression strain prior to aging.

It appears that the phase transformation starts and proceeds locally from the smaller surface of *β'* phase rather than a global transformation of *β'*. This is visible in Fig. 4. 58 (a) and (b) for partially transformed *β'* phase. On the other hand, β_1 precipitates often contain a planar defect in the microstructure along $[0\bar{1}1]$ direction, as indicated in Fig. 4. 58 (c). These defects result in the presence of two or more domains within a single β_1 phase. Since the orientation relationship of individual domains with the matrix and the morphologies are the same, these domains are the same variant of β_1. Therefore, the domains seem to form by an in-situ transformation of *β'* to β_1. From above observations, it can be concluded that *β'* can transform into β_1 by both local and global (in-situ) transformation.

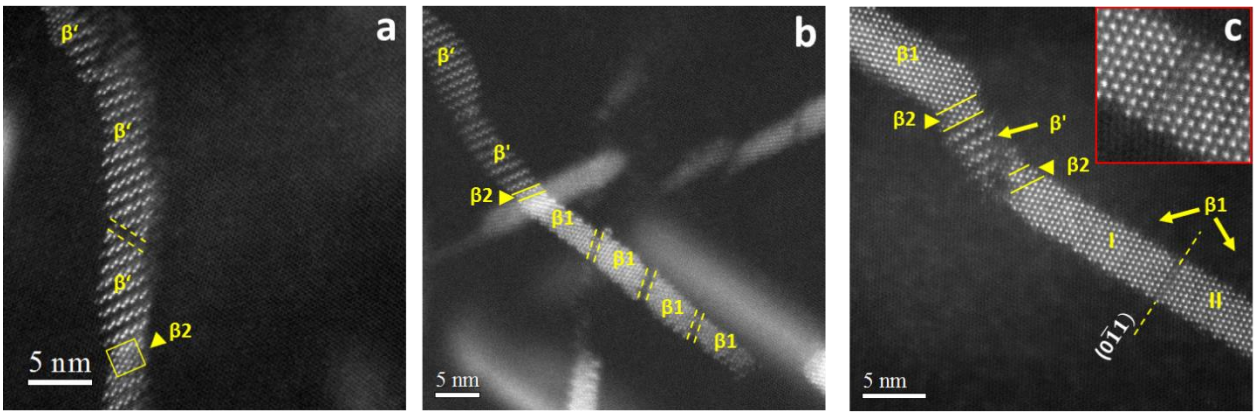

Fig. 4. 58. High resolution HAADF-STEM images of the smaller components of zigzag chains: a) *β'* precipitates as the main component in the chain; b) partial transformation of *β'* to β_1; c) β_1 precipitates as the main component in the chain.

As noticed from the DSC traces of the pre-deformed samples in Fig. 4. 56., the endothermic peak also shifts to lower temperatures with the increase in amount of deformation. Our earlier quantitative analysis showed that the shift of the dissolution peak to lower temperatures is accompanied by a decrease in the average size of the precipitates formed prior to formation of β_1. As we observed in STEM images, the large precipitates are indeed composed of smaller precipitates on the order of 5-10 nm with 2 atomic layer distance between them (Fig. 4. 58. (a) and (b)). Therefore, if the average size of the precipitates is considered based on the small components of the large precipitates, the behavior observed in DSC is consistent with the micrograph observations.

4. 9. Atom probe tomography analysis

The distribution of solute atoms in the precipitates was investigated by means of atom probe tomography (APT) technique. Fig. 4. 59 shows the APT elemental maps taken from the sample that was aged for 2hr at 200°C. The ion maps revealed the presence of long and thin precipitates that were elongated in z direction. The shape of these precipitates is consistent with what was found earlier for the G. P. zones and *β'*. A closer examination of the ion map reveals that the precipitates are not only enriched in Nd (indicated by green color), but contain higher content of Zn with respect to the matrix.

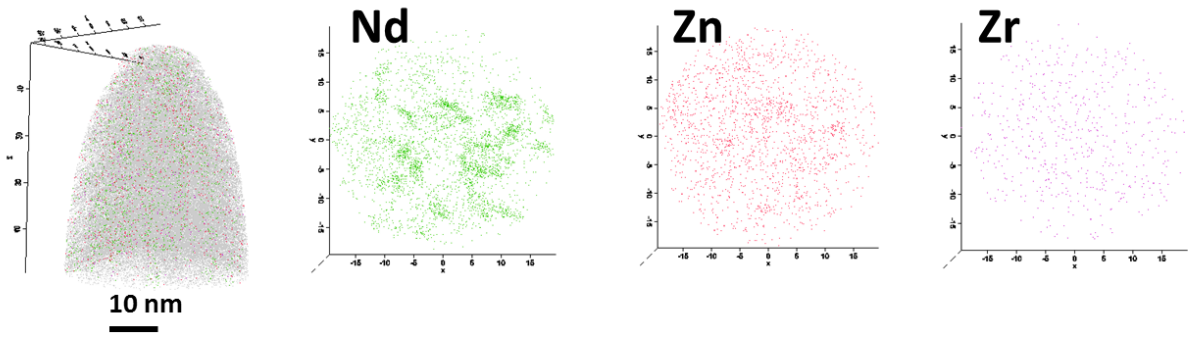

Fig. 4. 59. APT elemental maps in the sample aged at 200°C for 2hr. The maps show the distribution of Nd (green), Zn (red), and Zr (purple) in the matrix as well as the second phase.

The presence of Zn in the precipitates was more pronounced in the ion maps of the sample pre-deformed for 5% compression strain and aged for 8hr at 200°C. This is shown in Fig. 4. 60 in the reconstructed ion maps taken from this sample as well as the elemental reconstruction of a precipitate. The composition of the precipitates was studied in both samples and two main compositions were found as Mg- 12Nd-5Zn and Mg-21Nd-5Zn (at. %). Comparing the composition and size of the precipitates found in atom probe with the proposed compositions and

sizes for the detected precipitates in these two samples, the first composition can be related to β' while the second composition is attributed to β_1. The presence of Zn in the structure of the metastable phases is consistent with the earlier hypothesis for the growth mechanism of β_1 precipitates in the matrix.

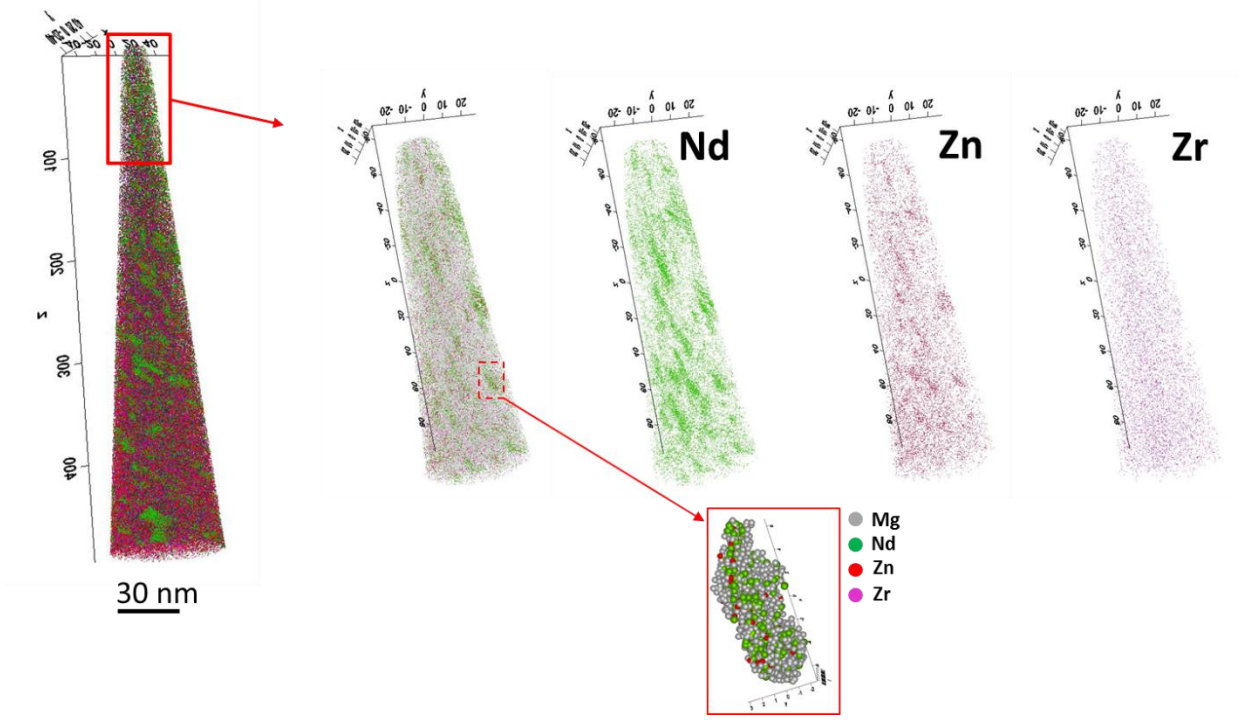

Fig. 4. 60. 3D APT elemental maps in the sample pre-deformed for 5% compression strain and aged for 8hr at 200°C. The maps show the distribution of Nd (green), Zn (red), and Zr (purple) in the matrix as well as the second phase.

The position of the Zn atoms in the structure cannot be deduced from APT analysis. However, since the amount of Nd atoms found by APT is less than what we expected from the structure of the precipitates, it is more likely that Zn atoms replace a portion of Nd atoms in the structure of the metastable phases. Since the atomic radius of Zn is smaller than Mg and Nd, the substitution of Zn atoms with Nd atoms can reduce the strain energy that is associated with the presence of larger Nd atoms in the structure.

Chapter 5

5. Conclusion

In this research, the microstructure evolution and kinetics of precipitation in age-hardening Mg-0.2 %Zn- 3%Nd alloy were studied. The major outcome of this research can be summarized as follows:

1) Careful STEM and TEM analysis of the microstructure of the samples aged at 200°C revealed the presence of some new phases in the microstructure in addition to the old description *Super saturated solid solution (SSSS)→ G. P. zones → β'' → β' → β,* reported for binary Mg-Nd alloy. The precipitation sequence for this alloy was identified as: *Super saturated solid solution (SSSS)→ Clusters of atoms → G. P. zones (I, II, III) → β' → β_2 → β_1 / γ' → β.*
2) Although DSC analysis did not reveal significant heat evolution as a result of clustering of atoms, the presence of clusters of solute atoms was confirmed by STEM and APT techniques. The formations of atom clusters, G. P. zones of different type, and β_2 phase

have not been reported for the binary Mg-Nd and ternary Mg-Nd-Zn system. Similarity of the structure of G. P. zones I and II with β' and G. P. zones III with β_2 shows that G. P. zones serve as nuclei for β' and β_2 phases.

3) Our measurements showed that the lattice parameter b for the orthorhombic β' phase is different from the one reported for Mg-RE alloys. Our microstructure observations showed that this is due to a different arrangement of atoms in β' phase formed in Mg-Nd-Zn alloy.
4) The intermediate β_2 phase detected in this study is a new phase with orthorhombic structure, lattice parameters of $a_{\beta 2}$= 0.64 nm, $b_{\beta 2}$= 0.56 nm, $c_{\beta 2}$= 0.52 nm and composition of Mg_3Nd. Our analysis showed that this phase is indeed a transition phase in the transformation of β' to β_1.
5) A unit cell of β_1 phase is produced through shearing and expansion of the β_2 unit cell. In addition, our structural model based on high resolution STEM images showed that the structure of β_1 is indeed BCT rather than reported FCC structure for this phase.
6) The higher yield strength of pre-deformed alloys may be associated with the pinning effect resulted from segregation of solute atoms into dislocations as well as twin boundaries. Analysis showed that the presence of atom clusters can enhance the pinning effect of solute atoms and further improve the strength and creep resistance of these alloys.
7) Our kinetic studies revealed that the concentration of quenched in vacancies is critical in growth kinetics of G. P. zones and β'/ β_2. The presence of quenched in vacancies in the solid solution state leads to a lower activation energy of the growth for these precipitates at higher annealing temperatures.

8) DSC analysis of the deformed alloys revealed that prior deformation enhances the kinetics of β_1 precipitation while it has slight negative effect on precipitation of prior phases. The negative effect was attributed to the annihilation of quenched in vacancies. The positive effect on β_1 precipitation was attributed to the effect of shear strain caused by basal dislocations and twins in lowering the required energy for shearing of β_2 in β_2/β_1 transformation.

References

[1] Z. Xingwei, D. Jie, L. Wencai, D. Wenjiang, Microstructure and mechanical properties of NZ30K alloy by semicontinuous direct chill and sand mould casting processes, Res. Dev. 8 (2011) 41.

[2] N. Stanford, M. Barnett, Effect of composition on the texture and deformation behavior of wrought Mg alloys, Scripta Mater. 58 (2008) 179.

[3] R. Gehrmann, M. M. Frommert, G. Gottstein, Texture effects on plastic deformation of magnesium, J. Mater. Sci. Eng. A 395 (2005) 338.

[4] K. Hantzsche, J. Bohlen, J. Wendt, K. Kainer, S. Yi, D. Letzig, Effect of rare earth additions on microstructure and texture development of magnesium alloy sheets, Scripta Mater. 63 (2010) 725.

[5] R. K. Mishra, A. K. Gupta, P. R. Rao, A. K. Sachdev, A. Kumar, A. Luo, Influence of cerium on the texture and ductility of magnesium extrusions, Scripta Mater. 59 (2008) 562.

[6] D. Wu, R. S. Chen, E. H. Han, Excellent room-temperature ductility and formability of rolled Mg-Gd-Zn alloy sheets, J. alloys Comp. 509 (2011) 2856.

[7] T. J. Pike, B. Noble, The formation and structure of precipitates in a dilute magnesium-neodymium alloy, J. the Less-Common Met. 30 (1973) 63.

[8] L. Ma, R. K. Mishra, M. P. Balogh, L. Peng, A. A. Luo, A. K. Sachdev, W. Ding, Effect of Zn on the microstructure evolution of extruded Mg-3Nd(-Zn)-Zr (%wt.) alloys, J. Mater. Sci. Eng. A 543 (2012) 12.

[9] P. A. Nuttall, T. J. Pike, B. Noble, Metallography of Dilute Mg-Nd-Zn alloys, Metallography 13 (1980) 3.

[10] M. Arnaud, Update on the assessment of magnesium status, *British J. Nut.* 99(2008) S24.

[11] J. F. Anthony, The chemical composition of seawater, (2006).

[12] B. U. Pal, A. C. Powell, The use of Solid-Oxide Membrane Technology for Electrometallurgy, JOM 59 (2007) 44.

[13] A.Sanaty-Zadeh, X. Xia, A. A. Luo, D. S. Stone, Precipitation evolution and kinetics in a magnesium-neodymium-zinc system, J. Alloys Comp. 583 (2013) 434.

[14] A. Kielbus, T. Rzychon, R. Gibis, Microstructure of AM50 die casting mangnesium alloy, J. Achiev. Mat. Manufac. Eng. 18 (2006) 135.

[15] C. Yan, R. X. Bai, Y. T. Gu, W. J. Ma, Investigation on mechanical behavior of AM60 magnesium alloys, J. Achiev. Mat. Manufac. Eng. 31 (2008) 398.

[16] S. M. He, L. M. Peng, X. Q. Zeng, W. J. Ding, Y. P. Zhu, Comparison of the microstructure and mechanical properties of a ZK60 alloy with and without 1.3 wt. % gadolinium addition, Mat. Sci. Eng. A 433 (2006) 175.

[17] H. Watanabe, T. Mukai, M. Mabuchi, K. Higashi, High strain rate super plasticity at low temperature in a ZK61 magnesium alloy produced by powder metallurgy, Scripta Mater. 41 (1999) 209.

[18] ASTM standard B951, Standard Practice for Codification of Unalloyed Magnesium and Magnesium-Alloys, Cast and Wrought.

[19] M. M. Avedesian, H. Baker Magnesium and Magnesium Alloys, Handbook, ASM International 1999.

[20] B. Landkof, Magnesium Applications in Aerospace and Electronic Industries, in Magnesium Alloys and their Applications, ed. K. U. Kainer, Wiley-VCH Verlag GmbH & Co. KGaA, Weinheim (2000).

[21] P. Mengucci, G. Barucca, G. Riontino, D. Lussana, M. Massazza, R. Ferragut, E. Hassan Aly, Structure evolution of a WE43 Mg alloy submitted to different thermal treatments, Mat. Sci. Eng. 479 (2008) 37.

[22] C. Lee, J.-B. Lee, D.-H. Park, S.-J. Na, Fiber Laser Welding of Noncombustible Magnesium alloy, Mat. Sci. For. 580-582 (2008) 479.

[23] G. L. Esperance, P. Plamondon, M. Kunst, A. Fischersworring-Bunk, Characterization of intermetallics in Mg-Al-Sr AJ62 alloys, Intermet. 18 (2010) 1.

[24] X. Zheng, A. A. Luo, J. Dong, A. K. Sachdev, W. Ding, Plastic flow behavior of a high-strength magnesium alloy NZ30K, Mat. Sci. Eng. A 532 (2012) 616.

[25] J. Dai, J. Huang, M. Li, Z. Li, J. Dong, Y. Wu, Effect of heat treatments on laser welded Mg-rare earth alloy NZ30K, Mat. Sci. Eng. A 529 (2011) 401.

[26] W.J. Ding, P.H. Fu, L.M. Peng, H.Y. Jiang, X. Q. Zeng, Study on the microstructure and mechanical property of high strength Mg-Nd-Zn-Zr alloy, Mat. Sci. Forum 546-549 (2007) 433.

[27] X. Zheng, J. Dong, Y. Xiang, J. Chang, F. Wang, L. Jin, Y. Wang, W. Ding, Formability, mechanical and corrosive properties of Mg-Nd-Zn-Zr magnesium alloy seamless tubes, Mater. Des. 31 (2010) 1417.

[28] W. Wen-Xiang, J. Li, D. Jie, D. Wen-Jiang, Prediction of flow stress of Mg-Nd-Zn-Zr alloy during hot compression, Trans. Nonferrous. Met. Soc. China 22 (2012) 1169.

[29] D. Wenjiang, L. Daquan, W. Qudong, L. Qiang, Microstructure and mechanical properties of hot-rolled Mg-Zn-Nd-Zr alloys, Mater. Sci. Eng. A 483–484 (2008) 228.

[30] Q. Li, Q. Wang, Y. Wang, X. Zeng, W. Ding, Effect of Nd and Y addition on microstructure and mechanical properties of as-cast Mg-Zn-Zr alloy, J. Alloys Comp. 427 (2007) 115.

[31] X. Zhou, H. Zhou, Z. Zhang, R. Liu, L. Liu, Tensile properties of Hot Extruded Mg-Zn-Nd-Y-Zr alloy at elevated temperatures, Adv. Mat. Res. 415-417 (2012) 1157.

[32] Y. Lin, G. Xiao-dan, L. Li, Z. Peng, C. Li-Jia, L. Zheng, Microstructural evolution of rolled Mg-5Zn-3Nd(-Zr) alloy, Trans. Nonferrous Met. Soc. China 20 (2010) s498.

[33] R. Wilson, C. J. Bettles, B. C. Muddle, J. F. Nie, Precipitation hardening in Mg-3wt%Nd(-Zn) casting alloys, Mater. Sci. Forum 419-422 (2003) 267.

[34] J. F. Nie, B. C. Muddle, Characterisation of strengthening precipitate phases in a Mg-Y-Nd alloy, Acta Mater. 48 (2000) 1691.

[35] K. Saito, K. Hirage, The structures of Precipitates in an Mg-0.5at%Nd Age-Hardened Alloy Studied by HAADF-STEM Technique, Mat. Trans. 52 (2011) 1860.

[36] T. Honma, T. Ohkubo, K. Hono, S. Kamado, Chemistry of nanoscale precipitates in Mg-2.1Gd-0.6Y-0.2Zr (at.%) alloy investigated by the atom probe technique, Mat. Sci. Eng. A 395 (2005) 301.

[37] S. M. He, X. Q. Zeng, L. M. Peng, X. Gao, J. F. Nie, W. J. Ding, Precipitation in a Mg-10Gd-3Y-0.4Zr (wt.%)alloy during isothermal aging at 250°C, J. Alloy. Comp. 421(2006) 309.

[38] M. Nishijima, K. Hiraga, Structural Changes of Precipitates in an Mg-5 at.%Gd alloy, Mater. Trans. 48 (2007) 10.

[39] P. A. Carvalho, M. Sijbolts, B. J. Kooi, J. Th. M. De Hosson, High-resolution transmission electron microscopy study of discontinuously precipitated Ni_3Sn, Acta Mater. 48 (2000) 4203.

[40] J. F. Nie, K. Oh-ishi, X. Gao, K. Hono, Solute segregation and precipitation in a creep-resistant Mg-Gd-Zn alloy, Acta Mat. 56 (2008) 6061.

[41] O. Prat, J. Garcia, D. Rojas, J. P. Sanhueza, C. Camurri, Study of nucleation, growth and coarsening of precipitates in a novel 9%Cr heat resistant steel: Experimental and modeling, Mat. Chem. Phys. 143 (2014) 754.

[42] Z. W. Du, Z. M. Sun, B. L. Shao, T. T. Zhou, C. Q. Chen, Quantitative evaluation of precipitates in an Al-Zn-Mg-Cu alloy after isothermal aging, Mat. Char. 56 (2006) 121.

[43] M. Cabibbo, S. Spigarelli, A TEM quantitative evaluation of strengthening in an Mg-RE alloy reinforced with SiC, Mat. Char. 62 (2011) 959.

[44] F. Delmas, M. J. Casanove, P. Lours, A. Coujou, Quantitative TEM study of the precipitation microstructure in aluminum alloy Al(MgSiCu) 6056 T6, Mat. Sci. Eng. A, 373 (2004) 80.

[45] R. K. W. Marceau, L. T. Stephenson, C. R. Hutchinson, S. P. Ringer, Quantitative atom probe analysis of nanostructure containing clusters and precipitates with multiple length scales, Ultramicroscopy 111 (2011) 738.

[46] M. E. Krug, A. Werber, D. C. Dunand, D. N. Seidman, Core-shell nanoscale precipitates in Al-0.06 at. % Sc microalloyed with Tb, Ho, Tm or Lu, Acta Mater. 58 (2010) 134.

[47] D. Liu, B. Xiong, F. Bian, Z. Li, X. Li, Y. Zhang, F. Wang, H. Liu, In situ studies of microstructure evolution and properties of an Al-7.5Zn-1.7Mg-1.4Cu-0.12Zr alloy during retrogression and reaging, Mat. Des. 56 (2014) 1020.

[48] A. Deschamps, F. De Geuser, Z. Horita, S. Lee, G. Renou, Precipitation kinetics in a severely plastically deformed 7075 aluminum alloy, Acta Mater. 66 (2014) 105.

[49] C. Genevois, A. Deschamps, A. Denquin, B. Doisneau-cottignies, Quantitative investigation of precipitation and mechanical behavior for AA2024 friction stir welds, Acta Mater. 53 (2005) 2447.

[50] A. Luo, D. J. Lloyd, A. Gupta, W. V. Youdelis, Precipitation and dissolution kinetics in Al-Li-Cu-Mg alloy 8090, Acta Mater. 41 (1993) 769.

[51] M. Avrami, Kinetics of Phase Change. I General Theory, J. Chem. Phys. 7 (1939) 1103.

[52] M. Avrami, Kinetics of Phase Change. II Transformation Time Relations for Random Distribution of Nuclei, J. Chem. Phys. 8 (1940) 212.

[53] M. Avrami, Granulation, Phase Change, and Microstructure Kinetics of Phase Change. III, J. Chem. Phys. 9 (1941) 177.

[54] A. N. Kolmogorov, Statistical theory of crystallization of metals, ILZ. Akud. Nut&. SSSR, Ser. Mui. 3 (1937) 335.

[55] Erik Woldt, The relationship between isothermal and non-isothermal description of Johnson-Mehl-Avrami-kolmogorov Kinetics, J. Phys. Chem. Solids. 53 (1992) 521.

[56] Homer E. Kissinger, Reaction Kinetics in Differential Thermal Analysis, Anal. Chem. 29 (1957) 1702.

[57] A. Maigne, How to optimize your EELS experiments by adjusting the collection angle of your spectrometer, Gatan.com.

[58] Brian Langelier, Xiang Wang, Shahrzad Esmaeili, Evolution of precipitation during non-isothermal ageing of an Mg–Ca–Zn alloy with high Ca content, Mat. Sci. Eng. A 538 (2012) 246.

[59] Toyohiko J. Konno, Masahiro Kawasaki, Kenja Hirage, Direct imaging of Guinier-Preston zones by high-angle annular detector dark-filed scanning transmission electron microscopy, J. Elec. Microscopy 50 (2001) 105.

[60] C. S. T. Chang, J. Banhart, Low-Temperature Differential Scanning Calorimetry of an Al-Mg-Si Alloy, Met. Mat. Trans. A 42A (2011) 1960.

[61] Mourad Ibrahim Daoudi, Abdelhafid Triki, Abdelkrim Redjaimia, DSC study of the kinetic parameters of the metastable phases formation during non-isothermal annealing of an Al–Si–Mg alloy, J Therm Anal Calorim 104 (2011) 627.

[62] K. S. Ghosh, N. Gao, Determination of kinetic parameters from calorimetric study of solid state reactions in 7150 Al-Zn-Mg alloy, Trans. Non Ferr. Met. Soc. China 21 (2011) 1199.

[63] D. A. Porter, K. E. Easterling, Phase transformation in Metals and Alloys, Second ed. Chapman & Hall, 1992.

[64] Z. Liang, Clustering and Precipitation in Al-Mg-Si Alloys, PhD dissertation, University of Berlin, Germany 2012.

[65] M. Murayama, K. Hono, Pre-precipitate clusters and precipitation processes in Al-Mg-Si alloys, Acta Mater. 47 (1999) 1537.

[66] L. Zhen, S. B. Kang, DSC analyses of the precipitation behavior of two Al-Mg-Si alloys naturally aged for different times, Mat. Lett. 37 (1998) 349.

[67] Y. Birol, Pre-straining to improve the bake hardening response of a twin-roll cast Al-Mg-Si alloy, Scripta Mater. 52 (2005) 169.

[68] Y. Birol, Pre-aging to improve bake hardening in a twin-roll cast Al-Mg-Si alloy, Mat. Sci. Eng. A 391 (2005) 175.

[69] E. Donoso, Calorimetric study of the dissolution of Guinier-Preston Zones and η' Phase in AL-4.5at.%Zn-1.75at.%Mg, Mat. Sci. Eng. 74 (1985) 39.

[70] T. Honma, T. Ohkubo, S. Kamado, K. Hono, Effect of Zn additions on the age-hardening of Mg-2.0Gd-1.2Y-0.2Zr alloys, Acta Mater. 55 (2007) 4137.

[71] [63] X. Gao, S. M. He, X. Q. Zeng, L. M. Peng, W. J. Ding, J. F. Nie, Microstructure

evolution in a Mg-15Gd-0.5Zr (wt. %) alloy during isothermal aging at 250°C, Mat. Sci. Eng. A 431 (2006) 322.

[72] C. Antion, P. Donnadieu, F. Perrard, A. Deschamps, C. Tassin, A. Pisch, Hardening precipitation in a Mg-4Y-3RE alloy, Acta Mater. 51 (2003) 5335.

[73] F. E. Fujita, On the lattice deformation in martensite transformation, Met Trans. A 8 (1977) 1727.

[74] T. Waltz, V. Kazykhanov, H. P. Karnthaler, Martensitic phase transformations in nanocrystalline NiTi studied by TEM, Acta Mater. 52 (2004) 137.

[75] Y. G. Liu, H. I. Aaronson, Surface relief effects associated with γ plates in Al-15%Ag, Acta Met. 18 (1970) 845.

[76] U. Dahmen, K. H. Westmacott, Ledge Structure and the Mechanism of θ' Precipitate Growth in Al-Cu, Phys. Stat. Sol. (a) 80 (1983) 249.

[77] [69] P. Haasen, Physical metallurgy, Cambridge University Press, 1978.

[78] S. Esmaeili, X. Wang, D. J. Lloyd, W. J. Poole, On the precipitation-hardening behavior of the Al-Mg-Si-Cu alloy AA6111, Met. Mat. Trans. A 34A (2003) 751.

[79] P. Sepehrband, S. Esmaeili, Application of recently developed approaches to microstructural characterization and yield strength modeling of aluminum alloy AA7030, Mat. Sci. Eng. A 487 (2008) 309.

[80] M. J. Whelan, On the kinetics of particle dissolution, Met. Sci. J. 3 (1969) 95.

[81] A. Varschavsky, E. Donoso, The influence of particle shape on the non-isothermal kinetics of precipitate dissolution, Thermochi. Acta 69 (1983) 341.

[82] G. Jurgens, M. Kempe, H. Loffler, On the kinetics of the growth of Guinier-Preston zones (GPZ) in AlZn(2.5 at.%) Mg(X) alloys, Phys. Status Solidi A 21 (1974) K39.

[83] K. J. Perry, Solute-vacancy interaction energies and the effect of 0.009 at.% Mg on the aging kinetics of an Al-4.01 at.% Zn alloy, Acta Metall. 14 (1966) 1143.

[84] H. Liu, Y. Gao, J.Z. Liu, Y. M. Zhu, Y. Wang, J. F. Nie, A simulation study of the shape of β' precipitates in Mg-Y and Mg-Gd alloys, Acta Mater. 61 (2013) 453.

[85] K. E. Rajab, D. Doherty, Kinetics of growth and coarsening of faceted hexagonal precipitates in an f.c.c. matrix-I. Experimental observations, Acta Metall. 37 (1989) 2709.

[86] R.D. Doherty, K.E. Rajab, Kinetics of growth and coarsening of faceted hexagonal precipitates in an f.c.c. matrix-II.. Analysis, Acta Metall. 37 (1989) 2723.

[87] Z. Liang. C. S. T. Chang, C. Abromeit, J. Banhart, J. Hirsch, The kinetics of clustering in Al-Mg-Si alloys studied by Monte Carlo simulation, Int. J. Mat. Res. 8 (2012) 980.

[89] J. F. Nie, Y. M. Zhu, J. Z. Liu, X. Y. Fang, Periodic Segregation of Solute Atoms in Fully Coherent Twin Boundaries, Science 340 (2013) 957.

[90] J. M. Rosalie, L. Bourgeois, B. C. Muddle, Nucleation and growth of the γ'($AlAg_2$) precipitate in Al-Ag(-Cu) alloys, Acta Mater. 59 (2011) 7168.

[91] R. Herschitz, D. N. Seidman, Atomic Resolution Observations of Solute Atom Segregation To Stacking Faults in A Co-0.9 at.% Nb Alloy, Scripta Mater. 10 (1982) 849.

[92] R. Herschitz, D. N. Seidman, Atomic resolution observations of solute atom segregation effects and phase transitions in stacking faults in dilute cobalt alloys-I. Experimental results, Acta Metall. 33 (1985) 1547.

[93] W. F. Hosford, Mechanical Behavior of Materials, Sec ed., Cambridge University Press, 2010.

Appendix 1

A protocol for making TEM wedge sample out of metallic samples (Magnesium alloys)

There are different approaches for making wedge samples. The common method is that a sample is glued to the surface of a metallic (mostly aluminum) fixture and polished down to about 600μm thickness using diamond paper. This results in a flat surface with no scratches when the correct procedure and proper polishing paper are used. For the second side, the sample is detached from the aluminum fixture and is glued from the polished surface to a flat glass surface. The polishing is continued but in an angel of about 2°. This procedure is well established for semiconductors and produces good samples. However, in the case of metals, since the material is soft, the second side does not turn out great using the same procedure. This is due to difference in ductility of the material and the substrate. Since the metal is a lot softer than glass, upon polishing, the metallic sample is polished faster than the glass underneath and therefore, the edge of the sample goes away during polishing. The result is a thick edge which is not usable for TEM analysis. This is shown schematically in Fig. A-1.

I modified this method by introducing a substrate with similar ductility for the second side and polishing by three transitions from coarser papers to smoother one.

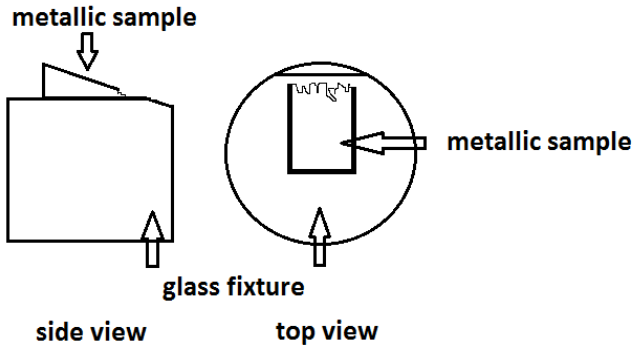

Fig. A-1. The side view and top view of the sample glued on the surface of the glass fixture. The edge of the sample is shown in the top view after polishing is jagged.

The procedure was to first attach a piece of metallic surface on the glass and flatten the surface on a zero angle. In next step, the sample with a polished surface is glued down to the surface of the metallic substrate from its polished side. The advantage of this fixture is that upon polishing, the substrate and the sample are polished uniformly with the same rate and therefore the edge of the sample is sharp and thin for TEM analysis (see Fig. A-2). The samples made with this method showed good results. Since water oxidizes magnesium alloys, an alcohol based lube (ABL) was utilized instead for final steps. The transitions from coarser to smoother papers for wedge polishing on the first side were as follow:

1- Polishing on 10 μm diamond paper down to 650 μm thickness using deionized water
2- Polishing on 3 μm diamond paper down to 600 μm thickness and using ABL
3- Polishing 10 μm more on 1 μm diamond paper and using ABL
4- Producing a mirror-looking surface by polishing on 0.1 μm for about 1.5 min and using ABL.

The procedure for the second side is as follow:

1- Polishing on 10 μm diamond paper down to 250 μm thickness using deionized water
2- Polishing on 3 μm diamond paper using ABL. This step is continued until the edge starts to go inward (sample becomes smaller), and then stopped immediately.
3- Polishing 10 μm more on 1 μm diamond paper using ABL. In this step, sample is polished slightly until all scratches from previous step are gone.
4- Producing a mirror-looking surface by polishing on 0.1 μm for about 3-4 min and using ABL.
5-

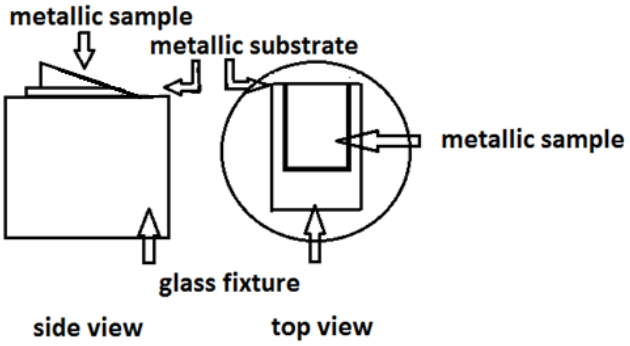

Fig. A-2. The side view and top view of the sample glued on metallic substrate. The edge of the sample is sharp and thin after the polishing on 0.1 μm diamond paper.

Appendix 2

Calculation of convergent angle and collection semi angle using diffraction patterns

Calibration of convergence angle (α) and EELS collection semi angle (β) (see Fig. B-1) was carried on by taking a series of convergent beam electron diffraction patterns on TEM and by using silicon as the reference material. Initially the sample was taken to [110] zone axis (or a known zone axis). The beam was then turned to convergent condition and the diffraction pattern was recorded (Fig. B-2. a). In the next step, the EELS detector with 2.5mm diameter was inserted. Upon inserting the detector, the shadow of the detector appears on the diffraction pattern. The diffraction pattern is again recorded with the shadow surrounding the diffraction spots (Fig. B-2. b). The two recorded patterns are then used to calculate the convergent and collection angels. In Fig. B-3, the procedures for calculating both angles are shown schematically. Following this procedure, and using the values for the electron wavelength and inter-planar spacing, the angles can be calculated. For the case of 300 kV, the wavelength of the electrons λ is 1.96996×10^{-12} m. Also the inter-planar spacing d (on [110] zone axis) for $(111)_{Si}$ plane is 3.14×10^{-10} m. Using this information, the convergent angel α and collection angel β for the instrument was calculated to be 3.697×10^{-3} and 1.166×10^{-3} radian respectively.

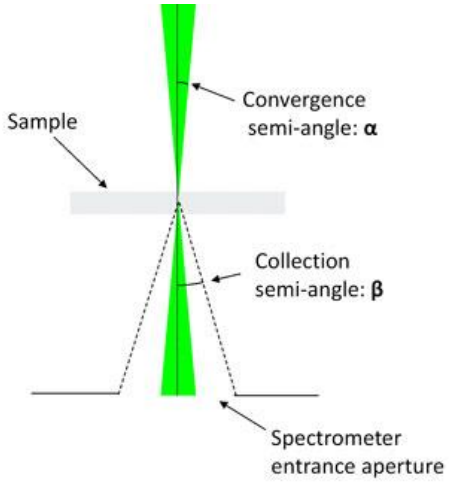

Fig. B-1. Schematic of the convergent angle and collection angle [57].

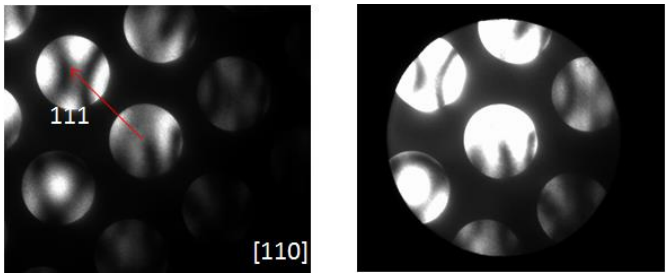

(a) (b)

Fig. B-2. Convergent diffraction patterns taken from silicon sample: a) without inserting EELS detector and b) after inserting the aperture. The aperture size is 2.5 mm. The beam is parallel to [110].

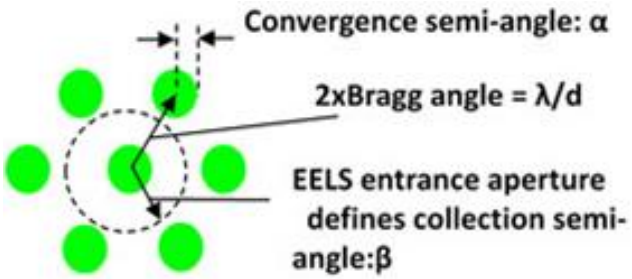

Fig. B-3. A schematic of how convergent angle and semi-collection angle are calculated from the recorded diffraction patterns. The calculated angles are in radian [57].

Appendix 3

Atom Probe Sample Preparation using Focused Ion Beam

Focused Ion Beam (FIB) is the technique that was used to make needle-shaped samples for APT analysis. In this regard, a 4×4×2 mm^3 sample was grinded with 1200 SiC grit and then polished with 0.3μm and 0.05μm alumina powder to achieve a smooth surface. The sample was then washed with ethanol and mounted on an AFM disc. The AFM disc was placed on a SEM stub for use in FIB.

After inserting the sample into the chamber, the sample was rotated to 54° and positioned at eccentric height with a working distance of 5.2 mm (After focusing). This position allows the sample to be at the coincidence point of electron beam and ion beam. This is shown schematically in Fig. C-1. After this step, the region of interest was coated with platinum coating to avoid removal of this region in later stage of milling by FIB. The dimension of the coating is roughly 32×3×1 μm^3. The sample was then rotated back to 24° angle. In this step a wedge sample is cut from the sample by milling the long sides of the coated region. Since the sample is positioned at 24°, the ion beam cuts the sample with a 30° angle. The ion milling is conducted with a 30kV, 8 nA Ga ion beam for a milling depth of about 20 micron and milling step of 15 layers. The milling region is a rectangle box of 30×2 μm^2. The milling region is positioned in a way that the bottom side of the milling region is at the top side of the coated region. Milling is conducted in the rectangle and from top to bottom. After milling the first side, sample is rotated 180° so that the bottom side of the coated region (un-milled side) is now on top. The second side is then milled using the same condition. Since during milling of the second side re-deposition of

some residue occurs on the first side, the sample is rotated back 180° after this step to its initial position and the first side is milled again with same condition for 30 seconds.

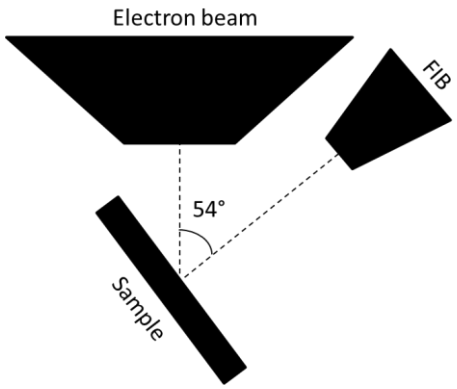

Fig. C-1. Schematic diagram of the relative positions of electron beam, Ga ion beam and sample in the chamber for APT sample preparation.

Upon completing the milling of the long sides of the wedge, sample is now rotated to 54° so that the ion beam is normal to the surface of the sample again. In this step, the left side of the coated region is milled with a 30kV, 2 nA Ga ion beam. The size of the milled region should be chosen such that the three milled sides of the sample are free after milling is done. This might be performed in a few steps for certainty.

In next step, the sample is welded to Omni probe micromanipulator using platinum. The welding should be strong enough to pull the sample out of the milled region once the right side is released. After this step, the right side of the sample is also milled using the same condition for the left side. A successful completion of this step leads to release of the wedge from the sample. The wedge is then pulled out by micromanipulator and the micromanipulator is kept at “parked” position.

To make needle-shaped samples, two type of Si coupons were used. Fig C. 2. show SEM images of a 22 posts and 36 posts Si coupons. On the 22 post coupon, each row includes 5 or 6 Si cone-shape posts with tip diameter of about 2 microns. On the 36 post coupon, there are 6 rows of 6 Si cone=shape posts with same dimension as the first type. The Si coupon is rotated 54° and aligned following the same procedure for the sample. After this step, the wedge is placed on top of the cone and welded to the Si post using electron beam deposition technique. Upon completion of the welding, a 2×2 microns (i.e. the area of the top surface of the wedge) wedge is cut from the original sample attached to micromanipulator using a 30kV, 2nA Ga ion beam. The procedure is repeated on other Si posts for however many needles that we intend to make.

Once the entire sample is used up, the deposition of platinum should be conducted on the second side of the wedge samples welded to Si posts. This is to make sure that there is a strong joint between the wedge and the Si post.

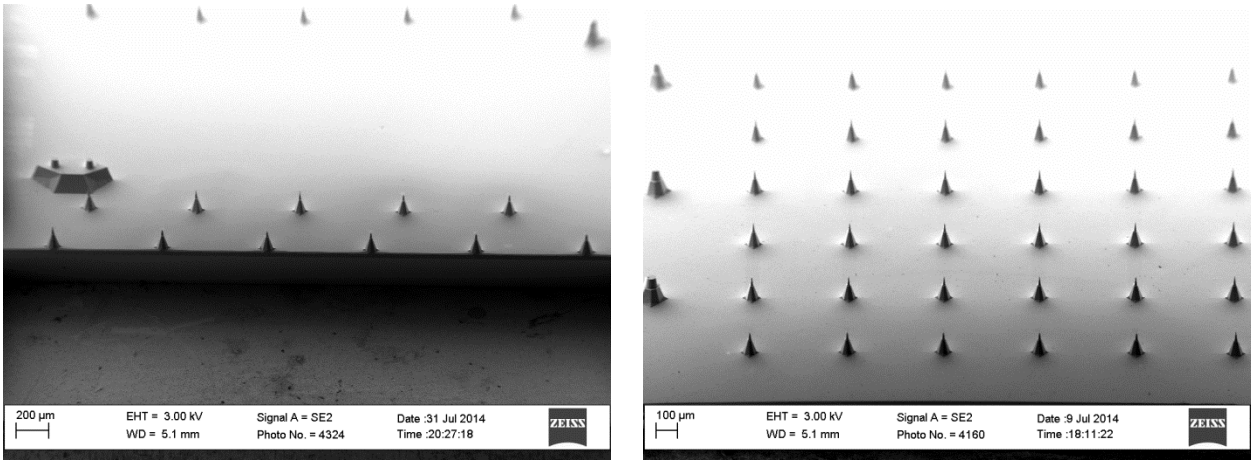

Fig. C. 2. SEM images of two types of Si coupon used for APT sample preparation. The first on the right has 22 Si posts with 2 rows of 5 and 2 rows of 6 Si posts. The one on the right has 36 Si posts (6×6). On both coupons there are fuducials for better identification of the position of the prepared samples.

Once the entire sample is used up, the deposition of platinum should be conducted on the second side of the wedge samples welded to Si posts. This is to make sure that there is a strong joint between the wedge and the Si post.

Needle-shape samples are made using annular milling technique. The annular milling is performed in three steps outlined below:

1- Annular milling using 30kV, 2nA ion beam, a ring-shape milling region with outer radius of 5 μm, and thickness of 1 μm as the starting point. The two dimensions are adjusted as the milling proceeds. The final diameter of the needle at this step is about 1.5 μm.

2- Annular milling using 30kV, 300nA ion beam, outer radius of about 3 μm, and thickness of 0.75 μm as the starting point. The two dimensions are adjusted as the milling proceeds. The final diameter of the needle at this step is about 500 nm. Upon reaching diameter of about 600 microns, the tip of the needle starts to mill off and becomes sharp. The milling should be continued until the platinum coating disappears. At this point, operator should be extra cautious not to mill off the entire sample. A good rule of thumb is that the diameter of the needle at 200 nm distance from the tip of the needle should be approximately 100 nm. Fig. C. 3. shows the needle and its tip at the end of this step. The transparent region at the top of the needle is clear in this image.

3- The final step is cleaning of the needle. This is performed by using a 5kV, 20 nA Ga ion beam and same dimension as the last step of the annular milling (i.e. about 1 μm outer radius and thickness of 0.25 nm). This step is stopped once the tip of the needle starts to mill off. The progress of each step is monitored on SEM.

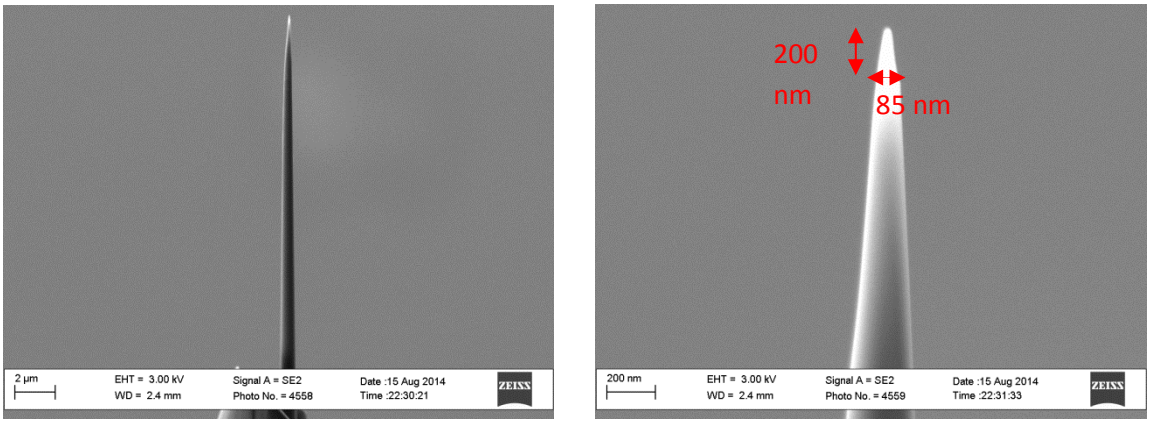

Fig. C. 3. Needle-shape sample made FIB milling. The transparent region of the needle is visible in the right image. The diameter of the needle at 200 nm distance from the tip is about 85 nm.